2019

Fabrication and Simulation of Nanomagnetic Devices for Information Processing

Justine L. Drobitch
Virginia Commonwealth University

Fabrication and Simulation of Nanomagnetic Devices for Information Processing

A dissertation submitted in partial fulfillment of the requirements for the degree of Doctor of Philosophy at Virginia Commonwealth University.

by

Justine L. Drobitch

Bachelor of Science in Physics and Astronomy, University of Pittsburgh, 2012

Advisor: Dr. Supriyo Bandyopadhyay

Commonwealth Professor, Department of Electrical and Computer Engineering

Virginia Commonwealth University

Richmond, Virginia

December, 2019

Acknowledgement

Many people have made this journey and this work possible. First, I would like to thank my advisor, Dr. Supriyo Bandyopadhyay, for his guidance, wisdom, and support over the past several years. It was truly inspiring to learn from someone with his level of knowledge and mastery of the field. I am deeply thankful to him for all the time he spent listening to, teaching (and reteaching), guiding, and helping me. Thank you for rolling the dice on a physicist and turning her into an engineer.

I am especially thankful for Dr. Daniel Gopman and for the six months I spent under his mentorship at NIST. Dan, I am a stronger researcher because of you, and everything I learned working in the lab with you and Xinjun greatly rounded out my experimental knowledge. I am also thankful for my other committee members, Dr. Jayasimha Atulasimha, Dr. Gary Atkinson, Dr. Ümit Özgür, and Dr. Shiv Khanna – each of whom has helped shape and inform my research in some way. I am very fortunate to have known and worked with these great professors and researchers who I respect and admire. I would also like to thank Dr. Erdem Topsakal, who made this whole journey possible and who has been an invaluable personal mentor to me. Stacy, I can't thank you enough for always having an ear to listen and a word of wisdom and encouragement to offer; if I could take you with me, you know I would.

To my colleagues Dr. Hasnain Ahmed, Dr. Md. Iftekhar Hossain, and Dr. Ayan Kumar Biswas: thank you for teaching me and guiding me during my first years of graduate study. To Dr. Md. Ahsanul Abeed: I'm glad we were able to learn and work together in our lab throughout our graduate study. Dylan, another thank you to someone who has been there from almost the

beginning to the end – I'm glad we could support and go through this process together. To all of the other graduate students I've had the opportunity to work with: thank you for all that you've taught me. To all of my friends – I'm a very lucky person because there are too many to name – thank you for making my time here in Richmond about more than just school and for keeping me a balanced, happy and loved person.

And finally, the most important and deepest thank you goes to the people who mean and are the world to me. Mom and Dad, nothing would have been possible without your endless love and support. Thank you for being the home we'll always come back to while we're out following our dreams. Jon, Neil, and Rissy – my bffs, my sibs, my life. *Even when we're far apart, I know we're always close at heart.*

Table of Contents

Acknowledgement iii
List of Figures vii
List of Tables xi
Abstract xii
Chapter 1: Introduction 1
Chapter 2: Precessional switching of a perpendicular anisotropy magnetic tunnel junction without a magnetic field 5
2.1 Introduction 5
2.2 Simulation Details 9
2.3 Results and Discussion 18
2.4 Conclusion 23
Chapter 2 References 24
Chapter 3: Robustness and scalability of p-bits implemented with low energy barrier nanomagnets 27
3.1 Introduction 27
3.2 Simulation Details 31
3.3 Results and Discussion 33
3.4 Conclusion 37
Chapter 3 References 39
Chapter 4: Systematic study of sputtering deposition rates towards reliable growth calibrations for magnetic device growth 41
4.1 Introduction 41
4.2 Experimental Details 42
4.3 Recipe Builder Results 46
4.4 Conclusion 47
Chapter 5: Effect of CoFe dusting layer and annealing on the magnetic properties of sputtered Ta/W/CoFeB/CoFe/MgO layer structures 49
5.1 Introduction 49
5.2 Experimental Details 51
5.3 Results and Discussion 54
5.4 Conclusion 68

Chapter 5 References 70
Chapter 6: Extreme sub-wavelength electromagnetic antenna implemented with acoustically driven magnetostrictive nanomagnets..... 73
6.1 Introduction 74
6.2 Experimental Details 75
6.3 Results and Discussion 80
6.4 Calculations 84
6.5 Conclusion 85
Chapter 6 References 86
Chapter 7: Conclusion 87
Vita and List of Publications 90

List of Figures

Fig. 2.1: (a) A magnetic tunnel junction (MTJ), (b) A perpendicular-magnetic-anisotropy magnetic tunnel junction (p-MTJ) 6

Fig. 2.2: (a) VCMA switching without an in-plane magnetic field. The magnetization rotates through 90°; (b) VCMA switching when an in plane magnetic field is present and the VCMA voltage pulse width is adjusted to one-half of the period of precession around the magnetic field. The magnetization rotates through 180°. 8

Fig. 2.3: Precessional switching of an MTJ with VCMA and no magnetic field. The write voltage V_{WRITE} is dropped across the piezoelectric (V_{st}) and the MTJ (V_{VCMA}). The former generates biaxial strain in the elliptical soft layer which acts as an effective in-plane magnetic field around which the out-of-plane magnetization vector begins to precess. By adjusting the V_{WRITE} pulse width to around one-half of the precessional period, the magnetization of the soft layer can be flipped to toggle the resistance of the MTJ between the high and low values. During the read cycle, the amplitude of V_{WRITE} is reduced (and, if necessary, the polarity is reversed) to suppress the VCMA effect. This is a 2-terminal device. 10

Fig. 2.4: The direction of effective magnetic field generated by the application of compressive and tensile stress along the major and minor axes of an ellipse. 11

Fig. 2.5: An example magnetization switching dynamic: (left) both VCMA and strain are turned on and the magnetization undergoes precessional motion, (right) VCMA and strain are turned off after half of the precessional period and the magnetization settles along the -x direction. 17

Fig. 2.6: The normalized out-of-plane magnetization component $m_x(t)$ as a function for time t for six different cases: (a) uniaxial compressive stress (-50 MPa) applied along the major axis of the elliptical soft layer, (b) uniaxial tensile stress (+50 MPa) along the major axis, (c) uniaxial compressive stress (-50 MPa) along the minor axis, (d) uniaxial tensile stress (+50 MPa) along the minor axis, (e) uniaxial compressive stress (-50 MPa) along the major axis *and* tensile stress (+50 MPa) along the minor axis, and (f) uniaxial tensile stress (+50 MPa) along the major axis *and* compressive stress (-50 MPa) along the minor axis. The VCMA voltage is turned on abruptly at time $t = 0$ and turned off abruptly at time $t = t_s$. The values of the applied VCMA voltage V_{VCMA}, the resulting current I and the pulse width t_s of V_{VCMA} are given in Table 2.2 for the six cases. Each figure has 10^4 switching trajectories plotted in the presence of room temperature thermal noise. Switching failures occur when the final steady state value of m_x is the initial value of +1 as opposed to -1. The write error probability is the fraction of trajectories that fail to switch. 21

Fig. 3.1: A low energy barrier nanomagnet (left), showing two different representative bits based on whether the projection of magnetization along the z axis is positive (bit 1) or negative (bit 0). The states are separated by an energy barrier (right) close to the thermal energy..... 28

Fig. 3.2: (a) An MTJ for a classical bit, (b) An MTJ for a p-bit using a LBM as the soft layer... 29

Fig. 3.3: (left) An LBM showing injected current that can have two directions of spin polarization. (right top) If the spin is polarized in the $+\hat{z}$ direction, there is an increased probability of writing bit 1 over bit 0; (right bottom) if the magnitude of the spin polarized current is larger, the probability of writing bit 1 over bit 0 is even higher. 30

Fig. 3.4: The probability of bit 1 as a function of spin polarized current for four different nanomagnet thicknesses of 5, 6, 7 and 15 nm. The major axis is 100 nm and the minor axis is 99.7 nm. The results are plotted for two different degrees of spin polarization in the current: 30% (top) and 70% (bottom). The variation in the probability at any given current is reduced at higher spin polarization. Positive value of the current corresponds to spin polarization in the +z direction and negative values correspond to spin polarization in the –z direction. For these thicknesses, the energy barrier heights are respectively 1.7 k_BT, 2.45 k_BT, 3.33 k_BT and 15.29 k_BT 35

Fig. 3.5: The probability of bit 1 as a function of spin polarized current for four different nanomagnet minor axis dimensions of 90, 98, 99 and 99.7 nm. The major axis dimension is fixed at 100 nm and the thickness is 6 nm. The results are plotted for two different degrees of spin polarization in the current: 30% (top) and 70% (bottom). As in Fig. 3.4, the variation is reduced at higher spin polarization..... 37

Fig. 4.1: An AFM step height image of a ruthenium film (left) grown for 10 minutes..... 44

Fig. 4.2: XRR data for the 10 min deposition ruthenium sample with measured data shown in red and the data fit shown in blue 44

Fig. 4.4: Sample deposition recipe created using the Recipe Builder module 47

Fig. 5.1: The layer structure of the sample. 51

Fig. 5.2: X-ray reflectivity scan of complete sample stack. The blue solid line is the fit to the intensity data (black points). Details of sample stack shown on right..... 52

Fig. 5.3: Exemplary x-ray reflectivity scans of our CoFe wedge used for deposition rate calibration. Intensity data taken at three positions on wedge: 30.6 nm (9 mm from thick edge);

23.2 nm (29 mm from thick edge); 14.6 (48 mm from thick edge). The colored solid lines are fits to the intensity data (open circles). The average lateral deposition rate gradient is estimated to be 4.50 (Å/s)/m, with an average deposition rate in the center estimated at 0.340 Å /s..... 53

Fig. 5.4: Magnetic moment vs. applied field for samples annealed at 400 °C with CoFeB/CoFe thickness of (a) 1.09 nm, (b) 1.14 nm, (c) 1.25 nm, and (d) 1.30 nm. 55

Fig. 5.5: Magnetic moment vs. applied field for samples annealed at 350 °C with CoFeB/CoFe thickness of (a) 1.09 nm, (b) 1.20 nm, (c) 1.25 nm, and (d) 1.29 nm. 56

Fig. 5.6: Magnetic moment vs. applied field for samples annealed at 325 °C with CoFeB/CoFe thickness of (a) 1.09 nm, (b) 1.14 nm, (c) 1.20 nm, (d) 1.24 nm, and (e) 1.30 nm. 57

Fig. 5.7: Magnetic moment vs. applied field for samples annealed at 300 °C with CoFeB/CoFe thickness of (a) 1.14 nm, (b) 1.20 nm, (c) 1.24 nm, and (d) 1.30 nm. 58

Fig. 5.8: Saturation moment vs. applied field for as-deposited samples with CoFeB/CoFe thickness of (a) 1.09 nm, (b) 1.14 nm, (c) 1.20 nm, (d) 1.24 nm, and (e) 1.29 nm. 59

Fig. 5.9: Saturation moment per unit area. Dead layer thickness and saturation magnetization were extracted from the x-intercept and slope, respectively. Inset: magnetic moment for sample with combined CoFeB/CoFe thickness of 1.20 nm annealed at 350 °C. 60

Fig. 5.10: A series of field-swept traces at numerous frequencies from 7 GHz (bottom left) to 27 GHz (top right) for the sample annealed at 350 °C with effective CoFe/CoFeB thickness of approximately 0.52 nm. Scans are offset vertically for clarity. 62

Fig. 5.11: (a) The ferromagnetic resonance field versus excitation frequency and (b) the linewidth versus excitation frequency of the sample with combined CoFeB and CoFe thickness t = 1.26 nm annealed at 350 °C. 63

Fig. 5.12: (a) Effective demagnetization field vs. effective thickness (combined CoFeB/CoFe layer thickness minus dead layer thickness) for several annealing temperatures. (b) Effective magnetic anisotropy multiplied by effective thickness versus the effective thickness for several annealing temperatures. 66

Fig. 5.13: Gilbert damping coefficient for annealing temperatures of (a) as-deposited, (b) 300 °C, (c) 325 °C, (d) 350 °C, and (e) 400 °C as a function of effective thickness of combined CoFeB/CoFe layer. 68

Fig. 5.14: The range of combined CoFeB/CoFe thicknesses and annealing temperatures which showed perpendicular magnetic anisotropy and those that showed in-plane magnetization..... 69

Fig. 6.1: A schematic of an extreme sub-wavelength electromagnetic antenna implemented with an array of magnetostrictive nanomagnets (not to scale) coupled to a piezoelectric substrate. ... 74

Fig. 6.2: Device fabrication schematic showing contact pads and alignment markers (yellow) and the area where magnets were deposited (grey) 75

Fig. 6.3: The photolithography fabrication process: (a) spin coat sample with SPR 3012, (b) soak in toluene, (c) photolithography and develop, (d) evaporate Ti and Au, (e) liftoff. 76

Fig. 6.4: The EBL fabrication process: (a) spin coat sample with PMMA 495, (b) spin coat with PMMA 950, (c) EBL and develop, (d) evaporate Ti and Co, (e) liftoff. 77

Fig. 6.5: Low magnification images of nanomagnet arrays of (a) Sample A and (b) Sample B.. 78

Fig. 6.6: An SEM image of Sample A, showing single nanomagnet array 80 nanomagnets across and 90 nanomagnets down 78

Fig. 6.7: An SEM image showing nanomagnets on Sample A 79

Fig. 6.8: An SEM image showing nanomagnets on Sample B 79

Fig. 6.9: An SEM image (Sample A) showing the measured magnet dimensions 80

Fig. 6.10: Experimental set-up of antenna measurement showing the antenna connected to a signal generator by a coaxial adapter and cable and the spectrum analyzer connected to a dipole antenna in the far-field. 81

Fig. 6.11: Spectrum analyzer measurement at 900 MHz for samples Control 1 and Sample A .. 81

Fig. 6.12: Spectrum analyzer measurement at 144 MHz for samples Control 1, Control 2, Sample A, and Sample B 82

Fig. 6.13: The measured S11 parameter for Sample A and the control samples, from 70 MHz to 2.4 GHz. 83

List of Tables

Table 2.1 – Parameters used in the simulations (soft layer is Terfenol-D) 18

Table 2.2 – Parameters chosen and simulation results for six different cases of applying uniaxial stresses (stress magnitude = 50 MPa) 20

Table 3.1 – Parameters used in the simulations 33

Table 4.1 – Crystal monitor, XRR, and AFM thickness measurements for the ruthenium calibration series 45

Table 4.2 – Deposition rates and tooling factors for ruthenium sample series 45

Table 5.1 – Dead layer thickness (t_{DL}) and saturation magnetization (M_S) for CoFeB/CoFe/MgO heterostructures for several annealing conditions 61

Table 6.1 – Peak signal strength (dBm) for sample and control measurements at 144 MHz and 900 MHz 83

Abstract

FABRICATION AND SIMULATION OF NANOMAGNETIC DEVICES FOR INFORMATION PROCESSING

By Justine L. Drobitch, Ph.D.

A dissertation submitted in partial fulfillment of the requirements for the degree of Doctor of Philosophy at Virginia Commonwealth University.

Virginia Commonwealth University, 2019.

Advisor: Dr. Supriyo Bandyopadhyay, Commonwealth Professor, Department of Electrical and Computer Engineering

Nanomagnetic devices are highly energy efficient and non-volatile. Because of these two attributes, they are potential replacements to many currently used information processing technologies, and they have already been implemented in many different applications. This dissertation covers a study of nanomagnetic devices and their applications in various technologies for information processing – from simulating and analyzing the mechanisms behind the operation of the devices, to experimental investigations encompassing magnetic film growth for device components to nanomagnetic device fabrication and measurement of their performance.

Theoretical sections of this dissertation include simulation-based modeling of perpendicular magnetic anisotropy magnetic tunnel junctions (p-MTJ) and low energy barrier nanomagnets (LBM) – both important devices for magnetic device-based information processing. First, we propose and analyze a precessionally switched p-MTJ based memory cell where data is written without any on-chip magnetic field that dissipates energy as low as 7.1 fJ. Next, probabilistic (p-) bits implemented with low energy barrier nanomagnets (LBMs) are also analyzed

through simulations, and plots show that the probability curves are not affected much by reasonable variations in either thickness or lateral dimensions of the magnetic layers.

Experimental sections of this dissertation comprise device fabrication aspects from the basics of material deposition to the application-based demonstration of an extreme sub-wavelength electromagnetic antenna. Magnetic tunnel junctions for memory cells and low barrier nanomagnets for probabilistic computing, in particular, require ultrathin ferromagnetic layers of uniform thickness, and non-uniform growth or variations in layer thickness can cause failures or other problems. Considerable attention was focused on developing methodologies for uniform thin film growth.

Lastly, micro- and nano-fabrication methods are used to build an extreme sub-wavelength electromagnetic antenna implemented with an array of magnetostrictive nanomagnets elastically coupled to a piezoelectric substrate. The 50 pW signal measured from the approximately 250,000-nanomagnet antenna sample was 10 dB above the noise floor.

Chapter 1: Introduction

Nanomagnetic devices are highly energy efficient and non-volatile potential replacements to many currently used information processing technologies. These devices are frequently used as "switches" between binary bits 0 and 1, and different methodologies are being explored to read and write information with the focus being on reducing energy to operate these devices. There are many ways to study, model, and measure the magnetization dynamics and properties, which will be discussed throughout this dissertation, as well as introducing the relevant theoretical and experimental information.

Nanomagnetic devices can be implemented in many different applications such as magnetic tunnel junctions (MTJs) for memory cells and low barrier nanomagnets (LBMs) for probabilistic computing, among others. This dissertation has examined different aspects of nanomagnetic devices that are used for information storage and processing, such as: field-free low-energy switching of nanomagnetic devices for memory using a combination of voltage controlled magnetic anisotropy, spin transfer torque and mechanical strain; the sensitivity of low barrier nanomagnetic devices used as hosts for probabilistic bits to device-to-device variations; thin film growth mechanisms with an eye to excellent control over film thickness in order to reduce device-to-device variations; structural engineering such as the introduction of a dusting layer to enhance magnetic properties of the thin film structures; and finally the experimental demonstration of an extreme sub-wavelength electromagnetic antenna implemented with magnetostrictive nanomagnets driven with a surface acoustic wave. The following chapters describe these aspects in greater detail.

In Chapter 2, strain-mediated switching of perpendicular-magnetic-anisotropy magnetic tunnel junctions (p-MTJ) is explored. The MTJs are used as memory cells and their resistances are switched between a high and a low resistance state to write binary bits 0 and 1 into the cell. This is accomplished with the combination of voltage controlled magnetic anisotropy (VCMA), spin polarized current injection that delivers spin transfer torque (STT) and mechanical strain. The use of strain eliminates the need for any in-plane on-chip magnetic field for complete magnetic reversal of the free layer of the p-MTJ. Simulations are carried out using the stochastic Landau-Lifshitz-Gilbert (s-LLG) equation to model precessional switching of these devices without using a magnetic field. The energy terms relevant to this precessional motion of magnetization in a ferromagnetic material will be discussed in this chapter. The switching (180° rotation of the free layer's magnetization) is accomplished using voltage-controlled-magnetic-anisotropy (VCMA), spin transfer torque (STT) and mechanical strain that is produced in the free layer by elastically coupling it to a piezoelectric film underneath and applying a voltage to the piezoelectric. The strain acts as an effective in-plane magnetic field around which the magnetization of the soft layer precesses to complete a flip. A two-terminal energy-efficient p-MTJ based memory cell, based on this strategy, that is compatible with crossbar architecture and high cell density, is designed.

In Chapter 3, similar s-LLG simulations are employed to model probabilistic (p-) bits implemented with low energy barrier nanomagnets (LBMs) with in-plane magnetization which can be leveraged to perform some computational tasks very efficiently. In some tasks (e.g. binary stochastic neurons for machine learning and p-bits for population coding), extended defects, such as variation of the LBM thickness over a significant fraction of the surface, can impair functionality. We have examined if unavoidable geometric device-to-device variations can have a significant effect on the ability to "program" probability with an external agent, such as a spin-

polarized current injected into the LBM. We found that the programming ability is fortunately not lost due to reasonable device-to-device variations. This is encouraging since it implies that p-bits can be scaled up to form "p-circuits" since p-bits are resilient to reasonable device-to-device variations.

In Chapter 4, we transition from simulation to explore fabrication aspects of magnetic devices. Precise control over the thin film deposition rate is essential for successful fabrication of ultrathin films and multilayered heterostructures, particularly for nm-thick magnetic layers used in spintronic devices. Magnetic tunnel junctions (MTJs) for memory cells and low barrier nanomagnets (LBMs) for probabilistic computing each require ultrathin ferromagnetic layers of uniform thickness, and non-uniform growth or variations can cause failures or other problems, such as those explored in Chapter 3. The work described in this chapter pertains to growth of thin magnetic films using an ultrahigh vacuum physical vapor deposition technique. Films were studied using x-ray reflectivity and atomic force microscopy. Growth rate calibrations were integrated into a tool for complex magnetic device fabrication.

In Chapter 5, we delve further into the growth and structure of magnetic devices and the analytical methods to investigate them. With a well-controlled and calibrated magnetic material deposition system, accurate lateral thickness variations can be deliberately induced to interesting effect studied in this chapter. We explored the effect of a CoFe wedge inserted as a dusting layer (0.2 nm – 0.4 nm thick) at the CoFeB/MgO interface of a layered magnetic device structure. Ferromagnetic resonance studies and vibrating sample magnetometry measurements were carried out to estimate magnetic properties of the sample as a function of the CoFe thickness and across several annealing temperatures. This study demonstrated the feasibility of using a dusting layer of CoFe at the interface between CoFeB and MgO to achieve moderate perpendicular magnetic

anisotropy, low damping, and relatively high saturation magnetization. These results have implications for p-MTJ devices such as those simulated in Chapter 1.

In Chapter 6, we demonstrate an extreme sub-wavelength electromagnetic antenna implemented with an array of magnetostrictive nanomagnets elastically coupled to an underlying piezoelectric substrate. This device is a culmination of theory and methods discussed in the preceding chapters, including piezoelectric and magnetic materials. The detected power measured at far field from the nanomagnet antenna sample was approximately 10 dB above the noise floor. Because the antenna is driven at the acoustic resonance instead of the electromagnetic resonance, the antenna can radiate with reasonable efficiency even though the antenna dimension is several orders of magnitude smaller than the electromagnetic wavelength. Had the antenna worked in the traditional fashion (driven by an electromagnetic wave at electromagnetic resonance instead of by an acoustic wave at acoustic resonance), the radiation efficiency would have been a few orders of magnitude lower. Such miniaturized (extreme sub-wavelength) antennas have many applications, such as in personal communicators, miniaturized RFID, and medically implanted devices that need to communicate signals outside the body.

Overall, this dissertation covers a comprehensive study of nanomagnetic devices and their uses in technology for information processing – from simulating and analyzing the mechanisms behind the devices, to experimental investigations encompassing magnetic film growth to nanomagnetic device fabrication.

Chapter 2: Precessional switching of a perpendicular anisotropy magnetic tunnel junction without a magnetic field

In this chapter, I describe an approach to implement precessional switching of a perpendicular-magnetic-anisotropy magnetic tunnel junction (p-MTJ) without using any magnetic field. The switching is accomplished with voltage-controlled-magnetic-anisotropy (VCMA), spin transfer torque (STT) and mechanical strain that is produced in the free layer by elastically coupling it to a piezoelectric film underneath and applying a voltage to the piezoelectric. The soft layer of the p-MTJ is magnetostrictive and the strain acts as an *effective in-plane magnetic field* around which the magnetization of the soft layer precesses to complete a flip. A two-terminal energy-efficient p-MTJ based memory cell, based on this strategy, that is compatible with crossbar architecture and high cell density, is designed.

2.1 Introduction

Magnetic tunnel junctions (MTJ) are devices composed of a thin insulting layer sandwiched between two ferromagnetic layers, with electron tunneling occurring through the insulting layer from one ferromagnetic layer to the other. The electrons that tunnel across the barrier between ferromagnetic electrodes are spin polarized, and the tunneling probability is higher when the two ferromagnetic electrodes are mutually aligned [1, 2]. One ferromagnetic layer has a fixed magnetization direction in-plane (hard layer) and the other is allowed to rotate its magnetization between parallel and anti-parallel states (soft or free layer), as shown in Fig. 2.1(a). The resistance of the MTJ is low when the magnetizations of the two layers are mutually parallel and high when they are mutually anti-parallel (this is a consequence of spin-dependent tunneling

through the spacer layer). These two resistance states encode binary bits 0 and 1 when the MTJ is used as a memory element.

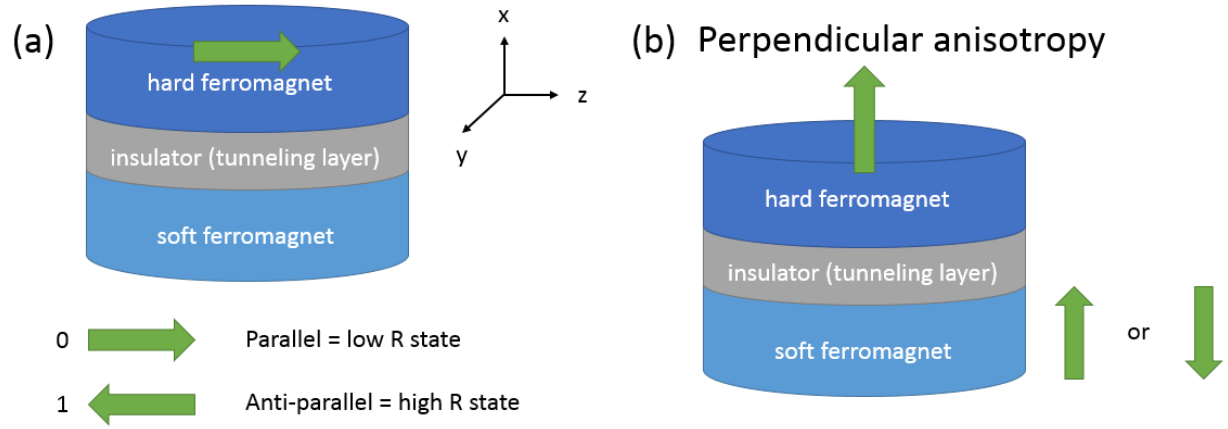

Fig. 2.1: (a) A magnetic tunnel junction (MTJ), (b) A perpendicular-magnetic-anisotropy magnetic tunnel junction (p-MTJ)

Perpendicular-magnetic-anisotropy magnetic tunnel junctions (p-MTJ), as shown in Fig. 2.1(b), have two stable magnetization orientations of the ferromagnetic layers that are not in-plane, but perpendicular to the surfaces. The physical origin of perpendicular magnetic anisotropy comes from the surface and interface effects beginning to outweigh the bulk as the magnetic layers become thinner. Once the surface anisotropy energy – preferring out-of-plane easy axis – becomes stronger than the demagnetizing energy – preferring in-plane easy axis – the magnetization rotates from in-plane to out-of-plane to minimize energy. Again, when the magnetizations of the two layers are mutually parallel, the resistance is low and when they are anti-parallel, the resistance is high. p-MTJs are the preferred embodiments of energy-efficient, non-volatile, high-density magnetic random access memory (MRAM) cells.

A chosen bit can be "written" by first "reading" the resistance and then (if necessary) flipping the magnetization of the soft layer with a voltage V_{VCMA} of appropriate polarity applied

across the MTJ which induces both voltage controlled magnetic anisotropy (VCMA) and spin transfer torque (STT) [3]. The spin transfer torque effect reflects spin polarized electrons tunneling into the free layer and delivering a torque on the magnetization of the free layer which is proportional to the accumulated spin polarized current incident on the free layer. VCMA, however, reflects the change in population of conduction band electrons at the interface between a ferromagnet and an oxide due to the accumulated charge associated with the ferromagnet-oxide interface. The increase in charge or depletion of charge will (depending on the conduction band structure of the ferromagnet) either enhance the magnetic anisotropy (making it less likely to switch) or reduce the magnetic anisotropy (making it easier to switch) [4]. As a result, the magnetization of the free layer will rotate from the perpendicular to in-plane orientation, resulting in 90° rotation of the magnetization. However, VCMA does not work alone: the voltage V_{VCMA} also drives a spin-polarized current between the hard and the soft layer which will result in a spin transfer torque acting on the magnetization of the soft layer. The current I flowing between the ferromagnetic hard and soft layers when V_{VCMA} is turned on is simply $I = V_{VCMA}/R_{MTJ}$ (R_{MTJ} = p-MTJ resistance) and this current, which is spin-polarized, automatically induces the STT.

We can change the relative importance of the roles of VCMA and STT in switching of magnetization by choosing the MTJ resistance; changing the thickness of the MgO layer can enhance the resistance of the barrier by orders of magnitude. A higher resistance will result in lower current and hence lower STT current, making VCMA more important, whereas a lower resistance will make STT dominant. VCMA is more energy efficient than STT because it is a voltage-controlled mechanism. Hence it will be preferable to increase the MTJ resistance to make VCMA dominant over STT. However VCMA alone can only change the magnetic anisotropy of the soft layer from “perpendicular” to “in-plane” [4, 5], resulting in 90° rotation of the soft layer’s

magnetization vector as shown in Fig. 2.2(a). To complete a 180° degree rotation (or "flip"), an in-plane magnetic field is applied in the plane of the soft layer, as shown in Fig. 2.2(b), causing the magnetization vector to precess about the magnetic field [6-8]. By adjusting the V_{VCMA} pulse width to approximately one-half of the precessional period, the magnetization vector can be made to undergo ~180° rotation and thus flip [6].

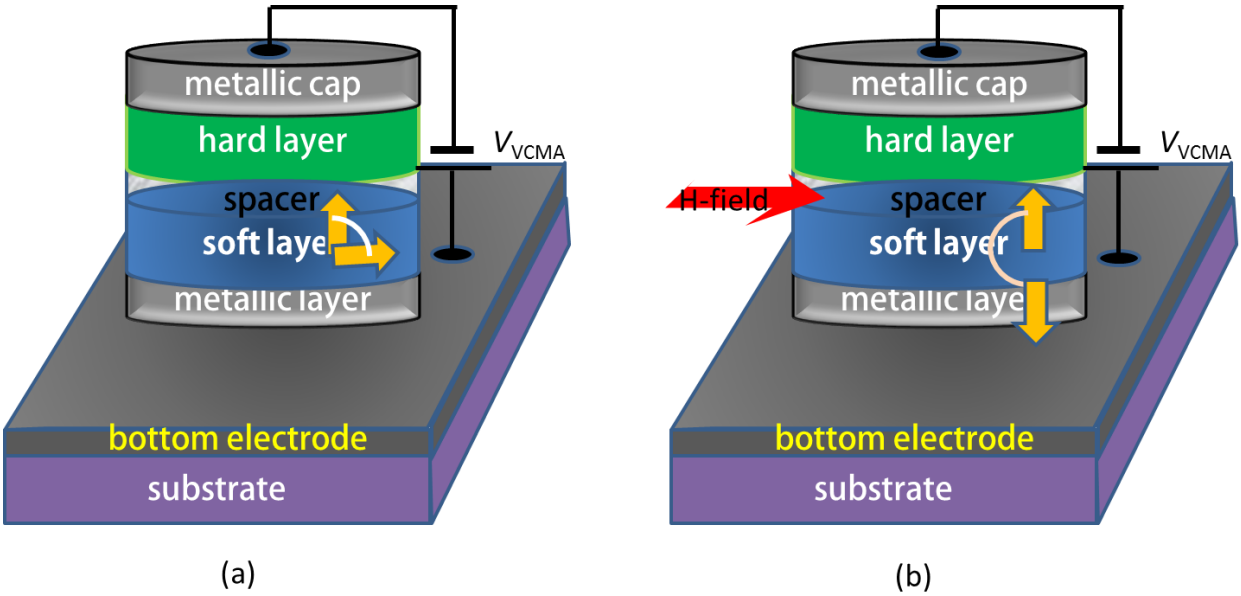

Fig. 2.2: (a) VCMA switching without an in-plane magnetic field. The magnetization rotates through 90°; (b) VCMA switching when an in plane magnetic field is present and the VCMA voltage pulse width is adjusted to one-half of the period of precession around the magnetic field. The magnetization rotates through 180°.

The in-plane magnetic field, however, can be inconvenient to generate, and it is challenging to maintain its uniformity across a chip. Hence, an effective magnetic field that can be generated electrically with a voltage will be desirable [8]. A possible route to deliver an effective magnetic field with a voltage is through constraining a ferromagnetic layer to a piezoelectric substrate; mechanical strain will generate an effective magnetic field in it via the inverse magnetostrictive (Villari) effect [9]. Furthermore, by placing contacts on the surface of a chip, individual bits can be locally strained, for ultrahigh density, low-energy control of magnetism at the nanoscale. Since

this field can be generated electrically, it will be easier to maintain uniformity across the chip and furthermore will result in all-electric switching. If the soft layer's cross-section is non-circular (e.g. elliptical), that too will generate an effective in-plane magnetic field from shape anisotropy, which will induce the required precessional motion of the magnetization vector to switch [9]. However, since the cross-sectional shape is difficult to control precisely, such an effective magnetic field will vary across a chip, which is undesirable. The cross-section of the p-MTJ can be made nearly circular which will make the effective field due to shape anisotropy much smaller than that due to strain, in which case any device-to-device variation of the shape anisotropy field will be inconsequential.

2.2 Simulation Details

Consider a p-MTJ stack with elliptical cross-section fabricated on a poled piezoelectric thin film with the soft layer in contact with the film. This configuration is shown in Fig. 2.3. A voltage V_{st} is applied over the piezoelectric film via electrodes on the surface. These electrodes are made of suitable dimensions and arranged in a suitable pattern to generate biaxial strain in the region of the piezoelectric film underneath the elliptical soft layer (compressive strain along the major axis and tensile strain along the minor axis, or vice versa, depending on the polarity of the voltage) [10-12]. The strain is partially or fully transferred to the soft layer through any ultrathin adhesion layer as shown in Fig. 2.3. If the soft layer is magnetostrictive, then the strain acts as an effective in-plane magnetic field within the soft layer.

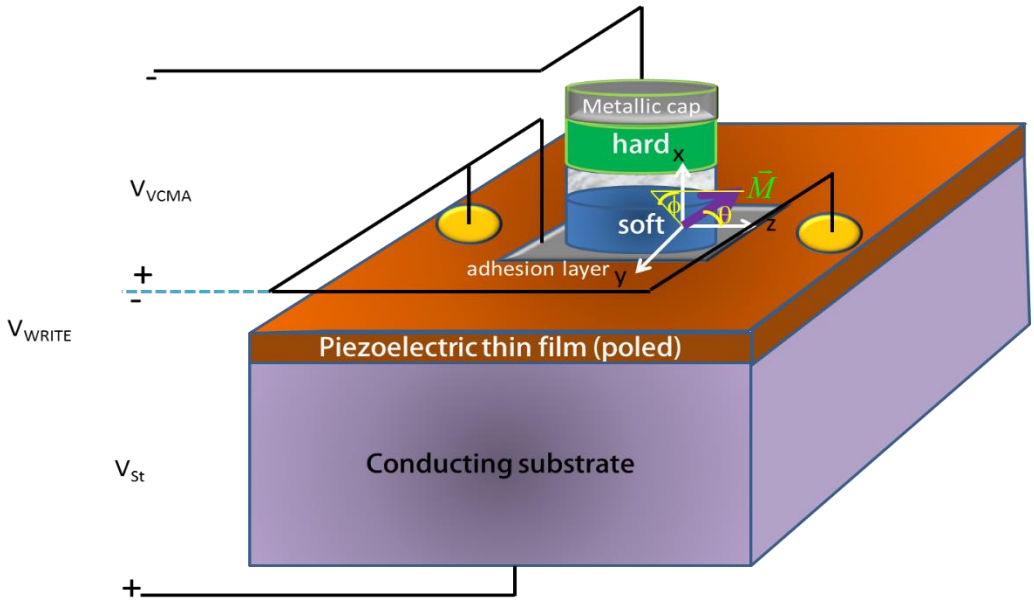

Fig. 2.3: Precessional switching of an MTJ with VCMA and no magnetic field. The write voltage V_{WRITE} is dropped across the piezoelectric (V_{st}) and the MTJ (V_{VCMA}). The former generates biaxial strain in the elliptical soft layer which acts as an effective in-plane magnetic field around which the out-of-plane magnetization vector begins to precess. By adjusting the V_{WRITE} pulse width to around one-half of the precessional period, the magnetization of the soft layer can be flipped to toggle the resistance of the MTJ between the high and low values. During the read cycle, the amplitude of V_{WRITE} is reduced (and, if necessary, the polarity is reversed) to suppress the VCMA effect. This is a 2-terminal device.

For a material with a positive magnetostriction coefficient (e.g. in materials like Terfenol-D or Galfenol), compressive stress along the major axis results in an effective magnetic field along the minor axis, while tensile strain results in an effective magnetic field along the major axis. Similarly, compressive strain along the minor axis will result in an effective magnetic field along the major axis and tensile strain will result in an effective magnetic field along the minor axis. This is illustrated in Fig. 2.4. The directions are reversed if the magnetostriction coefficient is negative (e.g. in Co, Ni). Therefore, biaxial strain will always produce an effective magnetic field that is directed along either the major or the minor axis of the ellipse around which the magnetization vector of the p-MTJ's soft layer precesses after a voltage V_{VCMA} applied across the p-MTJ dislodges it from the initial out-of-plane orientation. Materials such as Terfenol-D and Galfenol are also advantageous over Co or Ni because their magneto-mechanical coupling is very large.

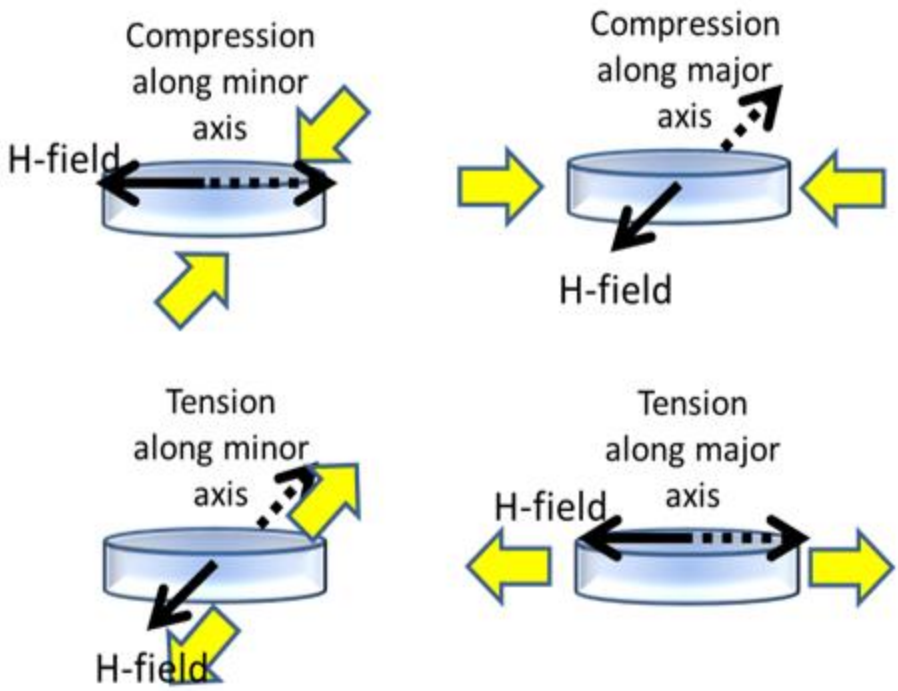

Fig. 2.4: The direction of effective magnetic field generated by the application of compressive and tensile stress along the major and minor axes of an ellipse.

To model the precessional dynamics of the soft layer's magnetization under the combined action of VCMA, STT and strain, we solved the stochastic Landau-Lifshitz-Gilbert (s-LLG) equation within the macrospin approximation numerically using a MATLAB solver that we developed for this purpose. This equation is written as [13]:

$$\frac{d\vec{n}_m(t)}{dt}-\alpha\left(\vec{n}_m(t)\times\frac{d\vec{n}_m(t)}{dt}\right)=-\frac{|\gamma|}{M_V}\left[\vec{n}_m(t)\times\vec{H}_E(t)+\vec{n}_m(t)\times\vec{H}_{TH}(t)\right]+|\gamma|\beta\varepsilon\left(\vec{n}_m(t)\times\vec{n}_p\times\vec{n}_m(t)\right)$$
$$-|\gamma|\beta\varepsilon'\left(\vec{n}_m(t)\times\vec{n}_p\right) \quad (1.1)$$

where

$\vec{n}_m = m_x\hat{x}+m_y\hat{y}+m_z\hat{z}$ (unit vector in the direction of the magnetization)

$$\beta=\left|\frac{\hbar}{\mu_0 e}\right|\frac{J}{lM_s}$$

$\vec{n}_p$ = unit vector in the direction of spin polarization of STT current

$$\varepsilon=\frac{P\Lambda^2}{\left(\Lambda^2+1\right)+\left(\Lambda^2-1\right)\left(\vec{n}_m\cdot\vec{n}_p\right)}$$

$\Lambda = 1$

$P = 0.8$

ε' = secondary spin transfer term = 0

where α is the Gilbert damping constant of the soft layer, $\gamma=\frac{2\mu_B\mu_0}{\hbar}=2.21\times10^5\,(\text{rad.m})/(\text{A.s})$, μ_B is the Bohr magneton, $M_V = \mu_o M_s \Omega$, μ_o is the permeability of free space, M_s is the saturation magnetization of the soft layer, Ω is the volume of the soft layer, $\hbar$ is reduced Planck constant, e is the electron charge, l is the thickness of the soft layer, J is the current density associated with the current I flowing between the hard and the soft layer, P is the spin polarization of the current and Λ is the product of the soft layer's conductance and the average resistance of the MTJ (averaged over the low and high resistance states) [12]. Since the soft layer's conductance can be chosen arbitrarily, we choose $\Lambda = 1$. We also choose the spin polarization of the STT current to be 80%. Finally, we considered only the Slonczewski STT term and assumed the field-like term to be zero. Consideration of the field-like term will obviously cause some quantitative change, but no qualitative change.

The quantity $\vec{H}_E$ is the effective magnetic field experienced by the magnetization vector of the soft layer due to any shape anisotropy field, strain and surface anisotropy, while $\vec{H}_{TH}$ is a random magnetic field due to thermal noise and is given by

$$\vec{H}_{TH}(t) = h_x(t)\hat{x} + h_y(t)\hat{y} + h_z(t)\hat{z} \ , \tag{2.2}$$

where $h_x(t), h_y(t), h_z(t)$ are three independent (uncorrelated) random magnetic fields given by [14]

$$h_i(t) = \sqrt{\frac{2\alpha kT}{\gamma(1+\alpha^2)M_V \Delta t}} G_{(0,1)}(t) \qquad (i = x, y, z) \tag{2.3}$$

in which Δt is the inverse of the attempt frequency (it is also the time step used in the simulation to solve Equation (2.1), which in this case was 0.1 ps), k is the Boltzmann constant, T is the absolute temperature, and $G_{(0,1)}(t)$ is a Gaussian with zero mean and unit standard deviation.

Equation (2.1) can be reduced to three scalar equations for each component of the magnetization vector:

$$
\begin{aligned}
\frac{dm_x(t)}{dt} &= -\gamma\left[H_z(t)m_y(t) - H_y(t)m_z(t)\right] \\
&\quad -\alpha\gamma\left[H_y(t)m_x(t)m_y(t) - H_x(t)m_y^2(t) - H_x m_z^2(t) + H_z(t)m_x(t)m_z(t)\right] \\
&\quad -\gamma\beta\varepsilon\left[m_y{}^2(t) + m_z{}^2(t)\right] \\
\frac{dm_y(t)}{dt} &= -\gamma\left[H_x(t)m_z(t) - H_z(t)m_x(t)\right] \\
&\quad -\alpha\gamma\left[H_z(t)m_y(t)m_z(t) - H_y(t)m_z^2(t) - H_y m_x^2(t) + H_x(t)m_x(t)m_y(t)\right] \qquad (1.4) \\
&\quad +\gamma\beta\varepsilon\left[-\alpha\left(m_z(t)\left(m_x{}^2(t) + m_y{}^2(t)\right) + m_z{}^2(t)\right) + m_x(t)m_y(t)\right] \\
\frac{dm_z(t)}{dt} &= -\gamma\left[H_y(t)m_x(t) - H_x(t)m_y(t)\right] \\
&\quad -\alpha\gamma\left[H_x(t)m_x(t)m_z(t) - H_z(t)m_x^2(t) - H_z m_y^2(t) + H_y(t)m_y(t)m_z(t)\right] \\
&\quad +\gamma\beta\varepsilon\left[\begin{array}{l}\alpha^3 m_z(t)\left(m_y{}^2(t) + m_z{}^2(t)\right)\left(m_z(t) - m_y(t)\right) - \alpha^2 m_x(t)\left(m_y{}^2(t) + m_z{}^2(t)\right)\left(1 - m_z(t)\right) \\ +\alpha\left(m_x{}^2(t)m_y(t) + m_y{}^2(t) + m_z{}^2(t)\right) + m_x(t)m_z(t)\end{array}\right]
\end{aligned}
$$

where

$$\vec{H}_E + \vec{H}_{TH} = H_x\hat{x} + H_y\hat{y} + H_z\hat{z}. \qquad (2.5)$$

We define the major axis of the soft layer to be along the *z*-axis, the minor axis along the *y*-axis and the out-of-plane axis to be the *x*-axis. The voltage V_{st} would result in biaxial strain (compression along the major axis of the ellipse and tension along the minor axis, or vice versa, depending on the polarity of V_{st}). Since biaxial strain is difficult to handle within the s-LLG formulation, we will approximate the effect of strain as producing uniaxial stress along the major axis of the ellipse and uniaxial stress of opposite sign along the minor axis. In that case, the expressions for the magnetic field components in the above equation are:

$$H_x(t) = -M_s N_{d-xx} m_x(t) + h_x(t) + \frac{2\left(K_{s0} + \kappa V_{VCMA}/t_b\right)}{\mu_0 M_s l} m_x(t)$$
$$H_y(t) = -M_s N_{d-yy} m_y(t) + h_y(t) + \frac{3}{\mu_0 M_s}\left(\lambda_s \sigma_{yy}\right) m_y(t) \qquad (2.6)$$
$$H_z(t) = -M_s N_{d-zz} m_z(t) + h_z(t) + \frac{3}{\mu_0 M_s}\left(\lambda_s \sigma_{zz}\right) m_z(t)$$

where K_{s0} is the surface anisotropy constant, κ is the VCMA coefficient, t_b is the spacer layer thickness, λ_s is the magnetostriction coefficient of the soft layer, σ_{zz} is the uniaxial stress generated along the major axis of the ellipse and σ_{yy} is the uniaxial stress generated along the minor axis (σ_{zz} and σ_{yy} have opposite signs). The quantities $N_{d\text{-}mm}$ are the demagnetization factors along the *m*-th direction and depend on the dimensions of the major and minor axes, as well as the thickness of the soft layer. They can be calculated with the prescription in Ref. [15]. The first terms in each of the equations above are associated with the shape anisotropy field, the second terms with the random field due to thermal noise, the last term in the top equation is the field associated with surface anisotropy which is modulated by the VCMA voltage and the last term in the bottom equations is the field associated with the uniaxial stress. Note that the last field is *not constant* and is proportional to the component of the magnetization along the stress axis. As a result, this field will be non-existent if the precession of the magnetization vector is constrained to the plane normal to the stress axis. However, that never happens since thermal noise will always displace the magnetization vector from such a plane. Nonetheless, the non-constant nature of the effective magnetic field due to stress and its dependence on the magnetization vector's component along the stress axis (which is unlike the case of the constant in-plane magnetic field) reduces the probability of flipping in the presence of thermal noise and increases the write error probability (WEP).

In order to obtain the magnetization dynamics under the combined effects of VCMA, stress and STT (i.e. to find the components of the magnetization vector $m_x(t)$, $m_y(t)$ and $m_z(t)$ as a function of time *t*), we solve Equations (2.4) - (2.6) with initial conditions $m_x(0)=1,\ m_y(0)=m_z(0)=0.$ The soft layer's magnetization is assumed to be initially along the +*x*-axis and the application of the voltages V_{VCMA} (which also causes the STT) and V_{st} will flip it to align along the –*x*-axis. Hence we had picked the spin polarization of the STT current to be along the –*x* axis $\left(\vec{n}_p=-\hat{x}\right)$ in Equation (2.4).

Because of the presence of the random thermal field $\vec{H}_{TH}(t)$, Equations (2.4) and (2.6) will obviously yield different solutions (i.e. different switching trajectories) at different times. Therefore, we carry out simulations of 10^4 switching trajectories. The voltage V_{st} is always chosen to produce a stress $\left(\sigma_{yy}=\sigma_{zz}=\sigma\right)$ of 50 MPa. The maximum value of the effective magnetic field produced by stress is $\left|3\lambda\sigma/\left(\mu_0 M_s\right)\right|$. For a highly magnetostrictive soft layer made of Terfenol-D $Tb_{0.27}Dy_{0.73}Fe_{1.95}\left(\lambda_s=600\text{ ppm},\ M_s=8\times10^5\text{ A/m}\right)$[14], the 50 MPa uniaxial stress will generate an effective magnetic field of strength H_{eff} = 90,000 A/m (1,125 Oe).

We turn on V_{VCMA} and V_{st} at time t = 0 and turn both off after a fixed time t_s which corresponds to approximately one half of the precession period, as shown in the example Fig. 2.5. In the first plot, VCMA and strain are not turned off and the magnet continues to precess; in the second plot, both voltages are turned off at the half of the precession period. We then continue the simulation until steady state is reached, i.e. until m_x reaches the value +1 or -1 for every trajectory. The +1 value indicates switching failure (the magnetization vector returns to the original orientation and does not flip) while the -1 value indicates successful flip. The switching error probability, which corresponds to the write error probability (WEP) in memory, is the fraction of

the trajectories (out of 10^4 simulated) that fails to switch. This probability depends on the magnitude of V_{VCMA} (which also determines the value of the STT current density J for a given resistance and cross-sectional area of the p-MTJ), the stress and the pulse duration t_s. These parameters can be tweaked to minimize the error probability, but usually at the expense of larger V_{VCMA} and t_s, which will increase the energy dissipation.

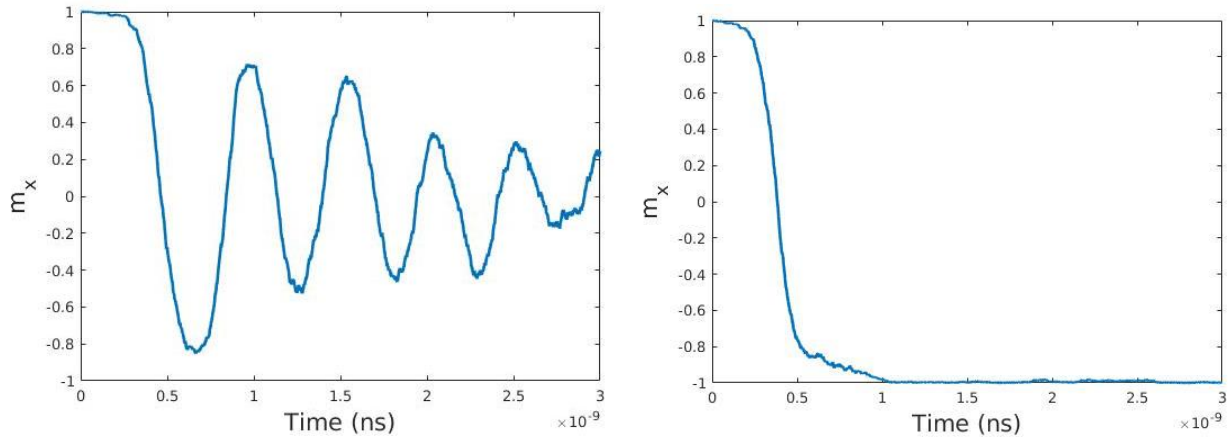

Fig. 2.5: An example magnetization switching dynamic: (left) both VCMA and strain are turned on and the magnetization undergoes precessional motion, (right) VCMA and strain are turned off after half of the precessional period and the magnetization settles along the -x direction.

The energy dissipation is given by

$$E_d = V_{VCMA} I t_s + C V_{st}^2 + E_{\text{int}} = V_{VCMA} J \left(\frac{\pi}{4} ab \right) t_s + C V_{st}^2 + E_{\text{int}} \ , \tag{2.7}$$

where a is the major axis dimension, b the minor axis dimension, C is the capacitance associated with charging the piezoelectric film to the voltage V_{st} and E_{int} is the internal energy dissipation within the soft layer due to Gilbert damping and mechanical loss. The first term in Equation (2.7) is overwhelmingly dominant and hence is the only term considered in calculating the energy dissipation [17]. In order to keep the energy dissipation as low as possible, we chose the soft layer material as Terfenol-D and chose the parameters in Table 2.1 for all our simulations. Some parameters showed a range of possible values, and we used values that would minimize the energy

dissipation. We could expect more energy dissipation and/or a higher write error probability from using more conservative values for the surface anisotropy per unit area and the VCMA constant.

Table 2.1 – Parameters used in the simulations (soft layer is Terfenol-D)

Parameter	Value
Surface anisotropy per unit area (K_{s0})	340 μJ m^{-2} [range 320-980 μJ m^{-2}] [19, 22, 23]
VCMA constant (C)	1000 fJ V^{-1} m^{-1} [range 3.3-1150 fJ V^{-1} m^{-1}] [6, 18-21]
Saturation magnetization (M_s)	8×10^5 A/m [15]
Magnetostriction coefficient (λ)	600 ppm [15]
Gilbert damping (α)	0.1
Major axis of soft layer	60 nm
Minor axis of soft layer	55 nm
Thickness of soft layer	0.8 nm
Young's modulus of soft layer	80 GPa
Spacer layer thickness	1.4 nm

2.3 Results and Discussion

In Fig. 2.6, we plot the switching trajectories for six different scenarios: uniaxial compressive stress (-50 MPa) applied along the major axis of the elliptical soft layer, uniaxial tensile stress (+50 MPa) along the major axis, uniaxial compressive stress (-50 MPa) along the minor axis, uniaxial tensile stress (+50 MPa) along the minor axis, uniaxial compressive stress (-50 MPa) along the major axis *and* tensile stress (+50 MPa) along the minor axis, and uniaxial tensile stress (+50 MPa) along the major axis *and* compressive stress (-50 MPa) along the minor axis. The switching error probability (or write error probability) is the fraction of the 10,000 switching trajectories in each case that fails to switch. For the six different cases, the values of V_{VCMA}, I, the corresponding current density J, the switch-off time t_s (which is the width of the V_{VCMA} pulse), the energy dissipation E_d, and the write error probability (WEP) are listed in Table

2.2. The lowest energy dissipation values are comparable to the best reported in Ref. [24] for an experimental demonstration with higher switching error probability (~10% error).

It would be possible to reduce the energy dissipation further if one can find a material with much larger VCMA coefficient since that would reduce the VCMA voltage needed to switch the MTJ. It may also be possible to reduce the energy dissipation by relaxing the requirement on write error probability. One could reduce both VCMA voltage amplitude and pulse duration to reduce the energy dissipation, but at the cost of a much higher switching error probability. The tolerable error probability depends on the application. Non-Boolean applications of switches (e.g. in neural networks) are more error-tolerant and in these types of applications, the requirement on switching error probability can be relaxed to decrease energy dissipation.

Table 2.2 – Parameters chosen and simulation results for six different cases of applying uniaxial stresses (stress magnitude = 50 MPa)

	Compressive stress along major axis	Tensile stress along major axis	Compressive stress along minor axis	Tensile stress along minor axis	Compressive along major axis and tensile along minor	Tensile along major axis and compressive along minor
V_{VCMA} (mV)	-80	-28	-80	-28	-60	-60
STT current I (mA)	-0.33	-0.36	-0.36	-0.33	-0.66	-0.66
STT current density$J$ (MA/cm^2)	-12.7	-13.9	-13.9	-12.7	-25.5	-25.5
VCMA pulse width t_s (ns)	0.7	0.7	0.7	0.7	0.35	0.35
Energy dissipation (E_d) in fJ	18.5	7.06	18.5	7.06	13.9	13.9
Write error probability (*WEP*)	10^{-4}	10^{-4}	10^{-4}	$< 10^{-4}$	10^{-4}	10^{-4}

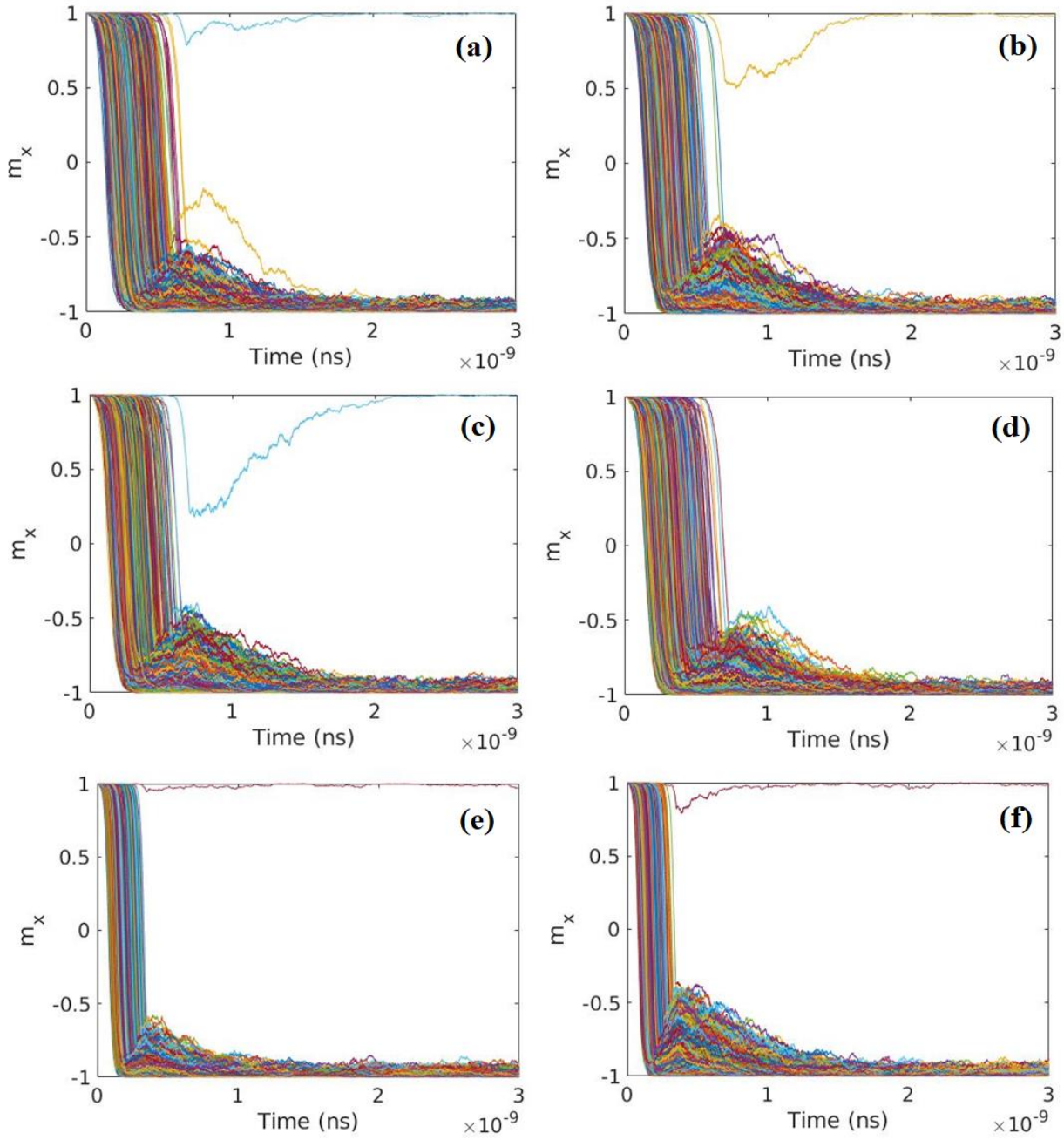

Fig. 2.6: The normalized out-of-plane magnetization component $m_x(t)$ as a function for time t for six different cases: (a) uniaxial compressive stress (-50 MPa) applied along the major axis of the elliptical soft layer, (b) uniaxial tensile stress (+50 MPa) along the major axis, (c) uniaxial compressive stress (-50 MPa) along the minor axis, (d) uniaxial tensile stress (+50 MPa) along the minor axis, (e) uniaxial compressive stress (-50 MPa) along the major axis *and* tensile stress (+50 MPa) along the minor axis, and (f) uniaxial tensile stress (+50 MPa) along the major axis *and* compressive stress (-50 MPa) along the minor axis. The VCMA voltage is turned on abruptly at time $t = 0$ and turned off abruptly at time $t = t_s$. The values of the applied VCMA voltage V_{VCMA}, the resulting current I and the pulse width t_s of V_{VCMA} are given in Table 2.2 for the six cases. Each figure has 10^4 switching trajectories plotted in the presence of room temperature thermal noise. Switching failures occur when the final steady state value of m_x is the initial value of +1 as opposed to -1. The write error probability is the fraction of trajectories that fail to switch.

There is a reason why the write error probabilities at room temperature are relatively large (~10^{-4}) compared to what have been reported in the literature [3, 7, 22-24]. As stated earlier, the effective magnetic field due to stress depends on the component of the magnetization vector along the stress axis and is not constant. Since the magnetization component has a random component due to thermal noise, the effective magnetic field also has a random component that results in a random variation of the precessional period. This is the reason behind the high error rate. An actual in-plane magnetic field would have been constant, resulting in a constant precession period, which, in turn, would have reduced the error probability. The high error probability is a trade-off for the elimination of the on-chip magnetic field. The error probabilities reported here, however, are still lower than what has been experimentally observed in magneto-electric memory cells [25].

An important consideration for a memory cell is that it should have no more than two terminals to maintain high cell density and be compatible with simple cross-bar architecture. In other words, the *same* two terminals should be used to apply a voltage for "read" and "write" operations. The design shown in Fig. 2.3 accomplishes this. There are only two terminals that are used for both read and write operations. The voltage dropped over the MTJ stack to induce VCMA is labeled V_{VCMA} and that dropped over the piezoelectric to induce stress in the soft layer is labeled V_{st}. They are related to the write voltage V_{WRITE} as $V_{VCMA} = R_{MTJ} \big/ \left(R_{MTJ} + R_{piezo} \right) V_{WRITE}$; $V_{st} = R_{piezo} \big/ \left(R_{MTJ} + R_{piezo} \right) V_{WRITE}$, where R_{MTJ} is the resistance of the MTJ stack and R_{piezo} is the resistance of piezoelectric film between the two shorted electrodes and the conducting substrate in Fig. 2.3. Since R_{MTJ} is different in the on- and off-states, we have to choose V_{WRITE} such that the lower value of $V_{VCMA}^{low} = R_{MTJ}^{ON} \big/ \left(R_{MTJ}^{ON} + R_{piezo} \right) V_{WRITE}$ exceeds the voltage required to switch with precessional motion as opposed to thermal activation. Similarly, the lower value of

$V_{st}^{low} = R_{piezo} \Big/ \left(R_{MTJ}^{OFF} + R_{piezo} \right) \mathrm{V_{WRITE}}$ must exceed the value required to generate the needed stress. Since the Young's modulus of Terfenol-D is 80 GPa, the amount of strain needed to produce 50 MPa stress in the soft layer of the p-MTJ is 625 ppm. Let us assume that the piezoelectric film is (001) PMN-PT, whose piezoelectric coefficient is ~ 2000 pC/N. Hence, the electric field needed in the piezoelectric film is 0.3125 MV/m. If the piezoelectric film is 100 nm thick, then the voltage V_{st}^{low} will be 31.25 mV. $\mathrm{V_{WRITE}}$ should exceed the greater of $V_{VCMA}^{low} \left(1 + R_{piezo} \Big/ R_{ON}^{MTJ} \right), V_{st}^{low} \left(1 + R_{OFF}^{MTJ} \Big/ R_{piezo} \right)$. Note that this design requires V_{VCMA} and V_{st} to be turned on and off at the same time; they cannot be controlled independently. However, this design lends itself to a two-terminal configuration which is vital for a memory cell.

2.4 Conclusion

In conclusion, we have proposed and analyzed a precessionally switched p-MTJ based memory cell where data is written with VCMA *without any on-chip magnetic field*. The role of the in-plane magnetic field is played by in-plane stress. This approach introduces some additional energy dissipation needed to generate the stress, but that energy overhead is almost negligible [26]. It is a small price to pay for eliminating the on-chip magnetic field.

Chapter 2 References

[1] M. N. Baibich, J. M. Broto, A. Fert, F. Nguyen Van Dau, F. Petroff, P. Etienne, G. Creuzet, A. Friederich, and J. Chazelas, “Giant Magnetoresistance of (001)Fe/(001)Cr Magnetic Superlattices,” *Phys. Rev. Lett.*, vol. 61, p. 2472, 1988.

[2] G. Binasch, P. Grünberg, F. Saurenbach, and W. Zinn, “Enhanced magnetoresistance in layered magnetic structures with antiferromagnetic interlayer exchange,” *Phys. Rev. B,* vol. 39, p. 4828, 1989.

[3] S. Wang, H. Lee, F. Ebrahimi, P. K. Amiri, K. L. Wang and P. Gupta, "Comparative Evaluation of Spin-Transfer-Torque and Magnetoelectric Random Access Memory," *IEEE Journal on Emerging and Selected Topics in Circuits and Systems,* vol. 6, no. 2, pp. 134-145, 6 2016.

[4] P. K. Amiri and K. L. Wang, "Voltage-Controlled Magnetic Anisotropy in Spintronic Devices," *SPIN*, 2012.

[5] T. Maruyama, Y. Shiota, T. Nozaki, K. Ohta, N. Toda, M. Mizuguchi, A. A. Tulapurkar, T. Shinjo, M. Shiraishi, S. Mizukami, Y. Ando and Y. Suzuki, "Large voltage-induced magnetic anisotropy change in a few atomic layers of iron," *Nature Nanotechnology*, 2009.

[6] S. Kanai, M. Yamanouchi, S. Ikeda, Y. Nakatani, F. Matsukura and H. Ohno, "Electric field-induced magnetization reversal in a perpendicular-anisotropy CoFeB-MgO magnetic tunnel junction," *Applied Physics Letters*, 2012.

[7] Y. Shiota, T. Nozaki, F. Bonell, S. Murakami, T. Shinjo and Y. Suzuki, "Induction of coherent magnetization switching in a few atomic layers of FeCo using voltage pulses," *Nature Materials,* 2012.

[8] J. Stöhr, H. C. Siegmann, A. Kashuba and S. J. Gamble, "Magnetization switching without charge or spin currents," *Citation: Appl. Phys. Lett*, vol. 94, 2009.

[9] M. Salehi Fashami, J. Atulasimha and S. Bandyopadhyay, "Magnetization dynamics, throughput and energy dissipation in a universal multiferroic nanomagnetic logic gate with fan-in and fan-out," *Nanotechnology*, vol. 23, no. 10, p. 105201, 16 3 2012.

[10] J. Cui, J. L. Hockel, P. K. Nordeen, D. M. Pisani, C.-y. Liang, G. P. Carman and C. S. Lynch, "A method to control magnetism in individual strain-mediated magnetoelectric islands," *Applied Physics Letters,* vol. 103, no. 23, p. 232905, 2 12 2013.

[11] C.-Y. Liang, S. M. Keller, A. E. Sepulveda, W.-Y. Sun, J. Cui, C. S. Lynch and G. P. Carman, "Electrical control of a single magnetoelastic domain structure on a clamped piezoelectric thin film—analysis," *Journal of Applied Physics,* vol. 116, no. 12, p. 123909, 28 9 2014.

[12] J. Cui, C.-Y. Liang, E. A. Paisley, A. Sepulveda, J. F. Ihlefeld, G. P. Carman and C. S. Lynch, "Generation of localized strain in a thin film piezoelectric to control individual magnetoelectric heterostructures," *Applied Physics Letters,* vol. 107, no. 9, p. 092903, 31 8 2015.

[13] *OOMMF User's Guide* Release 1.2b0 (September 29, 2016)

[14] J. Xiao, A. Zangwill and M. D. Stiles, "Boltzmann test of Slonczewski's theory of spin-transfer torque," *Physical Review B,* vol. 70, no. 17, p. 172405, 12 11 2004.

[15] M. Beleggia, M. De Graef and Y. Millev, "Demagnetization factors of the general ellipsoid: An alternative to the Maxwell approach," *Philosophical Magazine,* vol. 86, no. 16, pp. 2451-2466, 6 2006.

[16] R. Kellogg and A. Flatau, "Experimental Investigation of Terfenol-D's Elastic Modulus," *Journal of Intelligent Material Systems and Structures,* vol. 19, no. 5, pp. 583-595, 30 5 2008.

[17] A. K. Biswas, S. Bandyopadhyay, and J. Atulasimha, "Complete magnetization reversal in a magnetostrictive nanomagnet with voltage-generated stress: A reliable energy-efficient non-volatile magneto-elastic memory," *Applied Physics Letters*, vol. 105, p. 072408, 2014.

[18] J. W. Koo, S. Mitani, T. T. Sasaki, H. Sukegawa, Z. C. Wen, T. Ohkubo, T. Niizeki, K. Inomata and K. Hono, "Large perpendicular magnetic anisotropy at Fe/MgO interface," *Applied Physics Letters,* 2013.

[19] A. Rajanikanth, T. Hauet, F. Montaigne, S. Mangin and S. Andrieu, "Magnetic anisotropy modified by electric field in V/Fe/MgO(001)/Fe epitaxial magnetic tunnel junction," *Applied Physics Letters,* vol. 103, no. 6, p. 062402, 5 8 2013.

[20] T. Nozaki, Y. Shiota, M. Shiraishi, T. Shinjo and Y. Suzuki, "Voltage-induced perpendicular magnetic anisotropy change in magnetic tunnel junctions," *Applied Physics Letters,* 2010.

[21] Y. Shiota, S. Murakami, F. Bonell, T. Nozaki, T. Shinjo and Y. Suzuki, "Quantitative Evaluation of Voltage-Induced Magnetic Anisotropy Change by Magnetoresistance Measurement," *Applied Physics Express,* vol. 4, no. 4, p. 043005, 25 3 2011.

[22] C. Grezes, A. Rojas Rozas, F. Ebrahimi, J. G. Alzate, X. Cai, J. A. Katine, J. Langer, B. Ocker, P. Khalili Amiri and K. L. Wang, "In-plane magnetic field effect on switching voltage and thermal stability in electric-field-controlled perpendicular magnetic tunnel junctions," *AIP Advances,* 2016.

[23] S. Kanai, Y. Nakatani, M. Yamanouchi, S. Ikeda, F. Matsukura and H. Ohno, "In-plane magnetic field dependence of electric field-induced magnetization switching," *Applied Physics Letters,* vol. 103, no. 7, p. 072408, 12 8 2013.

[24] C. Grezes, F. Ebrahimi, J. G. Alzate, X. Cai, J. A. Katine, J. Langer, B. Ocker, P. Khalili Amiri and K. L. Wang, "Ultra-low switching energy and scaling in electric-field-controlled nanoscale magnetic tunnel junctions with high resistance-area product," *Applied Physics Letters,* 2016.

[25] Y. Shiota, T. Nozaki, S. Tamaru, K. Yakushiji, H. Kubota, A. Fukushima, S. Yuasa and Y. Suzuki, "Reduction in write error rate of voltage-driven dynamic magnetization switching by improving thermal stability factor," *Applied Physics Letters,* vol. 111, no. 2, p. 022408, 10 7 2017.

[26] K. Roy, S. Bandyopadhyay and J. Atulasimha, "Energy dissipation and switching delay in stress-induced switching of multiferroic nanomagnets in the presence of thermal fluctuations," *Journal of Applied Physics,* vol. 112, no. 2, p. 023914, 15 7 2012.

Chapter 3: Robustness and scalability of p-bits implemented with low energy barrier nanomagnets

Probabilistic (p-) bits implemented with low energy barrier nanomagnets (LBMs) have recently gained attention because they can be leveraged to perform some computational tasks very efficiently. Although more error-resilient than Boolean computing, p-bit based computing employing LBMs is, however, not completely immune to defects and device-to device variations. In some tasks (e.g. binary stochastic neurons for machine learning and p-bits for population coding), extended defects, such as variation of the LBM thickness over a significant fraction of the surface, can impair functionality. In this chapter, we have examined if unavoidable geometric device-to-device variations can have a significant effect on one of the most critical requirements for probabilistic computing, namely the ability to "program" probability with an external agent, such as a spin-polarized current injected into the LBM. We found that the programming ability is fortunately not lost due to reasonable device-to-device variations. The little variation in the probability versus current characteristic that reasonable device variability causes can be suppressed further by increasing the spin polarization of the current. This shows that probabilistic computing with LBMs is robust against small geometric variations, and hence will be "scalable".

3.1 Introduction

Probabilistic p-bits are random bits which fluctuate between 0 and 1 [1]. They are neither deterministic bits used in classical Boolean logic, nor qubits which are coherent superposition of 0 and 1. Probabilistic computing with p-bits encoded in the magnetization states of low energy barrier nanomagnets (LBMs) is extremely energy-efficient and far more error-resilient than

energy-efficient Boolean computing with nanomagnets, which is normally very error-prone [2]. Computing with p-bits has also been shown to excel in certain tasks such as combinatorial optimization [3], invertible logic [4] and integer factorization [5].

A popular platform for implementing p-bits is a low barrier nanomagnet (LBM) with two degenerate energy minima separated by a low energy barrier on the order of the thermal energy k_BT (k_B = Boltzmann constant and T = absolute temperature), as shown in Fig. 3.1 [1]. In such a nanomagnet, the magnetization will fluctuate between the two orientations corresponding to the two degenerate energy minima because of thermal fluctuations. If we take a snapshot of the magnetization at any instant of time, it will point in a random direction, as shown in Fig. 3.1. However, if its component along one of the two orientations is positive, then we will interpret the magnetization to represent the bit 1, while if it is negative, we will interpret it as bit 0. The bit will thus always fluctuate between 0 and 1 (sometimes 0 and sometimes 1) and act as a p-bit.

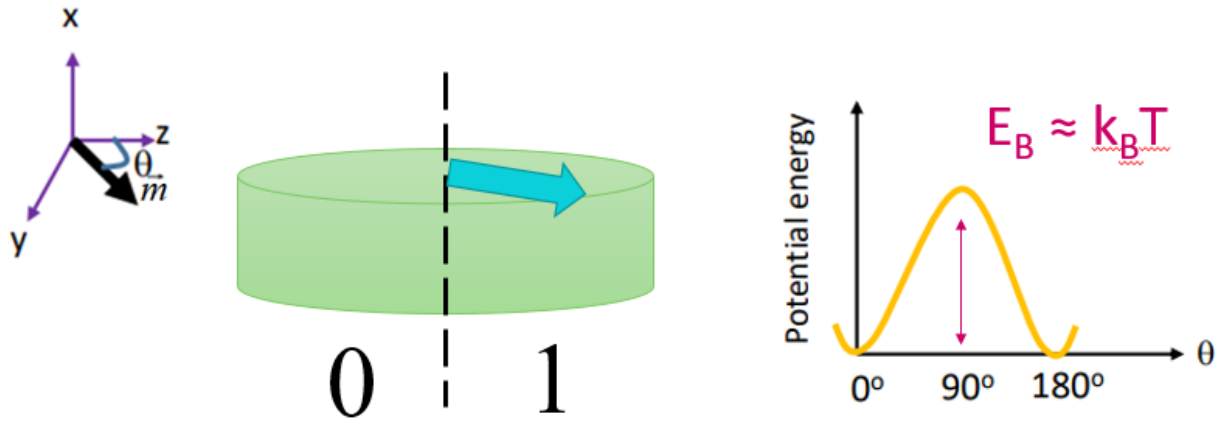

Fig. 3.1: A low energy barrier nanomagnet (left), showing two different representative bits based on whether the projection of magnetization along the z axis is positive (bit 1) or negative (bit 0). The states are separated by an energy barrier (right) close to the thermal energy.

One would measure the m_z component with a magnetic tunnel junction (MTJ) whose hard layer is magnetized in one direction along the z-axis, and hence the resistance of the MTJ will be a measure the m_z component. Compared to MTJs that are used for classical bits (Fig. 3.2(a)) where the switching time is on the order of nanoseconds, as seen in Chapter 2, MTJs using LBMs (Fig. 3.2(b)) can have switching time on the order of picoseconds. The resistance of MTJs with LBMs, of course, will not be binary and vary continuously between the high and low values since m_z component will vary continuously between -1 and +1. Hence, a threshold function is used in probabilistic computing to interpret all positive m_z component as bit 1 and all negative component as bit 0. We note that there is a chance of reading p-bits incorrectly this way, so usually repeated readings are averaged over to increase accuracy.

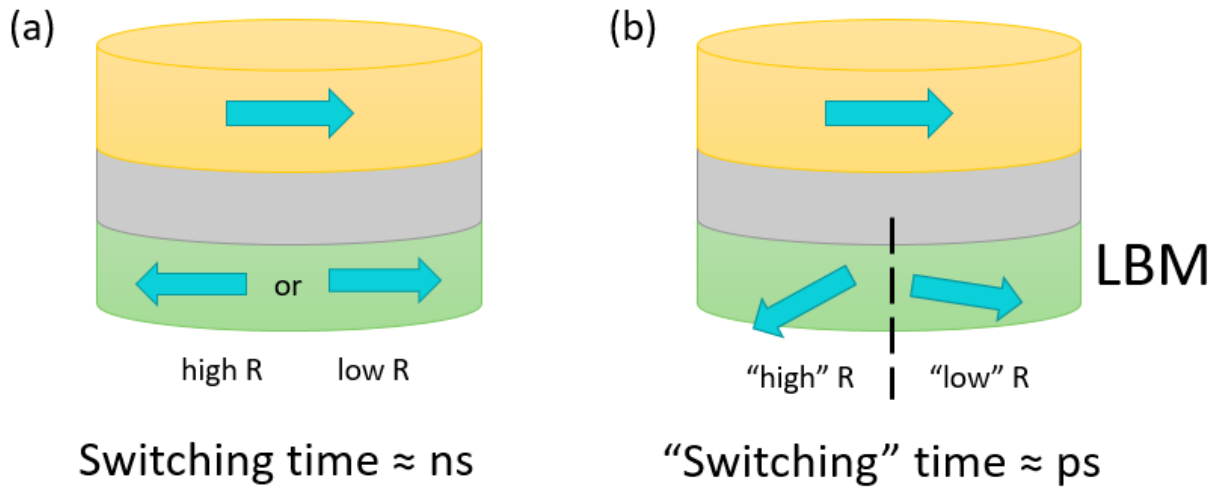

Fig. 3.2: (a) An MTJ for a classical bit, (b) An MTJ for a p-bit using a LBM as the soft layer.

If the energy barrier is symmetric between the two degenerate minima, then bits 0 and 1 will be generated with equal probability. However, one can change that by passing a spin polarized current through the nanomagnet with spins polarized along one of the two orientations. This will bias the probability, either toward 0 or toward 1, depending on the current's magnitude and spin

polarization (say, for example, 30% probability of 0 and 70% of 1 for a current of magnitude 1 μA with spins polarized in the direction representing bit 1). An example is shown in Fig. 3.3. Such an approach provides a means to "program" the probability, which is the basis of probabilistic computing. It is also the basis of binary stochastic neurons frequently used in stochastic neural networks and machine learning.

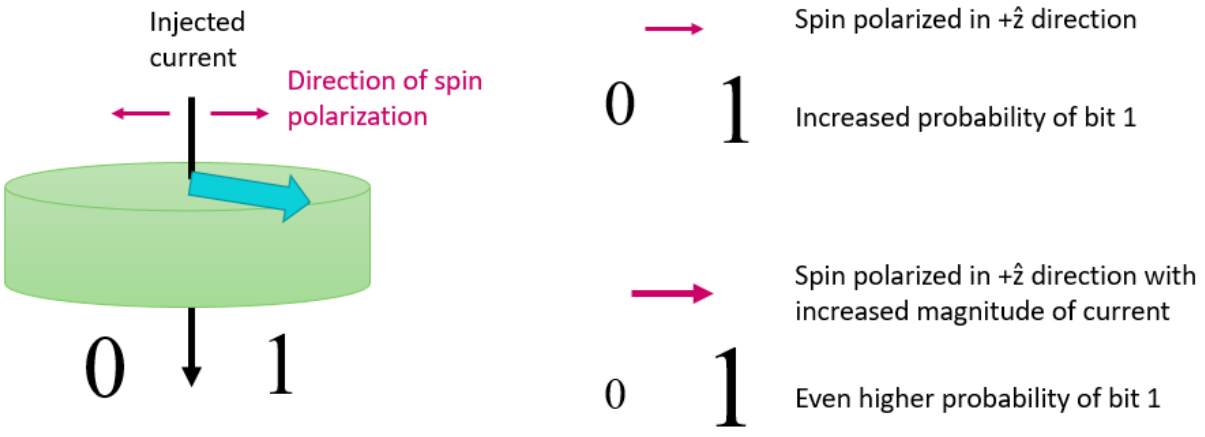

Fig. 3.3: (left) An LBM showing injected current that can have two directions of spin polarization. (right top) If the spin is polarized in the +ẑ direction, there is an increased probability of writing bit 1 over bit 0; (right bottom) if the magnitude of the spin polarized current is larger, the probability of writing bit 1 over bit 0 is even higher.

The programmability (or "control") will be lost if the magnitude of the current needed for a particular probability distribution (e.g. 30% for 0 and 70% for 1) varies significantly from one nanomagnet to another because of small variations in the nanomagnet's lateral dimensions or thickness. This will be debilitating for probabilistic computing and, at best, limit the number of p-bits that can be harnessed to build a "p-circuit", thereby making p-bits suffer from similar limitations on scalability that afflict qubits. It is this problem that we study. In the past, we have shown that extended defects in an LBM (e.g. thickness variation over a significant fraction of the surface) will radically alter the auto-correlation function of the magnetization fluctuation in time [6] and the fluctuation rate [7], which will, respectively, affect applications in, say, binary

stochastic neurons for machine learning [8] and population coding [9]. However, these are less serious than losing control over the probability because the latter is crucial to probabilistic computing. Therefore, it is critical to examine the effect of device-to-device variations caused by fabrication imperfections on the ability to control probability in LBMs.

To investigate this issue, we have carried out stochastic Landau-Lifshitz-Gilbert simulations to study magnetization fluctuations in an LBM (with in-plane magnetic anisotropy) at room temperature in the presence of a spin polarized current injected perpendicular to the plane of the LBM. These simulations allow us to generate the probability of bit 1 (encoded in the magnetization state of the LBM) as a function of the spin polarized current magnitude and polarization, and examine how this probability function varies with small variations in the nanomagnet's lateral dimensions and thickness. Our results show that the probability function is insensitive to reasonable variations. This is reassuring since it establishes that probabilistic computing with p-bits is not impaired by reasonable device-to-device variation and hence a large number of p-bits can be harnessed for p-circuits, meaning that p-bits are largely scalable.

3.2 Simulation Details

We consider an elliptical cobalt nanomagnet of nominal thickness 6 nm, major axis 100 nm and minor axis 99.7 nm (Fig. 3.1). This nanomagnet has in-plane magnetic anisotropy and because it has very small eccentricity (nearly circular), the shape anisotropy energy barrier separating the two stable orientations along the major axis (easy axis) is only 2.45 k_BT at room temperature. We follow the time evolution of the magnetization in this nanomagnet in the presence of thermal noise and a spin-polarized current injected perpendicular to plane with spin polarization along the major axis by solving the stochastic Landau-Lifshitz-Gilbert equation using MATLAB:

$$\frac{d\vec{m}(t)}{dt} = -\gamma\vec{m}(t)\times\vec{H}_{\text{total}}(t) + \alpha\left(\vec{m}(t)\times\frac{d\vec{m}(t)}{dt}\right)$$
$$+a\vec{m}(t)\times\left(\frac{\eta\vec{I}_s(t)\mu_B}{qM_s\Omega}\times\vec{m}(t)\right) + b\frac{\eta\vec{I}_s(t)\mu_B}{qM_s\Omega}\times\vec{m}(t) \qquad (1)$$

where

$$\hat{m}(t) = m_x(t)\hat{x} + m_y(t)\hat{y} + m_z(t)\hat{z} \qquad \left[m_x^2(t) + m_y^2(t) + m_z^2(t) = 1\right]$$
$$\vec{H}_{\text{total}} = \vec{H}_{\text{demag}} + \vec{H}_{\text{thermal}}$$
$$\vec{H}_{\text{demag}} = -M_s N_{d-xx} m_x(t)\hat{x} - M_s N_{d-yy} m_y(t)\hat{y} - M_s N_{d-zz} m_z(t)\hat{z}$$
$$\vec{H}_{\text{thermal}} = \sqrt{\frac{2\alpha kT}{\gamma\left(1+\alpha^2\right)\mu_0 M_s\Omega(\Delta t)}}\left[G^x_{(0,1)}(t)\hat{x} + G^y_{(0,1)}(t)\hat{y} + G^z_{(0,1)}(t)\hat{z}\right]$$

The last term in the right hand side of Equation (1) is the field-like spin transfer torque and the second to last term is the Slonczewski torque. The inclusion of the field like torque is necessary since the magnetization state of the nanomagnet will have to be read by a magnetic tunnel junction, which will result in a field-like torque. The coefficients *a* and *b* depend on device configurations and following [10], we will use the values $a = 1,\ b = 0.3$. Here $\hat{m}(t)$ is the time-varying magnetization vector in the nanomagnet normalized to unity, $m_x(t)$, $m_y(t)$ and $m_z(t)$ are its time-varying components along the x-, y- and z-axis, $\vec{H}_{\text{demag}}$ is the demagnetizing field in the soft layer due to shape anisotropy and $\vec{H}_{\text{thermal}}$ is the random magnetic field due to thermal noise [11]. The different parameters in Equation (1) are: $\gamma = 2\mu_B\mu_0/\hbar$ (gyromagnetic ratio), α is the Gilbert damping constant, μ_0 is the magnetic permeability of free space, M_s is the saturation magnetization of the magnetostrictive soft layer, kT is the thermal energy, Ω is the volume of the nanomagnet given by $\Omega = (\pi/4)a_1a_2a_3$, a_1 = major axis, a_2 = minor axis, and a_3 = thickness, Δt is the time step used in the simulation (0.1 ps), and $G^x_{(0,1)}(t)$, $G^x_{(0,1)}(t)$ and $G^x_{(0,1)}(t)$ are three uncorrelated

Gaussians with zero mean and unit standard deviation [11]. The quantities $N_{d-xx}, N_{d-yy}, N_{d-zz}$ $\left[N_{d-xx}+N_{d-yy}+N_{d-zz}=1\right]$ are calculated from the dimensions of the nanomagnet following the prescription of ref. [12]. We assume that the charge current injected into the nanomagnet is $\vec{I}_s(t)$ and that the spin polarization in the current is η. The spin current is given by $\eta\vec{I}_s(t)=\eta\left|\vec{I}_s(t)\right|\hat{z}$ where $\hat{z}$ is the unit vector along the major axis as shown in Fig. 3.1. The various parameters for the simulation are given in Table 3.1.

Table 3.1 – Parameters used in the simulations

Parameter	Value
Saturation magnetization (M_s)	1.1×10^6 A/m
Gilbert damping (α)	0.01
Temperature (T)	300 K
Spin polarization (η)	0.3, 0.7
Major axis of soft layer (a_1)	100 nm
Minor axis of soft layer (a_2)	90, 98, 99, 99.7 nm
Thickness of soft layer (a_3)	5, 6, 7, 15 nm

Stochastic Landau-Lifshitz-Gilbert simulations are run in the manner of ref. [11]. We start the simulation for any given magnitude and polarization of the spin polarized current with the initial value $m_x(0)=m_z(0)=0;\ m_y(0)=1,$ i.e. the magnetization is initially pointing in one direction along the minor axis. We run the simulation for 10 ps and note the final value of m_z. If it is positive, then we interpret the magnetization state to represent the bit 1, while if it is negative, we interpret it as bit 0.

3.3 Results and Discussion

We run 10,000 simulations of the magnetization dynamics for each value of spin polarized current (in steps of 0.1 mA) and calculate the fraction of simulations where the final state after 10

ps represents the bit 1. That fraction is the probability of bit 1 or *P(1)*. If we had monitored the bit as a function of time, this would have been the probability of observing the bit as 1, based on ergodicity. Obviously, *P(0)* is always 1 – *P(1)*. In Fig. 3.4, we show *P(1)* as a function of the magnitude and spin polarization of the spin polarized current for four different nanomagnet thicknesses of 5 nm, 6 nm, 7 nm and 15 nm. Positive current corresponds to spin polarization along the +z-axis and negative current corresponds to polarization along the –z-axis. We plot the results for two different degrees of spin polarization η in the current: 30% and 70%.

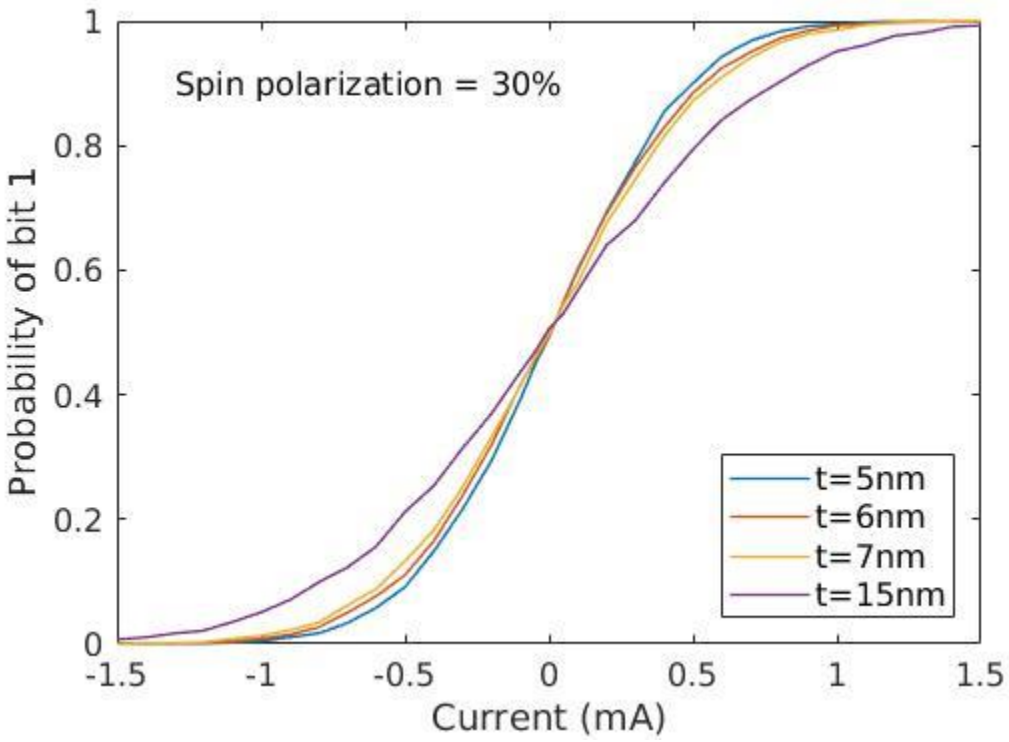

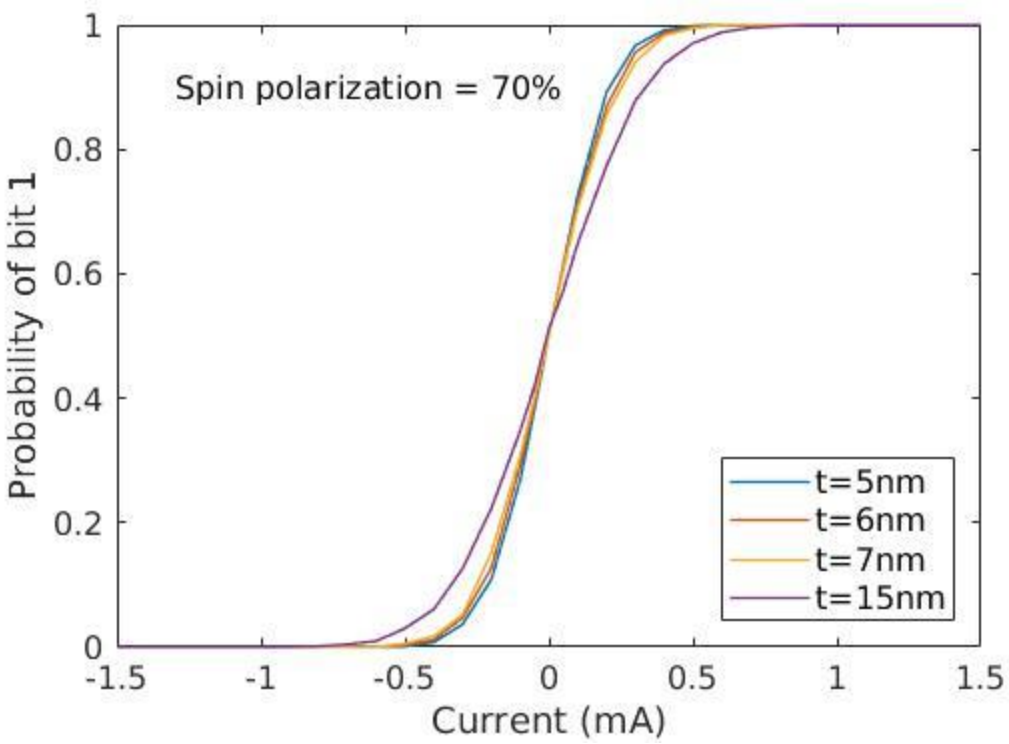

Fig. 3.4: The probability of bit 1 as a function of spin polarized current for four different nanomagnet thicknesses of 5, 6, 7 and 15 nm. The major axis is 100 nm and the minor axis is 99.7 nm. The results are plotted for two different degrees of spin polarization in the current: 30% (top) and 70% (bottom). The variation in the probability at any given current is reduced at higher spin polarization. Positive value of the current corresponds to spin polarization in the +z direction and negative values correspond to spin polarization in the –z direction. For these thicknesses, the energy barrier heights are respectively 1.7 k_BT, 2.45 k_BT, 3.33 k_BT and 15.29 k_BT

In Fig. 3.5, we show *P(1)* as a function of the magnitude and degree of spin polarization in the spin polarized current for four different minor axis dimensions of 99.7 nm, 99 nm, 98 nm and 90 nm (the major axis is fixed at 100 nm and the thickness is fixed at 6 nm). We keep the aspect ratio (major axis to minor axis dimension ratio) small enough so that the energy barrier in the nanomagnet remains sufficiently low (the energy barriers are 2.45 k_BT, 8.16 k_BT, 16.34 k_BT and 81.62 k_BT for the four different minor axis dimensions). When the minor axis is 90 nm, the energy barrier is obviously too high to qualify the nanomagnet as a "low barrier nanomagnet". Yet, even with that much variation in the barrier height (3300%), the probability curves change very little, showing that the probability versus current characteristic is very insensitive to barrier height

variation in this regime. Comparing Figs. 3.4 and 3.5, we find that the probability versus current characteristic is much more insensitive to lateral dimension variation than thickness variation. This is fortunate since lateral dimension is more difficult to control since it is defined by lithography than thickness which is defined by film growth. In Fig. 3.5, we show the plots for two different degrees of spin polarization η in the current: 30% (top) and 70% (bottom). The higher degree of spin polarization again suppresses the variability just as in the case of thickness variation.

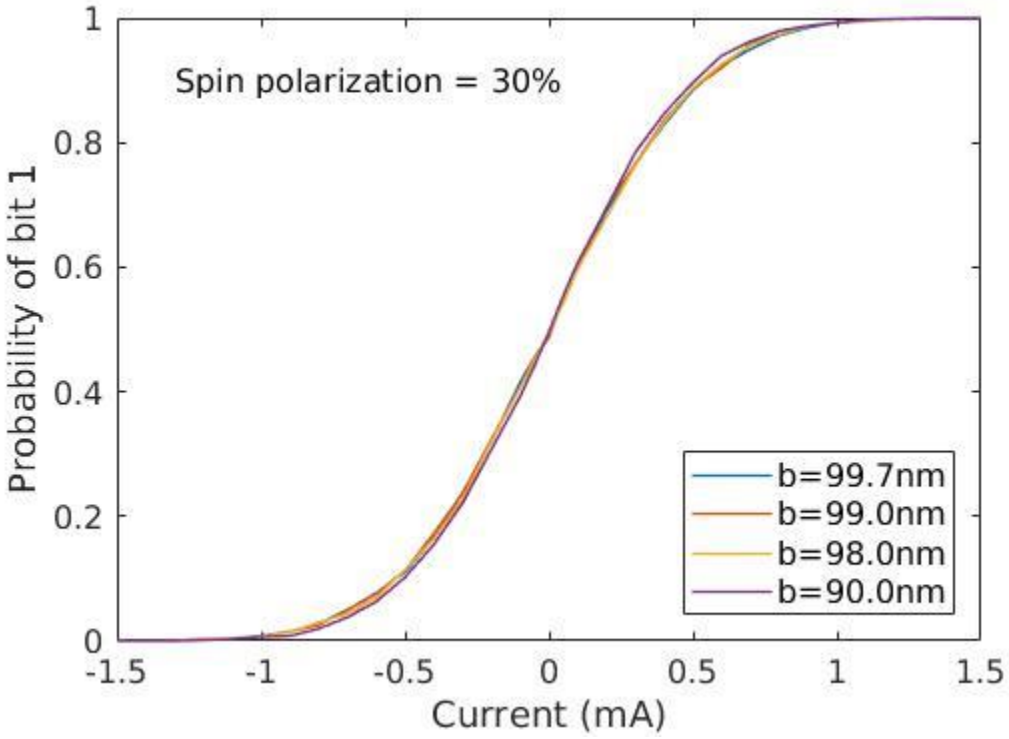

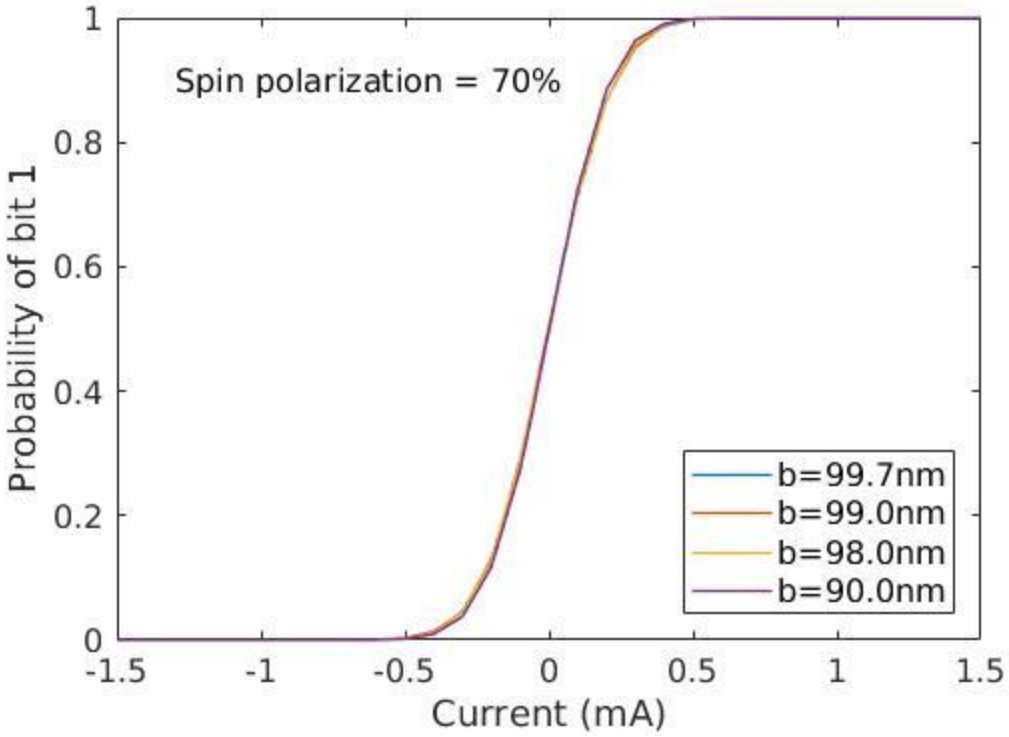

Fig. 3.5: The probability of bit 1 as a function of spin polarized current for four different nanomagnet minor axis dimensions of 90, 98, 99 and 99.7 nm. The major axis dimension is fixed at 100 nm and the thickness is 6 nm. The results are plotted for two different degrees of spin polarization in the current: 30% (top) and 70% (bottom). As in Fig. 3.4, the variation is reduced at higher spin polarization.

3.4 Conclusion

Clearly, the plots show that the probability curves are not affected much by reasonable variations in either thickness or lateral dimensions. In the case of thickness variation, we see a significant difference only for the 15 nm thickness. Variation in thickness by ±1 nm is reasonable since nanomagnets are usually fabricated on substrates with surface roughness of 0.3 nm, but the 15 nm thickness would require the thickness to vary by 9 nm from the target thickness of 6 nm and is not reasonable. Therefore, we can conclude that the probability curves are not affected significantly by reasonable thickness variations.

Variation in the lateral dimension (minor axis length) is even more forgiving. A variation of more than 9 nm, which is 9% of the minor axis dimension, does not make a significant difference in the probability curves. The little variation that there is can be further suppressed by increasing the degree of spin polarization in the current.

Increasing the degree of spin polarization also decreases (expectedly) the magnitude of the current needed to pin the bit to either 0 or 1. All this is reassuring since it implies that the "control" over p-bits exercised with spin polarized current is not impaired by reasonable device-to-device variations and therefore a fairly large number of p-bits can be harnessed for "p-circuits" in many applications, i.e. p-bits are generally "scalable". This is in sharp contrast to qubits where only a small number can be entangled for quantum operations (the largest number entangled so far appears to be 53 [13]) because of decoherence. Classical p-bits do not suffer from decoherence and their scalability does not appear to be severely limited by reasonable device-to-device variations either. Some specific applications may still be vulnerable to defects [5, 6], but the practicality of implementing p-bits with LBMs is unassailable.

Finally, we clarify that the variations we have considered are uniform variations in thickness and lateral dimensions. Studying the effect of spatially inhomogeneous variations (e.g. surface roughness) would require running micromagnetic simulations instead of macrospin simulations (stochastic Landau-Lifshitz-Gilbert). Since running 10,000 micromagnetic simulations for each current value will be computationally prohibitive, the effect of spatially inhomogeneous variations (e.g. surface roughness) has not been address here.

Chapter 3 References

[1] K. Y. Camsari, B. M. Sutton and S. Datta, “p-bits for probabilistic spin logic”, Appl. Phys. Rev., 6, 011305, 2019. [Online]. Available: https://doi.org/10.1063/1.5055860.

[2] D. Winters, M. A. Abeed, S. Sahoo, A. Barman and S. Bandyopadhyay, “Reliability of magnetoelastic switching of nonideal nanomagnets with defects: A case study for the viability of straintronic logic and memory”, Phys. Rev. Appl., 11, 034010, 2019. [Online]. Available: http://dx.doi.org/10.1103/PhysRevApplied.12.034010.

[3] B. Sutton, K. Y. Camsari, B. Behin-Aein, and S. Datta, “Intrinsic optimization using stochastic nanomagnets,” Sci. Rep., 7 44370 , 2017. [Online]. Available: https://doi.org/10.1038/srep44370.

[4] K. Y. Camsari, R. Faria, B. M. Sutton, and S. Datta, “Stochastic p-bits for invertible logic,” Phys. Rev. X, 7, 031014, 2017. [Online]. Available: https://link.aps.org/doi/10.1103/PhysRevX.7.031014.

[5] W. A. Borders, A. Z. Pervaiz, S. Fukami, K. Y. Camsari, H. Ohno and S. Datta, “Integer factorization using stochastic magnetic tunnel junctions”, Nature, 573, 390, 2019. [Online]. Available: https://doi.org/10.1038/s41586-019-1557-9.

[6] M. A. Abeed and S. Bandyopadhyay. “Low energy barrier nanomagnet design for binary stochastic neurons: Design challenges for real nanomagnets with fabrication defects”, IEEE Magnetics Letters, 10, 4504405, 2019. [Online] Available: DOI: 10.1109/LMAG.2019.2929484.

[7] M. A. Abeed and S. Bandyopadhyay, “Sensitivity of the power spectra of thermal magnetization fluctuations in low barrier nanomagnets proposed for stochastic computing to in-plane barrier height variations and structural defects”, SPIN, 9, 2050001, 2019.

[8] O. Hassan, R. Faria, K. Y. Camsari, J. Z. Sun, and S. Datta, “Low barrier magnet design for efficient hardware binary stochastic neurons,” IEEE Magnetics Lett., 10, 4502805, 2019. [Online]. Available: doi: 10.1109/LMAG.2019.2910787

[9] A. Mizrahi, T. Hirtzlin, A. Fukushima, H. Kubota, S. Yuasa and J. Grollier, “Neurallike computing with populations of super-paramagnetic basis functions”, Nature Commun., 9, 1533, 2018. [Online] Available: DOI: 10.1038/s41467-018-03963-w.

[10] K. Roy, S. Bandyopadhyay and J. Atulasimha, “Metastable state in a shape anisotropic single-domain nanomagnet subjected to spin-transfer-torque”, Appl. Phys. Lett., 101, 162405, 2012. [Online] Available: https://doi.org/10.1063/1.4761250.

[11] K. Roy, S. Bandyopadhyay and J. Atulasimha, “Energy dissipation and switching delay in stress-induced switching of multiferroic nanomagnets in the presence of thermal fluctuations”, J. Appl. Phys., 112, 023914, 2012. [Online]. Available: https://doi.org/10.1063/1.4737792 and references therein.

[12] S. Chikazumi, Physics of Magnetism (Wiley, New York, 1964). [13] A. Cho, “Google claims quantum computing milestone”, Science, 365, 1364, 2019.

Chapter 4: Systematic study of sputtering deposition rates towards reliable growth calibrations for magnetic device growth

Magnetic tunnel junctions (MTJs) for memory cells and low barrier nanomagnets (LBMs) for probabilistic computing each require ultrathin (nm or sub-nm resolution with monolayer accuracy) ferromagnetic layers of well-controlled thickness. Therefore, it is imperative to study optimal methods for uniform and well-controlled thin film growth. Precise control over the thin film deposition rate is essential for successful fabrication of ultrathin films and multilayered heterostructures, particularly for nm-thick magnetic layers using in magnetic devices. This demands judicious calibration of the thin film growth rate and *in-situ* monitoring of the deposited thickness. The work described in this chapter pertains to growth of thin magnetic films and was conducted as a guest researcher at the National Institute of Standards and Technology (NIST).

4.1 Introduction

The Magnetic Engineering Research Facility (MERF) within the Materials Science and Engineering Division (MSED) at NIST is a specially designed facility for the deposition and characterization of magnetic thin films. The central piece of equipment in the facility is a multi-chamber ultrahigh vacuum sputtering system with 13 sputtering guns – 11 in the main chamber and 2 in an attached analytical chamber. Sputtering is a form of physical vapor deposition where an inert gas, such as argon, is ionized and an accelerating voltage causes the argon ions to collide with target materials, ejecting neutral target atoms towards a substrate. Sputtering targets installed include magnetic device related materials and device support related materials, such as adhesion, buffer, and capping materials. There are quartz crystal monitors (four in the main chamber and one

for each gun in the analytical chamber) to monitor the deposition thickness during sample growth. A stage mounted on a long transfer rod allows for sample movement between the chambers, and a heater stage allows for pre-, during, or post deposition annealing. Both stages have controllable azimuthal rotation to improve lateral deposition uniformity and can be tilted to permit adjustments of the angle between the substrate surface normal and deposition sources.

After several upgrades to the sputtering system, it was necessary to obtain new deposition rate calibrations before more advanced structure growth could occur. A procedure was developed to ensure a systematic process to determine the deposition rate for all materials currently installed in the chamber and those that might be installed in the future. Thickness measurements were done using two methods, x-ray reflectivity and atomic force microscopy, compare alternative techniques for thickness evaluation. Deposition rate data was compiled into a user-interface to build sample recipes for quick and accurate record keeping.

4.2 Experimental Details

Samples were grown on thermally oxidized Si (100) substrates that were first cleaned and degreased by sonicating in acetone and boiling in isopropyl alcohol. Each film was grown by direct current magnetron sputtering at various power levels, except MgO which was grown by radio frequency sputtering, in a chamber with base pressure less than 1.0×10^{-9} Torr and a working Ar pressure of 3 mTorr. Magnetron sputtering uses magnetic fields to confine the ionized plasma close to the target surface and trap electrons from the negative cathode, increasing the ionization rate among the argon atoms, and leading to a higher deposition rate than non-magnetron sputtering. Radio frequency (RF) sputtering, in contrast, uses the alternating current signal to periodically attract and eject charge build-up and is essential for insulating oxides such as MgO. For each material, a series of samples with different deposition times, such as 5, 10, and 20 minutes, was

prepared. For several magnetic materials, a second series was collected with the sample stage tilted such that the surface normal was aligned with the surface of the sputtering target to deliver higher sputtering rates and possibly different kinetics compared to the film sputtered with the substrate surface normal tilted 30 degrees away from the sputtering target. Data was collected for twelve distinct materials but is shown throughout this chapter for the ruthenium series only, as an illustrative example of the process.

Two different measurement methods were used to estimate the film thickness: x-ray reflectivity (XRR) and step heights from atomic force microscopy (AFM). Both methods have some benefits and drawbacks. XRR is generally very precise, can look at a sizeable sample area to statistically eliminate anomalies, and does not require physical interaction with the sample. AFM is relatively quick for a very small sample area but has a finite measurement limit determined by the size and shape of the tip.

An example AFM step height image for the ruthenium 10 min deposition sample is shown below in Fig. 4.1. An abrupt edge was created for step height estimation using a quick liftoff technique: a sharpie mark shadowed a small section of the sample and was easily removed after deposition with isopropyl alcohol, removing the metal on top with it. An average step height was taken over an area with a smooth edge (lacking high rough edges like at the bottom of the image), indicated by the white box in Fig. 4.1. The XRR data for the same sample is shown in Fig. 4.2. After the XRR data was collected, fitting software was used to construct a model for the roughness, density, and thickness of the films. Both thickness measurements were compared to one another and to the readings from the crystal monitors in the chamber during deposition. An example of this data for the ruthenium sample series is shown in Table 4.1.

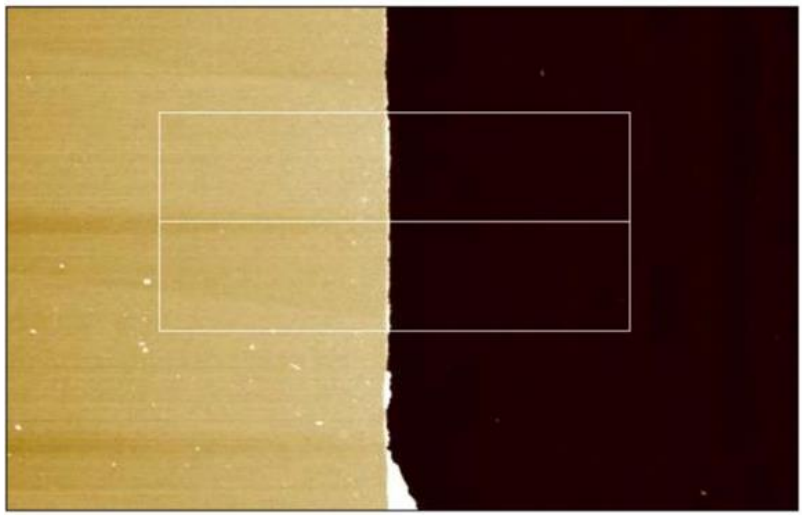

Fig. 4.1: An AFM step height image of a ruthenium film (left) grown for 10 minutes.

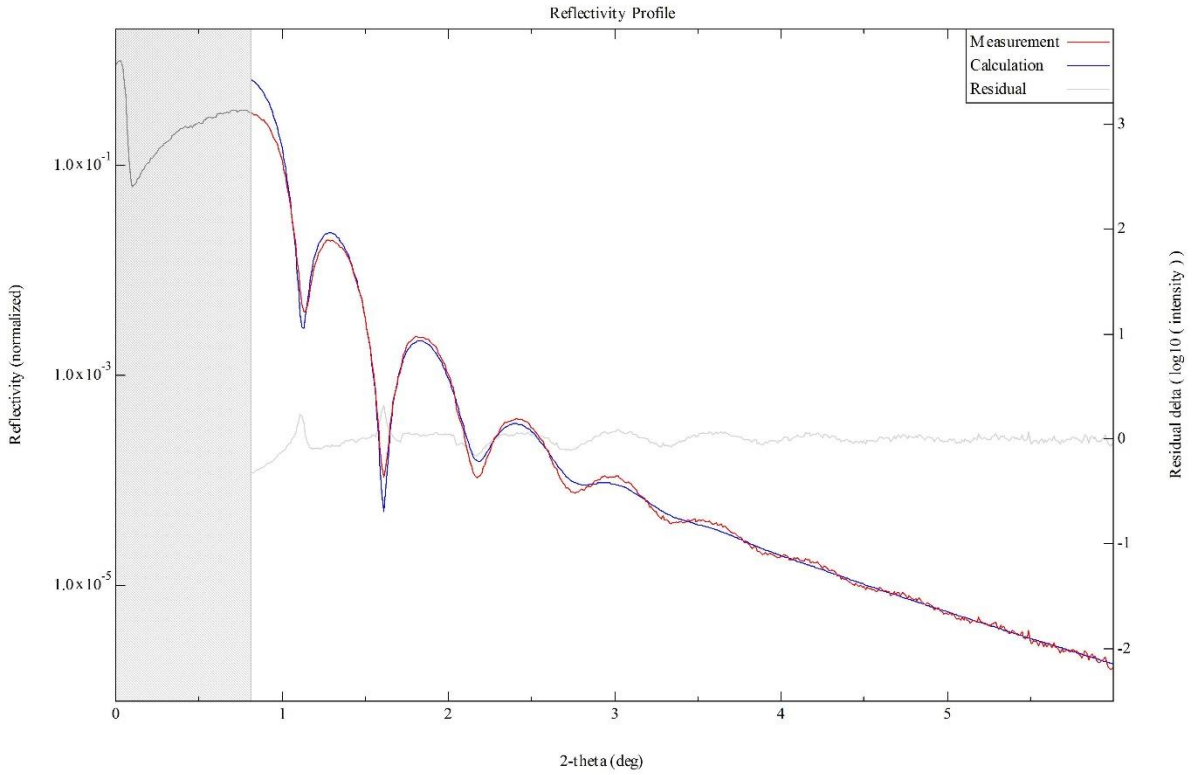

Fig. 4.2: XRR data for the 10 min deposition ruthenium sample with measured data shown in red and the data fit shown in blue

Table 4.1 – Crystal monitor, XRR, and AFM thickness measurements for the ruthenium calibration series

Description	Crystal 1 (nm)	Crystal 2 (nm)	Crystal 3 (nm)	Crystal 4 (nm)	XRR (nm)	AFM (nm)
Ru 5 min	3.1	5	7.5	1.5	8.33	8.3
Ru 10 min	6	9.6	15	2.8	14.06	14.1
Ru 20 min	10.6	17.4	26.5	5	24.64	24.3

After XRR and AFM thicknesses were obtained, deposition rates were estimated based on the thickness measurements from XRR. The XRR data sets were found to be more consistent across the different deposition times for each sample series, particularly for some of the shorter depositions. AFM thicknesses were used for comparison to the XRR data. An average deposition rate was calculated from the samples series. Additionally, the average deposition rates were calculated with more weight given to the shorter and longer deposition times, designated "weighted long" and "weighted short." These rates could be used for more accurate depositions when the deposition time is significantly outside the calibration time window. The tooling factor was also calculated for each material and each crystal monitor. The tooling factor, TF, is defined as the ratio of the thickness measured on the sample to the thickness measured by the crystal monitor. The results for the ruthenium sample series are shown in Table 4.2.

Table 4.2 – Deposition rates and tooling factors for ruthenium sample series

Description	Deposition rate (nm_{XRR}/min)		Deposition rate (nm/min)		TF
Ru 5 min	1.67	Average:	1.44	Crystal 1	2.5
Ru 10 min	1.41	Weighted long:	1.34	Crystal 2	1.5
Ru 20 min	1.23	Weighted short:	1.53	Crystal 3	1.0
				Crystal 4	5.2

4.3 Recipe Builder Results

Deposition rate calibrations were used as the basis for building a user interface within a macro-enhanced excel spreadsheet for sample recipe creation and record keeping purposes. An example of a recipe created using this module is shown in Fig. 4.4. The process of using the recipe builder is as follows:

1. The materials being deposited for each layer are selected from a drop-down menu in the 'Material' column. Options are included for tilted magnetic material depositions.
2. The stage where the growth will occur is selected next; there is another drop-down menu for either the heater stage or the long-transfer rod stage. Based on this selection and the material selection, the 'Long Transfer position' column is automatically populated.
3. The 'Angle' column is automatically populated based on the tilted position necessary for the different magnetic materials.
4. The 'Temp' column is pre-populated to standard chamber temperature of 27 °C but can be changed by the user.
5. The 'Layer Type' is selected from a drop-down menu with the options: Single, Co-sputter, or Bilayers.
6. The 'Pressure' column is pre-populated with standard pressures of 3 mTorr of Ar and 0 mTorr of N_2 but can be changed by the user.
7. The 'Power' column is automatically populated when the material is selected. The power is set to the power that was used during the deposition rate calibration. If the user changes this power, a linear extrapolation is used to calculate the modified deposition rate.
8. The 'Final Thickness' is user-input. Based on this thickness, the times are automatically calculated from the deposition rates for each material.

9. An image of the sample is automatically created below the recipe.
10. There are buttons next to the recipe (not shown below) to clear out the user inputs and to save and print a copy of the recipe.

Layer Number	Material	Stage	Angle	Temp (°C)	Long Transfer position	Layer Type	Pressure (mTorr)		Power (W)	Final Thickness (nm)	Required Time (s)	Time (h:mm:ss)
							Ar	N_2				
1	Ta	Long	0	27	0	Single	3	0	60	3	108.2	0:01:48
2	MgO	Long	0	27	704	Single	3	0	50	2	61.6	0:01:02
3	CoFeB_TILT	Heater	-30	27	-150	Single	3	0	60	0.8	44.8	0:00:45
4	Ta	Heater	0	27	-150	Single	3	0	60	2	72.2	0:01:12

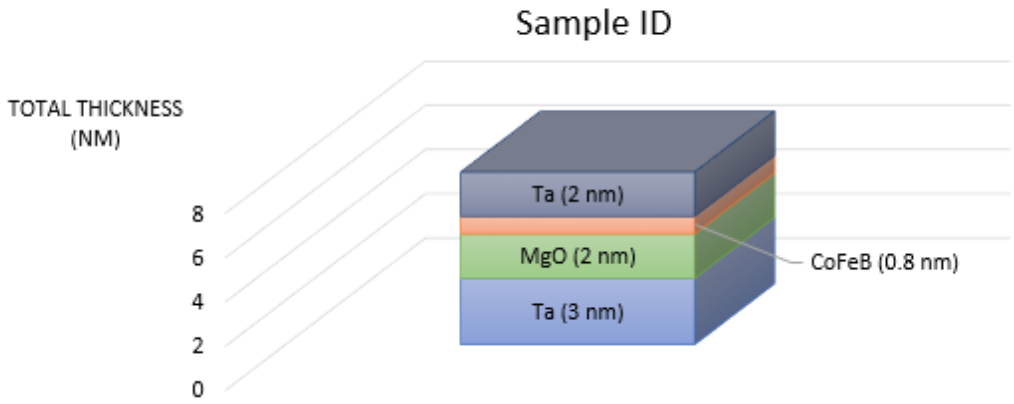

Fig. 4.4: Sample deposition recipe created using the Recipe Builder module

4.4 Conclusion

Deposition rate calibrations were obtained for the dual-chamber, ultrahigh vacuum sputtering system in the Magnetic Engineering Research Facility at NIST. A procedure was developed for future deposition rate calibrations during this process. Thicknesses were measured for all samples using both XRR and AFM. These growth rates were integrated into a "recipe builder" user-interface for sample creation and documentation. Having a convenient and systematic method for calibrating growth rates and creating sample recipes brings order and

usefulness to a piece of equipment with significant capabilities. This systematic control is required to produce the kind of ultrathin layers and engineered interfaces for applications discussed in this thesis.

Chapter 5: Effect of CoFe dusting layer and annealing on the magnetic properties of sputtered Ta/W/CoFeB/CoFe/MgO layer structures

In this chapter, we explored the effect of a CoFe wedge inserted as a dusting layer (0.2 nm – 0.4 nm thick) at the CoFeB/MgO interface of a sputtered Ta(2 nm)/W(3 nm)/CoFeB(0.9 nm)/MgO(3 nm)/Ta(2 nm) film – a typical structure for spin-orbit torque devices. Films were annealed at temperatures varying between 300 ºC and 400 ºC in an argon environment. Ferromagnetic resonance studies and vibrating sample magnetometry measurements were carried out to estimate the effective anisotropy field, the Gilbert damping, the saturation magnetization and the dead layer thickness as a function of the CoFe thickness and across several annealing temperatures. While as-deposited films present only easy-plane anisotropy, a transition along the wedge from in-plane to out-of-plane was observed across several annealing temperatures, with evidence of a spin-reorientation transition separating the two regions.

5.1 Introduction

Ultrathin CoFeB films have been essential to many spintronic applications since the discovery of perpendicular magnetic anisotropy in CoFeB/MgO magnetic tunnel junctions [1]. Perpendicular magnetic anisotropy (PMA) is critical for achieving next-generation high density spintronic devices with low power consumption due to the achievability of high thermal stability and low critical switching current [2,3]. Other materials systems are capable of attaining perpendicular anisotropy, but when the junction size is reduced, both high anisotropy energy density (to maintain PMA) and low damping (to maintain low critical switching current) are required; most material systems can satisfy the first condition and not the second [1]. These

conditions are both satisfied by CoFeB/MgO magnetic tunnel junctions. Manipulating magnetic properties of ultrathin CoFeB films through interface engineering is an area of intense research within the spintronics community.

Properties are highly dependent on the choice of layer structure, and many studies have focused on the effects and optimization of various top and bottom film structures [4–7]. Layered CoFeB/MgO structures with heavy metal underlayers, particularly tungsten (W), were shown to have strong PMA, low Gilbert damping, and high thermal stability [6–9]. Interfacial anisotropy is found to be greater with a W buffer compared to a Ta buffer [10]. Thin capping layers of Ta were also shown to increase interfacial anisotropy [11,12]. Devices must maintain characteristics and performance over a range of annealing temperatures up to 400 °C, a standard compatibility requirement for CMOS processing.

Here we look at insertion of very thin CoFe layer at CoFeB/MgO interface to determine its effect on the underlying magnetic properties and annealing stability – key factors for spintronic applications involving CoFeB. The CoFe insertion layer lateral thickness variation across a 60 mm long Si substrate was deliberately engineered to cover an adequately large thickness range of the combined CoFeB and CoFe complex that would exhibit a preferred perpendicular magnetization at the thinner range and a preferred easy-plane magnetization at the higher thicknesses. The success of this approach was demonstrated in samples annealed at temperatures exceeding 350 °C. In fact, the sample annealed at 400 °C exhibited regions in which our measurements estimated a modest perpendicular magnetic anisotropy energy. The role of CoFe thickness on the magnetic and annealing properties will be discussed.

5.2 Experimental Details

Samples were produced in which an ultrathin CoFe wedge layer was inserted between the CoFeB and MgO layers in a thin film heterostructure grown on a thermally oxidized Si substrate. Each layer of the deposited film was grown by direct current at constant power (100 W) (excepting the MgO layer, grown by radio frequency at 150 W) magnetron sputtering at room temperature in a chamber with base pressure less than 1.3×10^{-6} Pa (1.0×10^{-8} Torr) and a working Ar pressure of 0.4 Pa (3 mTorr). Each sputtering target (CoFe, Ta, CoFeB, MgO) was a 2" sputtering target. The structure of the sample was Ta (2 nm)/W (3 nm)/$Co_{20}Fe_{60}B_{20}$ (0.9 nm)/$Co_{50}Fe_{50}$ (0.2 nm - 0.4 nm)/MgO (3 nm)/Ta (2 nm); the structure is illustrated in Fig. 5.1. Note that the lattice constant of crystalline CoFe is approximately 0.28 nm, and at some points along the wedge, there is likely partial coverage of zero, one, or two monolayers. However, the average, or nominal, film thickness of the wedge is expected to be 0.2 nm – 0.4 nm based on carefully calibrated deposition rates.

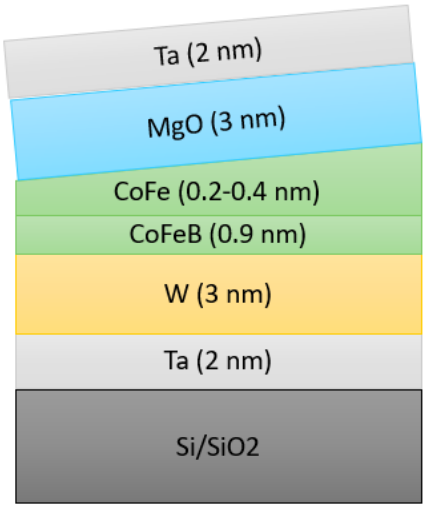

Fig. 5.1: The layer structure of the sample.

Nominal film deposition rates were estimated from calibration samples, and thicknesses were confirmed from x-ray reflectivity measurements of the wedge sample, as shown in Fig. 5.2. The calibrated deposition rates (Å/s) are: CoFe (0.34); Ta (0.5); CoFeB (0.32) and MgO (0.06).

Ta, CoFeB, and MgO layers were grown with the substrate surface normal confocal with the sputtering targets. However, the CoFe layer was deposited after having translated the center of the substrate manipulator to a displacement that is 45° away from the sputtering gun surface normal. Such an oblique orientation enabled us to obtain a continuously varying CoFe layer along the direction of the substrate oriented radially outward from the focus of the CoFe sputtering gun. Calibration of the nominal thicknesses of the thickness wedge described in this manuscript was carried out on a much thicker CoFe wedge calibration sample, whose x-ray reflectivity results are shown in Fig. 5.3.

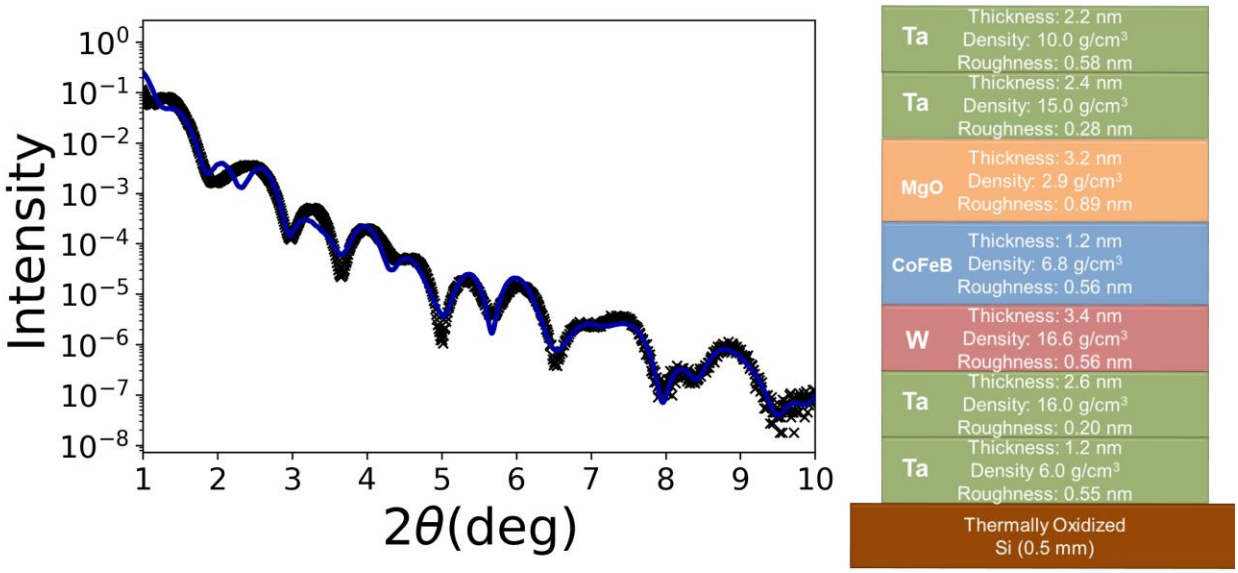

Fig. 5.2: X-ray reflectivity scan of complete sample stack. The blue solid line is the fit to the intensity data (black points). Details of sample stack shown on right.

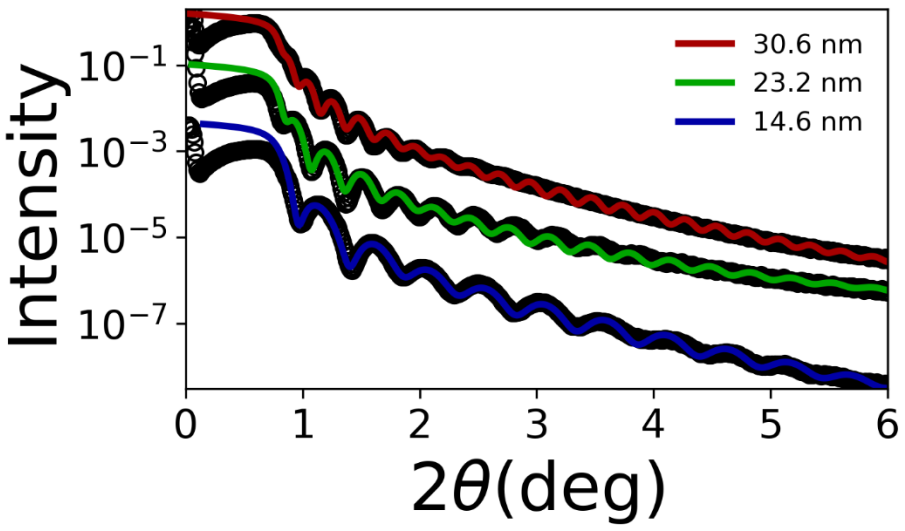

Fig. 5.3: Exemplary x-ray reflectivity scans of our CoFe wedge used for deposition rate calibration. Intensity data taken at three positions on wedge: 30.6 nm (9 mm from thick edge); 23.2 nm (29 mm from thick edge); 14.6 (48 mm from thick edge). The colored solid lines are fits to the intensity data (open circles). The average lateral deposition rate gradient is estimated to be 4.50 (Å/s)/m, with an average deposition rate in the center estimated at 0.340 Å /s.

In order to promote depletion of the B-content in CoFeB and to promote crystallization of the CoFeB, CoFe, and MgO layers, samples were annealed post-deposition using a rapid thermal annealer (RTA) [4,13,14]. Annealing was carried out in an argon environment for 30 minutes at 300 °C, 325 °C, 350 °C, and 400 °C, temperatures known to induce crystallization and promote perpendicular magnetic anisotropy [7,15]. Individual samples were cleaved from the wedge at representative positions along the thickness gradient to evaluate the role of CoFe insertion layer thickness on magnetic properties and the effects of annealing.

Magnetic properties of both the as-deposited and annealed samples were measured with a vibrating sample magnetometer (VSM) and broadband ferromagnetic resonance (FMR). Estimation of the saturation magnetization and magnetic dead layer thickness were carried out using a Microsense VSM. Magnetic moment was measured along the applied field direction with fields applied within the plane of the film. Measurements of the ferromagnetic resonance field and

linewidth versus frequency were taken to estimate the perpendicular anisotropy field and Gilbert damping in the films. Samples were placed film-side down on a coplanar waveguide within an electromagnet with a field range up to 1.5 T and frequency excitation range 1-50 GHz [16]. All measurements were conducted with the applied magnetic field aligned in the plane of the thin film samples.

5.3 Results and Discussion

Magnetometry was used to evaluate the saturation magnetization and dead layer thickness amongst the samples and under the various annealing conditions. Magnetic moment was measured along the applied field direction with fields applied within the film plane. Saturation moment was estimated for each sample from its magnetic hysteresis loop by taking the average of the saturation values from maximum and minimum applied fields. Magnetic hysteresis plots for all samples are shown in Figs. 5.4-5.8. The areal saturation magnetization was plotted against the combined thickness of the CoFeB and CoFe layers, as shown in Fig. 5.9. A standard error of 5% was included from estimations of the saturation moment and sample area.

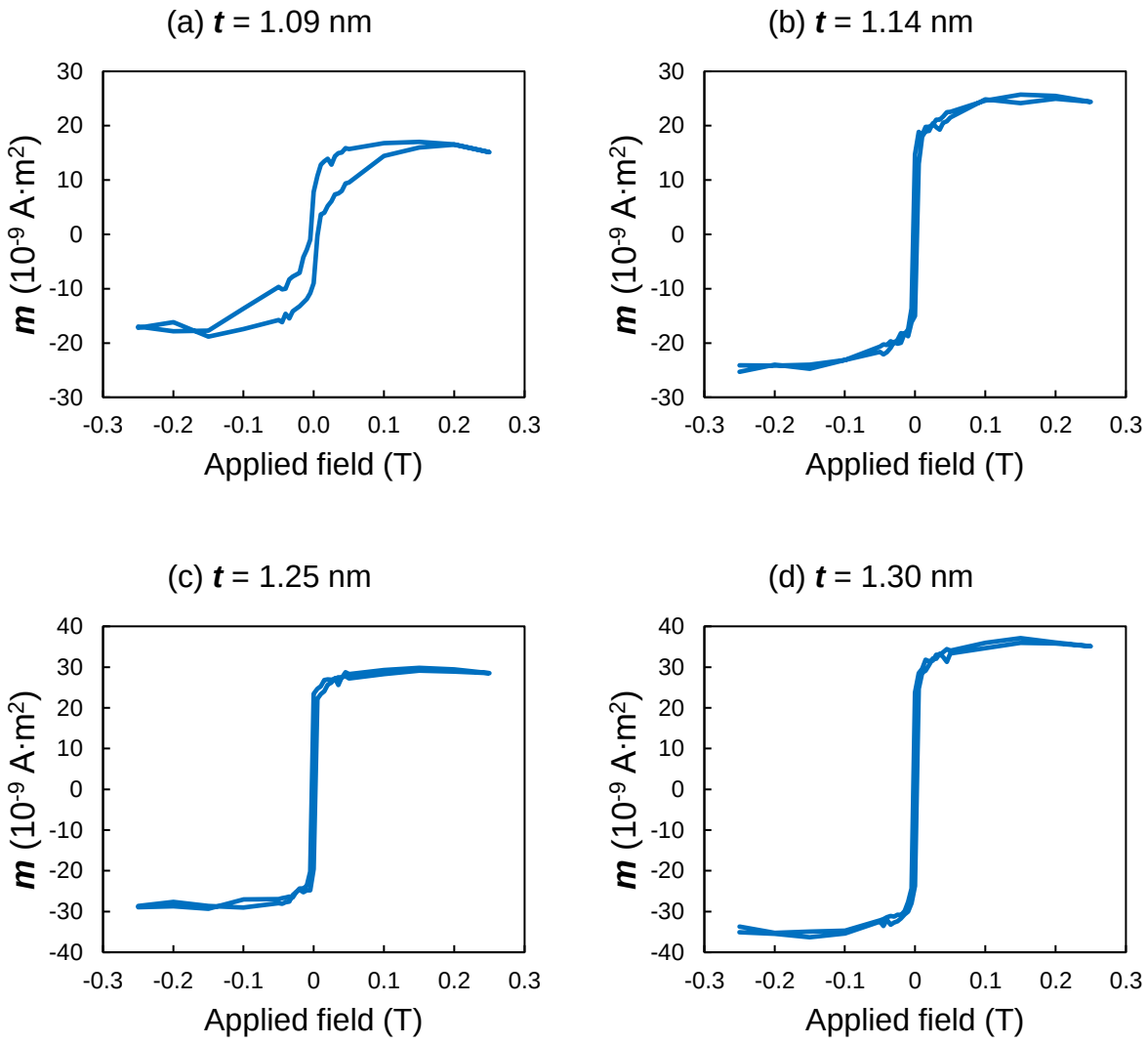

Fig. 5.4: Magnetic moment vs. applied field for samples annealed at 400 °C with CoFeB/CoFe thickness of (a) 1.09 nm, (b) 1.14 nm, (c) 1.25 nm, and (d) 1.30 nm.

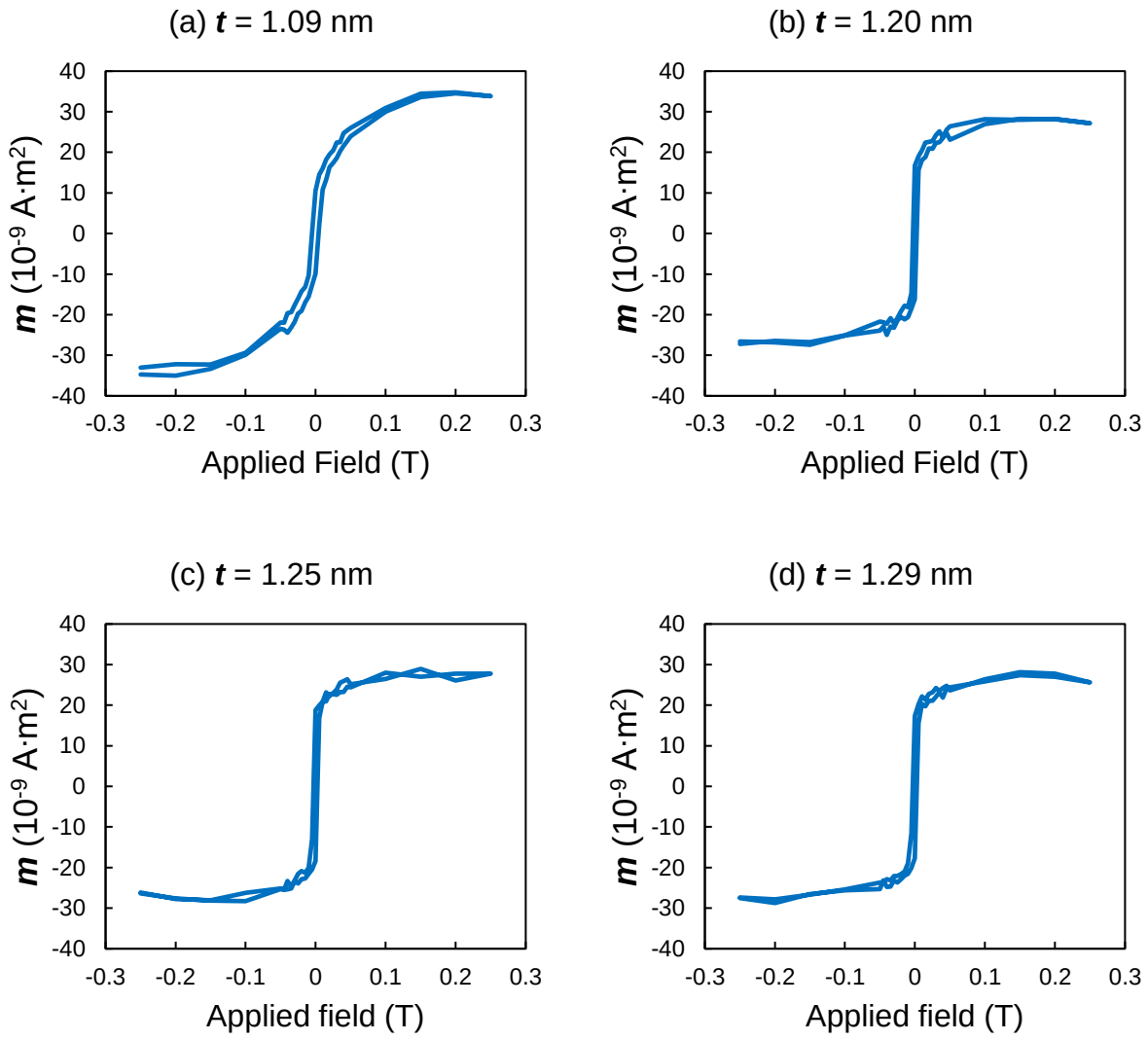

Fig. 5.5: Magnetic moment vs. applied field for samples annealed at 350 °C with CoFeB/CoFe thickness of (a) 1.09 nm, (b) 1.20 nm, (c) 1.25 nm, and (d) 1.29 nm.

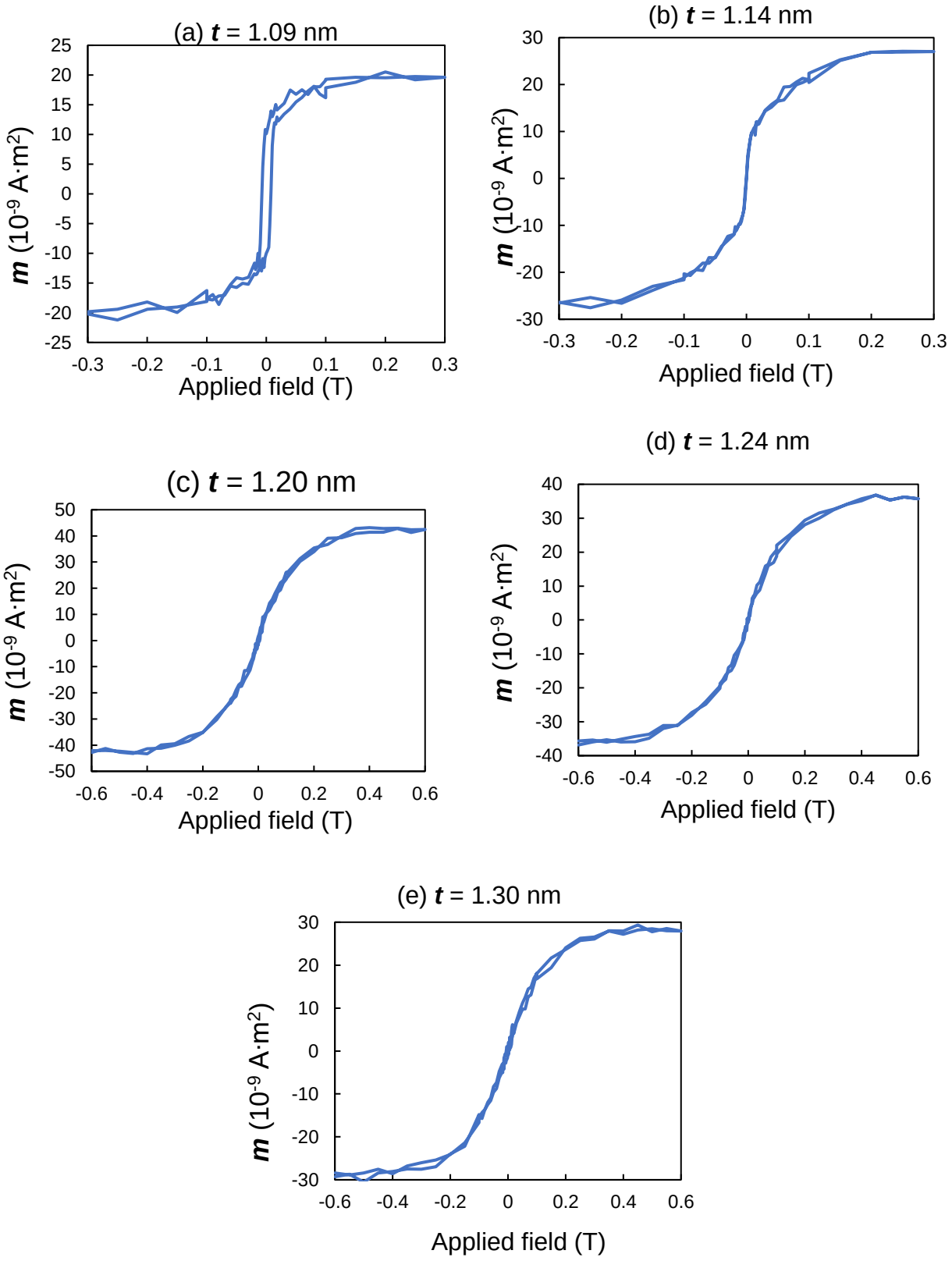

Fig. 5.6: Magnetic moment vs. applied field for samples annealed at 325 °C with CoFeB/CoFe thickness of (a) 1.09 nm, (b) 1.14 nm, (c) 1.20 nm, (d) 1.24 nm, and (e) 1.30 nm.

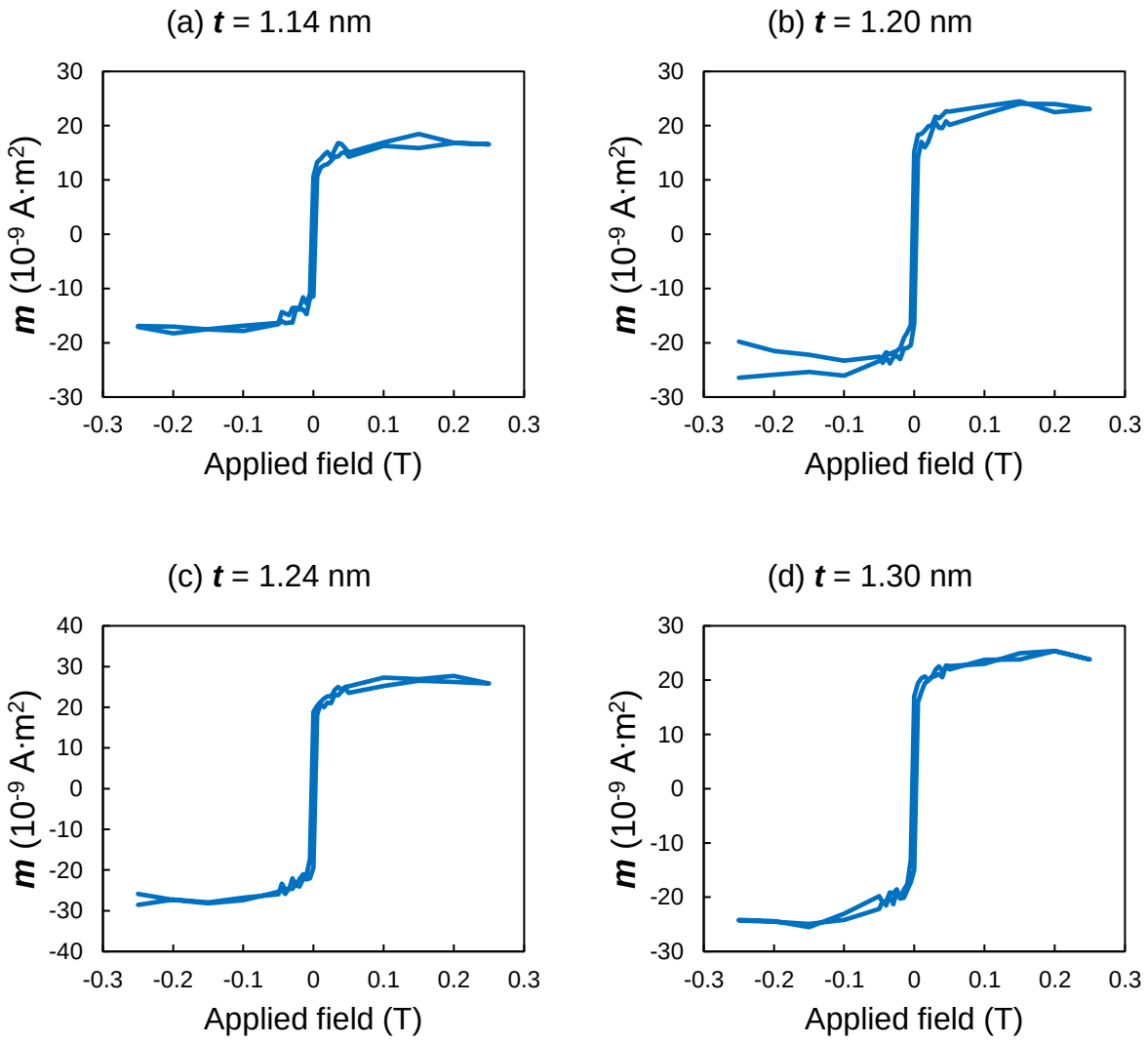

Fig. 5.7: Magnetic moment vs. applied field for samples annealed at 300 °C with CoFeB/CoFe thickness of (a) 1.14 nm, (b) 1.20 nm, (c) 1.24 nm, and (d) 1.30 nm.

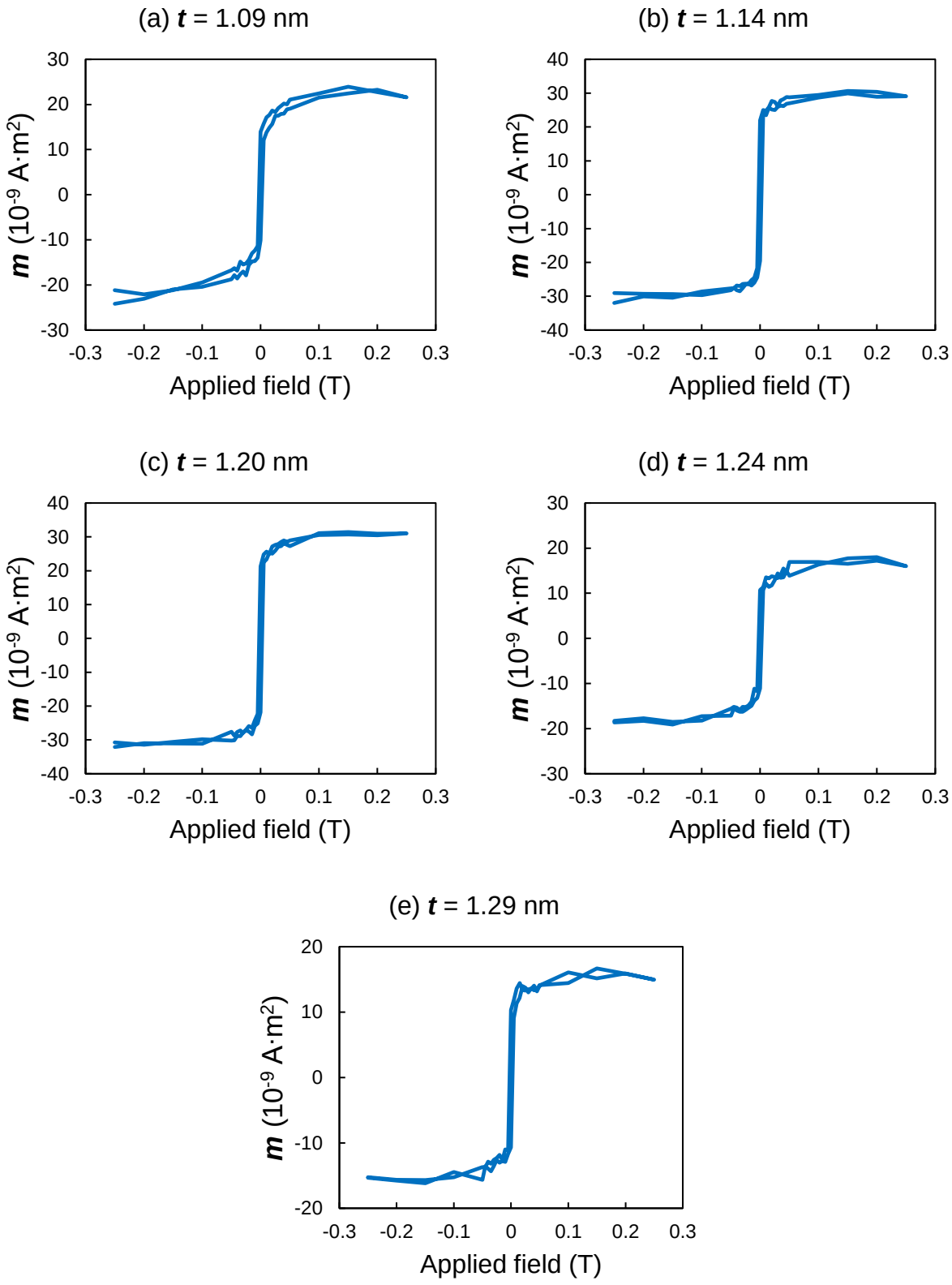

Fig. 5.8: Saturation moment vs. applied field for as-deposited samples with CoFeB/CoFe thickness of (a) 1.09 nm, (b) 1.14 nm, (c) 1.20 nm, (d) 1.24 nm, and (e) 1.29 nm.

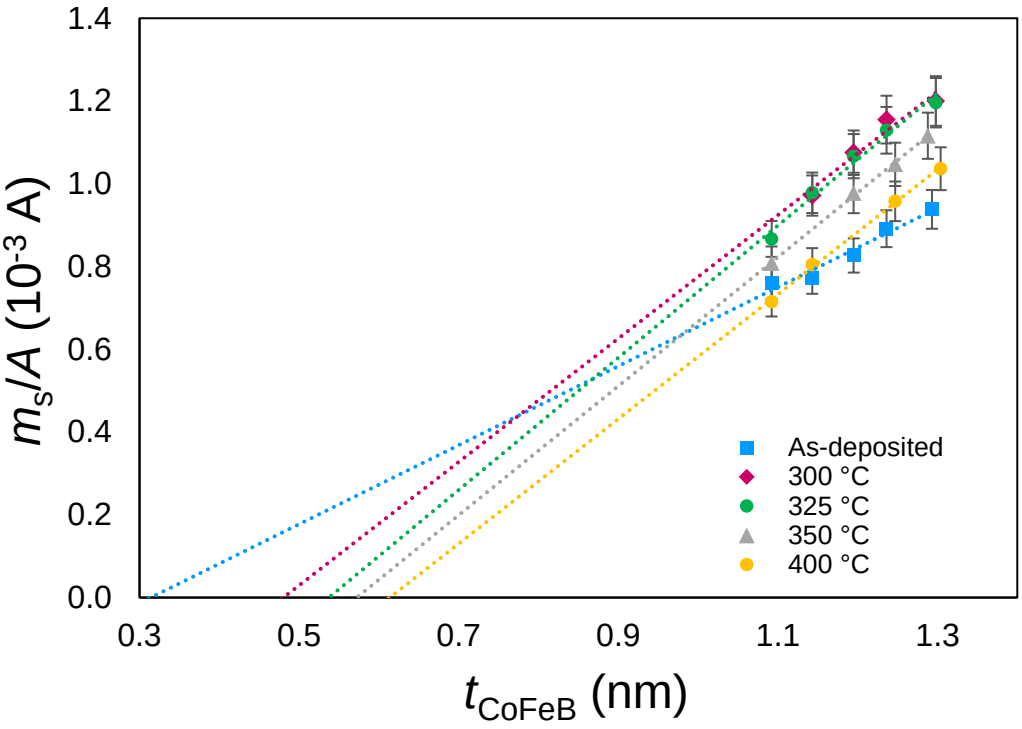

Fig. 5.9: Saturation moment per unit area. Dead layer thickness and saturation magnetization were extracted from the x-intercept and slope, respectively. Inset: magnetic moment for sample with combined CoFeB/CoFe thickness of 1.20 nm annealed at 350 °C.

For each of the sample series under various annealing conditions, a non-zero horizontal asymptote in the areal moment versus thickness curve indicates the presence of a magnetic dead layer, commonly seen in CoFeB/MgO thin films [5,10]. From the data in Fig. 5.9, we evaluated the dead layer thickness (the *x*-intercept) and the saturation magnetization (the slope) for each annealing series. A clear trend shows that the dead layer thickness increases with annealing, while the saturation magnetization only increases up to 325 °C, after which it appears to level off or slightly decrease. This trend has been seen in homogeneous CoFeB layers and is typically associated with the oxidation of the CoFe at the MgO interface and interdiffusion with the heavy metal underlayer (W in this case), and the densification of the CoFe layer during annealing, respectively [4,14,17].

Estimates for dead layer thickness, t_{DL}, and saturation magnetization, M_S, are summarized in Table 5.1. Uncertainty in the estimated parameters reflect uncertainties in the measured areal saturation magnetization, uncertainty in the nominal film thickness, and the variance of the parameter estimates from linear fitting of the areal magnetization versus nominal thickness data. The dead layer thickness increased from 0.48 nm to 0.62 nm for annealing temperatures from 300 °C to 400 °C – observations that agree with results from other groups [7,9,14]. Our results indicate a saturation magnetization of approximately 1500 kA/m was achieved by annealing at 300 °C, which is larger than previous results without a CoFe insertion layer for this annealing temperature [7,9,14].

Table 5.1 – Dead layer thickness (t_{DL}) and saturation magnetization (M_S) for CoFeB/CoFe/MgO heterostructures for several annealing conditions

	t_{DL} (nm)	M_S (kA/m)
As-deposited	0.32 ± 0.03	970 ± 30
300°C	0.48 ± 0.02	1500 ± 40
325°C	0.54 ± 0.02	1600 ± 30
350°C	0.57 ± 0.01	1570 ± 30
400°C	0.62 ± 0.01	1510 ± 30

Next, ferromagnetic resonance measurements were taken to estimate the perpendicular anisotropy field and Gilbert damping in the films. FMR is a measurement technique used to measure the magnetic properties of magnetic materials by probing and quantifying the precessional motion of magnetization. When the precessional frequency at an applied external field value is the same as the frequency applied, absorption strongly increases; this is a resonance and the applied field value is the resonance field. For each sample, a series of absorption versus applied field scans

were taken at several frequencies to sample the ferromagnetic resonance field versus frequency dispersion and the linewidth versus frequency dispersion; an example series is shown in Fig. 5.10.

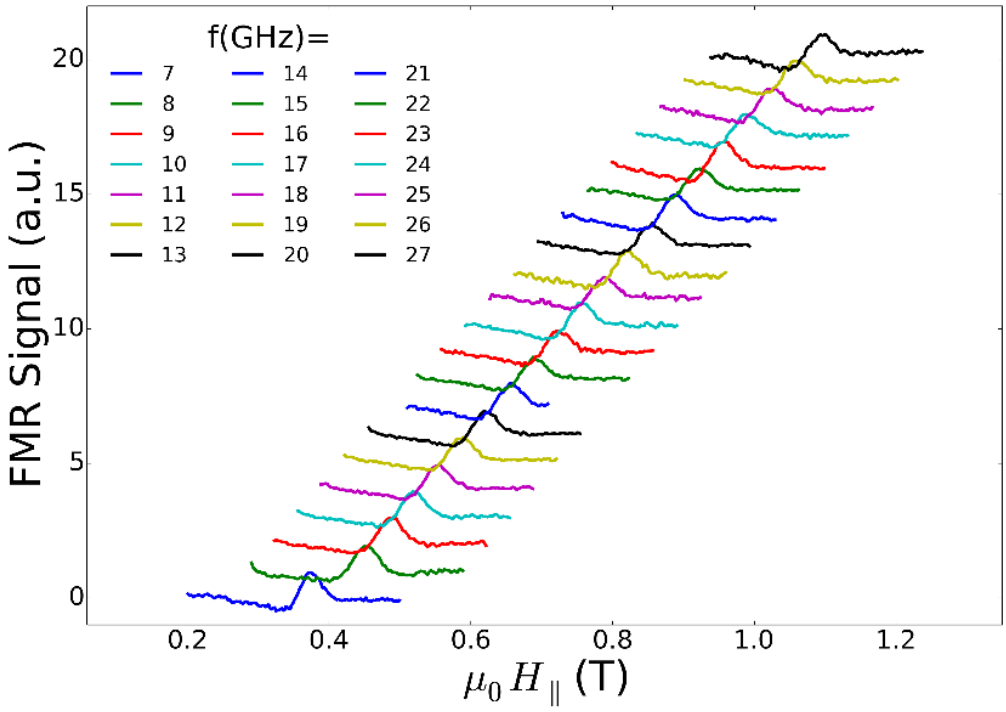

Fig. 5.10: A series of field-swept traces at numerous frequencies from 7 GHz (bottom left) to 27 GHz (top right) for the sample annealed at 350 °C with effective CoFe/CoFeB thickness of approximately 0.52 nm. Scans are offset vertically for clarity.

Several equations are used to fit the extracted data. The ferromagnetic resonance condition is given by the Kittel equation for planar applied fields [18]:

$$f^2 = \gamma^2 \mu_0^2 H \left(H + M_S - \frac{2K_1}{M_S} - \frac{4K_2}{M_S} \right) \tag{5.1}$$

where γ is the gyromagnetic ratio, M_s is the saturation magnetization, and K_1 and K_2 are the first and second order uniaxial anisotropy constants. The linewidth of the resonance is linear in frequency:

$$\mu_0 \Delta H = \frac{2\alpha f}{\gamma} + \mu_0 \Delta H_0 \tag{5.2}$$

where $\mu_0 H_0$ is the inhomogeneous linewidth broadening and α is the Gilbert damping coefficient. Exemplary data is presented in Fig. 5.11 for the sample with combined CoFeB and CoFe thickness t = 1.26 nm annealed at 350 °C, with best-fit curves overlaid on top of the data markers. The Kittel equation is used to fit the data and extract the effective magnetization, M_{eff}:

$$\mu_0 M_{\text{eff}} = \mu_0 M_S - 2K_1/M_S - 4K_2/M_S. \tag{5.3}$$

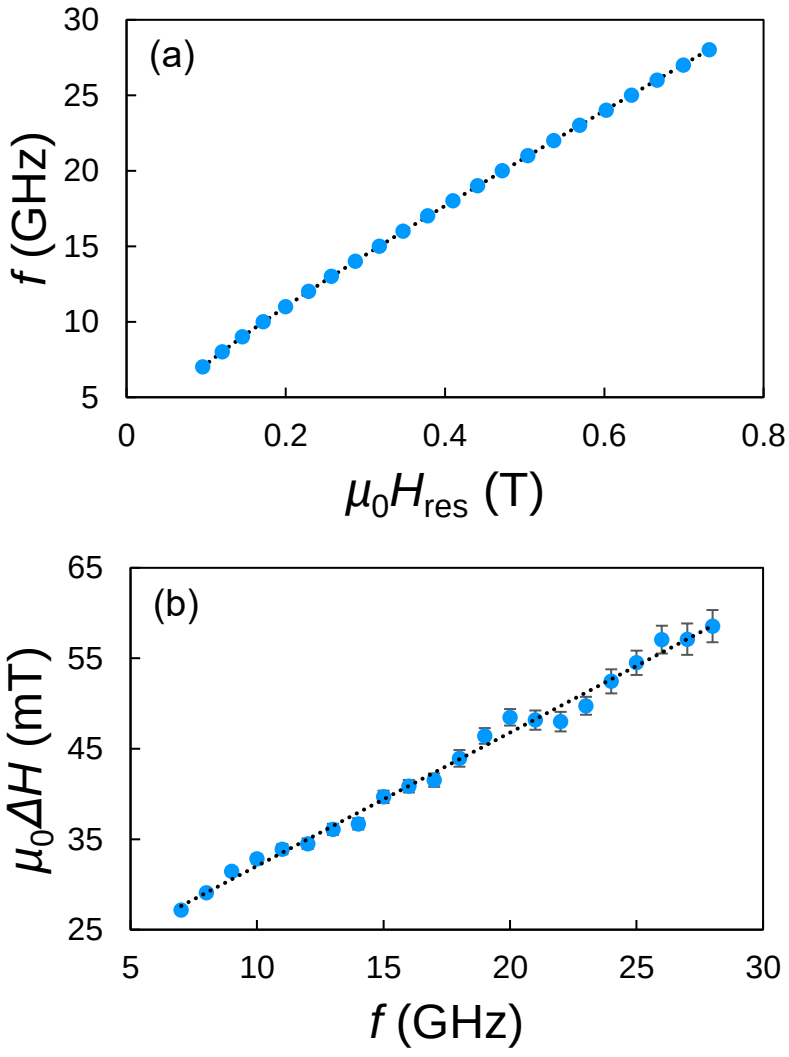

Fig. 5.11: (a) The ferromagnetic resonance field versus excitation frequency and (b) the linewidth versus excitation frequency of the sample with combined CoFeB and CoFe thickness t = 1.26 nm annealed at 350 °C.

The effective magnetization versus the effective thickness (defined as the combined CoFeB and CoFe thickness minus the dead layer thickness at each temperature) has been plotted in Fig. 5.12(a). Vertical error bars reflect the one-sigma uncertainty in the M_{eff} parameter estimated from the frequency versus resonance field dispersion, which implicitly carries the uncertainties of each estimated resonance field from Lorentzian fits to the absorption curve and ultimately, the precision of the applied external field. For the as-deposited sample, all discrete points along the CoFe thickness wedge revealed a positive effective magnetization, and correspondingly an easy-plane magnetization. As the annealing temperature is increased, the magnetic dead layer thickness similarly rises. However, the position of the thickness-dependent transition between an easy-plane and an out-of-plane magnetic easy axis takes place around a common effective thickness of approximately 0.63 nm. This is a strong indication that the appearance of perpendicularly magnetized regions of the nominally higher combined CoFeB and CoFe thicknesses at elevated annealing temperatures is strongly influenced by the corresponding increases in magnetic dead layer thickness with annealing temperature. A net perpendicular magnetic anisotropy was observed in several regions of the samples annealed at 325 °C, 350 °C, and 400 °C with CoFe insertion layer effective thicknesses ($t_{CoFeB} - t_{DL}$) below 0.7 nm. While a thickness dependence consistent with an interfacial anisotropy is observed for temperatures up to 350 °C, the M_{eff} versus thickness for the sample annealed at 400 °C is clearly non-monotonic. This appears to be a reliability issue associated with annealing stability in the heterogeneous CoFe/CoFeB samples at 400 °C.

By plotting the M_{eff} data versus the effective thickness instead of the nominal thickness, we can see that the annealing series nearly collapse onto a master curve. Here we can estimate that the zero-crossing (the spin reorientation transition into the plane) occurs in the vicinity of an effective thickness of 0.6 nm. In particular, the critical effective thickness is 0.62 nm for an

annealing temperature of 300 °C, 0.63 nm for an annealing temperature of 325 °C, 0.59 nm for an annealing temperature of 350 °C, and finally 0.60 nm for annealing at 400 °C. Interestingly, measurements of the effective magnetization in the two sample series annealed at 325 °C and 350 °C are qualitatively very similar, indicating a range of annealing temperature stability over which the magnetic anisotropy variation is minimal.

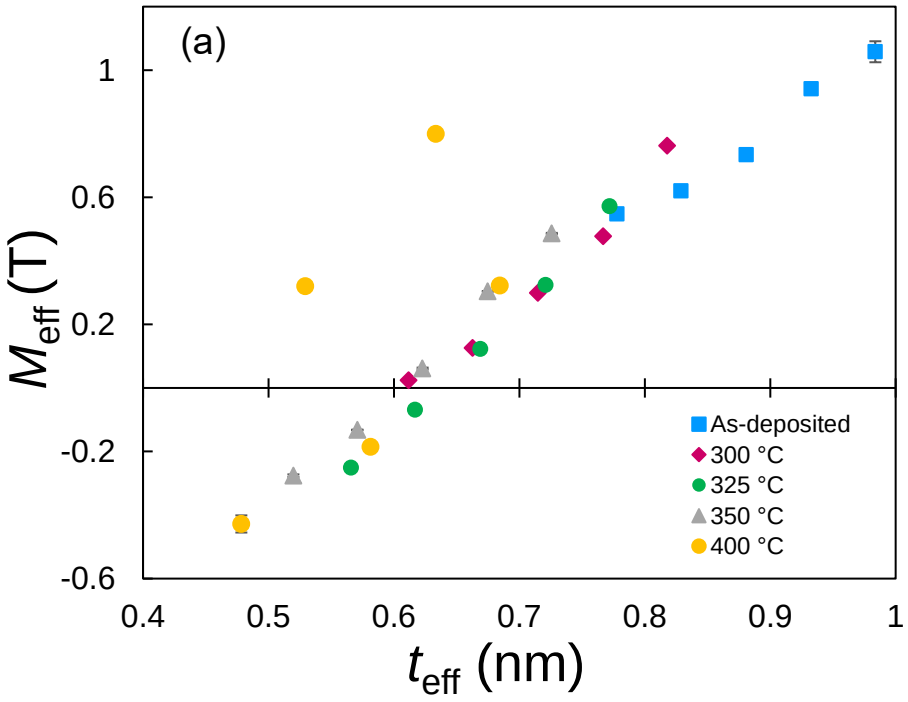

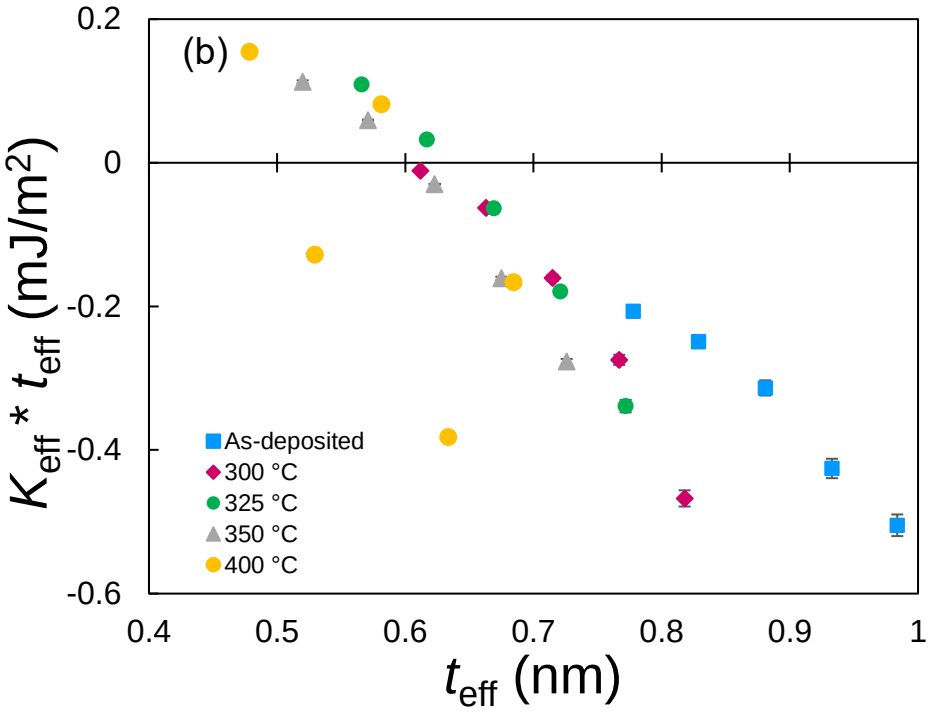

Fig. 5.12: (a) Effective demagnetization field vs. effective thickness (combined CoFeB/CoFe layer thickness minus dead layer thickness) for several annealing temperatures. (b) Effective magnetic anisotropy multiplied by effective thickness versus the effective thickness for several annealing temperatures.

The effective magnetic anisotropy multiplied by effective thickness versus the effective thickness has been plotted in Fig. 5.12(b). Effective magnetic anisotropy is given by:

$$K_{\text{eff}} = -\frac{1}{2} M_{\text{eff}} M_{\text{S}} \qquad (4)$$

When $K_{\text{eff}} * t_{\text{eff}}$ is greater than 0, the magnetization is out-of-plane, and when $K_{\text{eff}} * t_{\text{eff}}$ is less than zero, the magnetization is in-plane. We estimate K_{i} by a linear fit to the $K_{\text{eff}} * t_{\text{eff}}$ versus t_{eff} data shown in Fig. 5.12(b), for which the y-intercept value equals K_{i}. K_{i} values are 0.98, 1.36, 1.35, and 1.15 mJ/m^2 for the as-deposited, 300 °C, 325 °C, and 350 °C annealing temperatures, respectively.

The Gilbert damping (α) parameter versus effective thickness of the CoFeB/CoFe layer is shown in Fig. 5.13. Vertical error bars reflect the one-sigma uncertainty in the α parameter estimated from the linewidth versus frequency dispersion, which implicitly carries the

uncertainties of each estimated resonance linewidth from Lorentzian fits to the absorption curve and ultimately, the precision of the applied external field. The overall average magnitude of the Gilbert damping is comparable with similar CoFeB films grown without a CoFe dusting layer, and there is a moderate reduction in the damping following annealing [9]. Thinner CoFe insertion layer samples show a net reduction in the Gilbert damping upon annealing up to 350 °C, when compared to the as-deposited case. On the other hand, samples with a thicker CoFe insertion layer exhibit a weaker temperature trend, or do not indicate a significant change in the Gilbert damping under annealing. This suggests that the annealing treatment has a weaker effect on the samples with a thicker CoFe insertion, and perhaps serves as an indication of the significance of the relatively higher boron content in the annealing and crystallization of thinner layers and thereby on the damping behavior.

The effective demagnetization data and the Gilbert damping constant estimated from the 400 °C annealed thickness series has a clearly non-monotonic trend, in contrast to the other samples in this growth series. Possible reasons for this range from overoxidation through the thin (2 nm thick) Ta cap to thermodynamic instability of this particular heterostructure, leading to the deleterious effects of interdiffusion of the W/CoFeB/CoFe complex. This may suggest that for the particular sample series, the annealing stability is limited to below 400 °C.

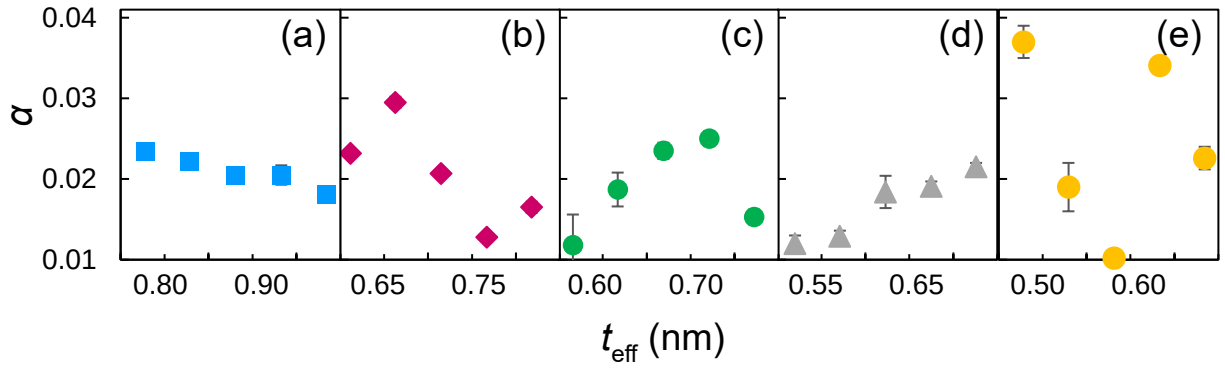

Fig. 5.13: Gilbert damping coefficient for annealing temperatures of (a) as-deposited, (b) 300 °C, (c) 325 °C, (d) 350 °C, and (e) 400 °C as a function of effective thickness of combined CoFeB/CoFe layer.

5.4 Conclusion

This study has demonstrated the feasibility of using a dusting layer of CoFe at the interface between CoFeB and MgO to achieve moderate perpendicular magnetic anisotropy, low damping, and relatively high saturation magnetization. We measured perpendicular magnetic anisotropy for several samples over a range of combined CoFeB/CoFe thicknesses and annealing temperatures, as shown in Fig. 5.14. For several annealed samples, we observed a net perpendicular magnetic anisotropy with a saturation magnetization exceeding 1500 kA/m and a Gilbert damping coefficient below 0.015.

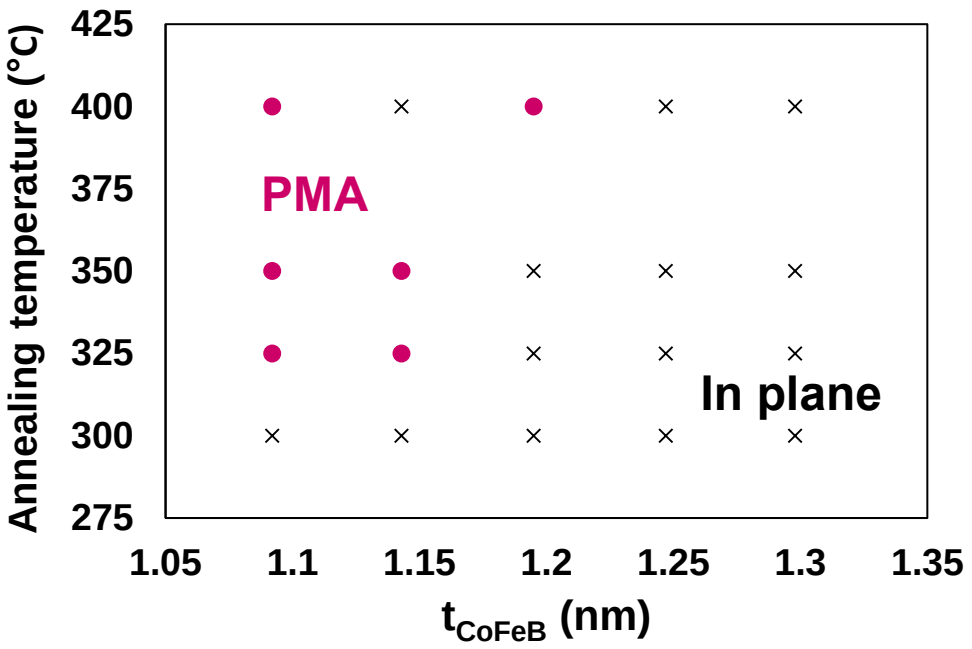

Fig. 5.14: The range of combined CoFeB/CoFe thicknesses and annealing temperatures which showed perpendicular magnetic anisotropy and those that showed in-plane magnetization.

Engineering desirable spintronic properties in the CoFeB/MgO system follows from depositing a Co-Fe-B alloy layer that is sufficiently amorphous and dense to form a smooth underlayer for the MgO growth, followed by crystallization during annealing under the influence of the MgO layer. Previous studies have looked at the effect of boron composition in Co-Fe-B layers on several paraments including microstructure, magnetic anisotropy, and annealing stability [19–21]. By inserting a CoFe layer between the CoFeB and MgO, we demonstrate an approach for introducing a thickness gradient in B content, which can modify the final properties of the annealed bilayer by changing the microstructure of the as-deposited film. Future studies may indicate that not only the proportion of CoFe to CoFeB, but the location of the inserted CoFe layer within the CoFeB film could have meaningful effects on the properties of annealed heterostructures.

Chapter 5 References

[1] Ikeda S, Miura K, Yamamoto H, Mizunuma K, Gan H D, Endo M, Kanai S, Hayakawa J, Matsukura F and Ohno H 2010 A perpendicular-anisotropy CoFeB-MgO magnetic tunnel junction *Nat. Mater.* **9** 721–4

[2] Kishi T, Yoda H, Kai T, Nagase T, Kitagawa E, Yoshikawa M, Nishiyama K, Daibou T, Nagamine M, Amano M, Takahashi S, Nakayama M, Shimomura N, Aikawa H, Ikegawa S, Yuasa S, Yakushiji K, Kubota H, Fukushima A, Oogane M, Miyazaki T and Ando K 2008 Lower-current and fast switching of A perpendicular TMR for high speed and high density spin-transfer-torque MRAM *Technical Digest - International Electron Devices Meeting, IEDM*

[3] Nishimura N, Hirai T, Koganei A, Ikeda T, Okano K, Sekiguchi Y and Osada Y 2002 Magnetic tunnel junction device with perpendicular magnetization films for high-density magnetic random access memory *J. Appl. Phys.* **91** 5246–9

[4] Wang Y-H, Chen W-C, Yang S-Y, Shen K-H, Park C, Kao M-J and Tsai M-J 2006 Interfacial and annealing effects on magnetic properties of CoFeB thin films *J. Appl. Phys.* **99** 08M307

[5] Jang S Y, Lim S H and Lee S R 2010 Magnetic dead layer in amorphous CoFeB layers with various top and bottom structures *J. Appl. Phys.* **107** 09C707

[6] Torrejon J, Kim J, Sinha J, Mitani S, Hayashi M, Yamanouchi M and Ohno H 2014 Interface control of the magnetic chirality in CoFeB/MgO heterostructures with heavy-metal underlayers *Nat. Commun.* **5** 4655

[7] An G-G, Lee J-B, Yang S-M, Kim J-H, Chung W-S and Hong J-P 2015 Highly stable perpendicular magnetic anisotropies of CoFeB/MgO frames employing W buffer and capping layers *Acta Mater.* **87** 259–65

[8] Lee K-M, Choi J W, Sok J and Min B-C 2017 Temperature dependence of the interfacial magnetic anisotropy in W/CoFeB/MgO *AIP Adv.* **7** 065107

[9] Lattery D M, Zhang D, Zhu J, Hang X, Wang J-P and Wang X 2018 Low Gilbert Damping Constant in Perpendicularly Magnetized W/CoFeB/MgO Films with High

Thermal Stability *Sci. Rep.* **8** 13395

[10] Watanabe K, Fukami S, Sato H, Ikeda S, Matsukura F and Ohno H 2017 Annealing temperature dependence of magnetic properties of CoFeB/MgO stacks on different buffer layers *Jpn. J. Appl. Phys.* **56** 0802B2

[11] Cheng C W, Feng W, Chern G, Lee C M and Wu T H 2011 Effect of cap layer thickness on the perpendicular magnetic anisotropy in top MgO/CoFeB/Ta structures *J. Appl. Phys.* **110** 033916

[12] Kim D, Jung K Y, Joo S, Jang Y, Hong J, Lee B C, You C Y, Cho J H, Kim M Y and Rhie K 2015 Perpendicular magnetization of CoFeB on top of an amorphous buffer layer *J. Magn. Magn. Mater.* **374** 350–3

[13] Ikeda S, Hayakawa J, Ashizawa Y, Lee Y M, Miura K, Hasegawa H, Tsunoda M, Matsukura F and Ohno H 2008 Tunnel magnetoresistance of 604% at 300 K by suppression of Ta diffusion in CoFeBMgOCoFeB pseudo-spin-valves annealed at high temperature *Appl. Phys. Lett.* **93** 082508

[14] Jang S Y, You C Y, Lim S H and Lee S R 2011 Annealing effects on the magnetic dead layer and saturation magnetization in unit structures relevant to a synthetic ferrimagnetic free structure *J. Appl. Phys.* **109** 013901

[15] Skowroński W, Nozaki T, Lam D D, Shiota Y, Yakushiji K, Kubota H, Fukushima A, Yuasa S and Suzuki Y 2015 Underlayer material influence on electric-field controlled perpendicular magnetic anisotropy in CoFeB/MgO magnetic tunnel junctions *Phys. Rev. B* **91** 184410

[16] Gopman D B, Sampath V, Ahmad H, Bandyopadhyay S and Atulasimha J 2017 Static and Dynamic Magnetic Properties of Sputtered Fe-Ga Thin Films *IEEE Trans. Magn.* **53** 6101304

[17] Oguz K, Jivrajka P, Venkatesan M, Feng G and Coey J M D 2008 Magnetic dead layers in sputtered Co40 Fe40 B20 films *J. Appl. Phys.* **103** 07B526

[18] Kittel C 1948 On the Theory of Ferromagnetic Resonance Absorption *Phys. Rev.* **73** 155–61

[19] Kodzuka M, Ohkubo T, Hono K, Ikeda S, Gan H D and Ohno H 2012 Effects of boron composition on tunneling magnetoresistance ratio and microstructure of CoFeB/MgO/CoFeB pseudo-spin-valve magnetic tunnel junctions *J. Appl. Phys.* **111** 043913

[20] Ikeda S, Koizumi R, Sato H, Yamanouchi M, Miura K, Mizunuma K, Gan H, Matsukura F and Ohno H 2012 Boron composition dependence of magnetic anisotropy and tunnel magnetoresistance in MgO/CoFe(B) based stack structures *IEEE Trans. Magn.* **48** 3829–32

[21] Honjo H, Ikeda S, Sato H, Sato S, Watanabe T, Miura S, Nasuno T, Noguchi Y, Yasuhira M, Tanigawa T, Koike H, Muraguchi M, Niwa M, Ito K, Ohno H and Endoh T 2016 Improvement of Thermal Tolerance of CoFeB-MgO Perpendicular-Anisotropy Magnetic Tunnel Junctions by Controlling Boron Composition *IEEE Trans. Magn.* **52** 3401104

Chapter 6: Extreme sub-wavelength electromagnetic antenna implemented with acoustically driven magnetostrictive nanomagnets

In this chapter, I report the demonstration of an extreme sub-wavelength electromagnetic antenna implemented with an array of magnetostrictive nanomagnets elastically coupled to an underlying piezoelectric substrate. A surface acoustic wave (SAW) launched into the substrate with contact pads periodically strains the nanomagnets and makes their magnetizations rotate and oscillate periodically in time, which results in the emission of electromagnetic waves at the frequency of the SAW. Thus, the nanomagnets acts like an electromagnetic antenna that is actuated by the SAW. Because the antenna is driven at the acoustic resonance instead of the electromagnetic resonance, and because at the same frequency, the wavelength of the SAW is five orders of magnitude smaller than the wavelength of electromagnetic wave, the antenna can radiate with reasonable efficiency even though the antenna dimension is several orders of magnitude smaller than the electromagnetic wavelength. The antenna lateral dimension is roughly four orders of magnitude smaller than the electromagnetic wavelength, but one order of magnitude larger than the acoustic wavelength, which allows the antenna to radiate with reasonable efficiency, because the relevant wavelength is the acoustic wavelength owing to the driving mechanism employed. A schematic of this device is shown in Fig. 6.1.

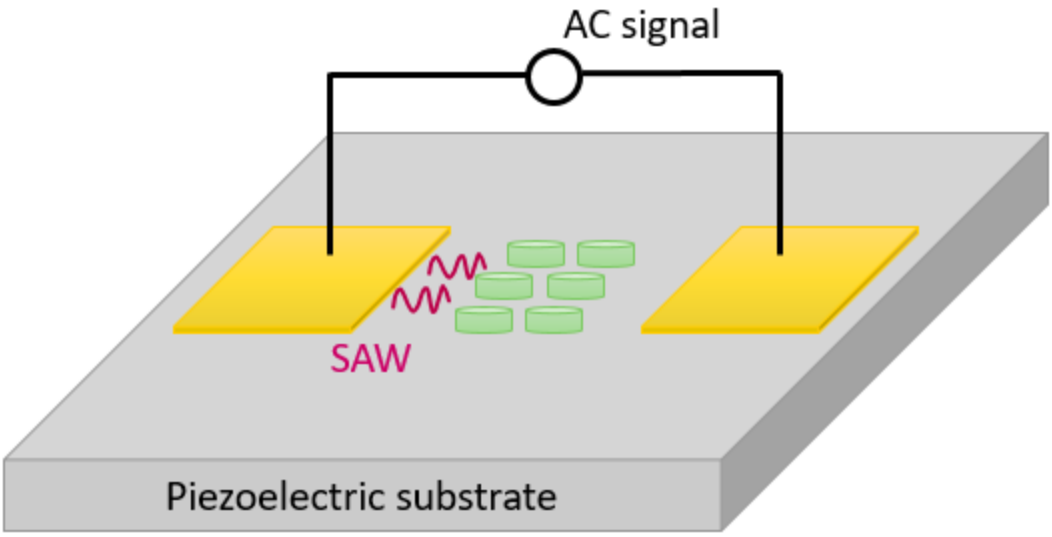

Fig. 6.1: A schematic of an extreme sub-wavelength electromagnetic antenna implemented with an array of magnetostrictive nanomagnets (not to scale) coupled to a piezoelectric substrate.

6.1 Introduction

Electromagnetic waves can be generated either by a periodically time varying electric field or a time varying magnetic field. Therefore, periodic magnetization flipping of nanomagnets will emit electromagnetic waves. Normally, antennas are excited by a periodic electromagnetic wave. The radiation efficiency of such an antenna is $\sim(l/\lambda)^2$, when $l < \lambda$, where l is the wavelength of the exciting electromagnetic wave. This makes it very difficult to miniaturize antennas that radiate at RF frequencies. For example, if the frequency is 100 MHz, then the electromagnetic wavelength is 3 meters. If the antenna dimension is only fractions of a mm, say, 300 μm, then the radiation efficiency would be $\sim(l/\lambda)^2$ which is on the order of 10^{-8}. Clearly, this would be insufficient. Here, however, we have excited the antenna with acoustic waves, and the wavelength of acoustic waves in many piezoelectric materials at 100 MHz is ~30 μm (the speed of acoustic waves is about 3000 m/s, whereas the speed of electromagnetic waves is about 3×10^8 m/s). The antenna dimension is now larger than the acoustic wavelength and hence the radiation efficiency will be much larger.

This is the principle of extreme sub-(electromagnetic) wavelength antenna which have been proposed [1-5].

The nanomagnet antenna has another advantage. Electromagnetically driven antennas are plagued by the so-called “platform effect”. The driving electromagnetic field of a traditional antenna produces image charges on a ground plane which tend to cancel the effect of the driving excitation, effectively reducing the radiation efficiency by offsetting the radiation of the antenna. Antennas predicated on the acoustic excitation of magnetostrictive nanomagnets will be largely immune to this effect [2].

6.2 Experimental Details

Cobalt nanomagnet arrays were fabricated on a piezoelectric lithium niobate ($LiNbO_3$) substrate to create the antenna. Four samples were prepared for fabrication: two with nanomagnet arrays and two without for ‘control’ samples. The device schematic is shown in Fig. 6.2:

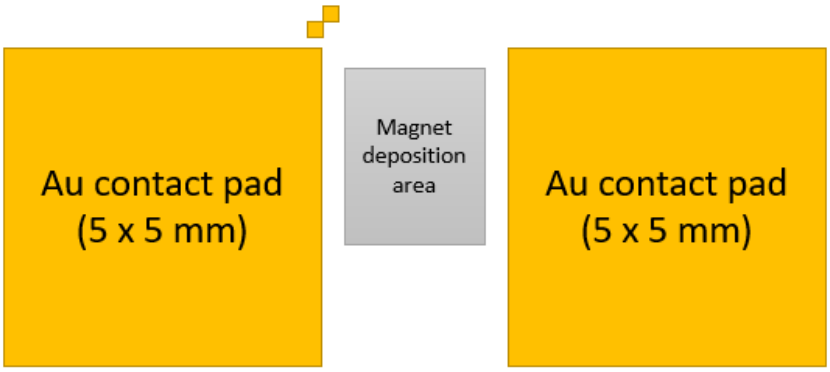

Fig. 6.2: Device fabrication schematic showing contact pads and alignment markers (yellow) and the area where magnets were deposited (grey)

Fabrication of the nanomagnet antenna device involved a two-step lithography process. During the first step, photolithography was used to delineate gold contact pads for external connection. First, the samples are cleaned by sonicating in acetone for 5 min, IPA for 5 min,

acetone again for 3 min, and finally methanol for 3 min. SPR 3012 is spin coated on each sample for 30 s at 4000 RPM before baking at 90 C for 1 min. To aid in the liftoff process, the wafer is soaked in toluene for 1 min, followed by an additional bake at 90 C for 15 s. The toluene-soaked surface layer develops slower than the layer underneath, to produce an overhang to reduce sidewall deposition. Next, the sample is exposed with 365 nm wavelength light to delineate the pattern, before developing and post-baking for 1 min at 120 C. Electron beam evaporation is used to deposit a thin layer of Ti (10 nm) for adhesion, followed by a 100 nm thick layer of Au, with a growth rate of 1 Å/s. Acetone is used to liftoff the resist and metal outside the pattern area. This process is illustrated in Fig. 6.3.

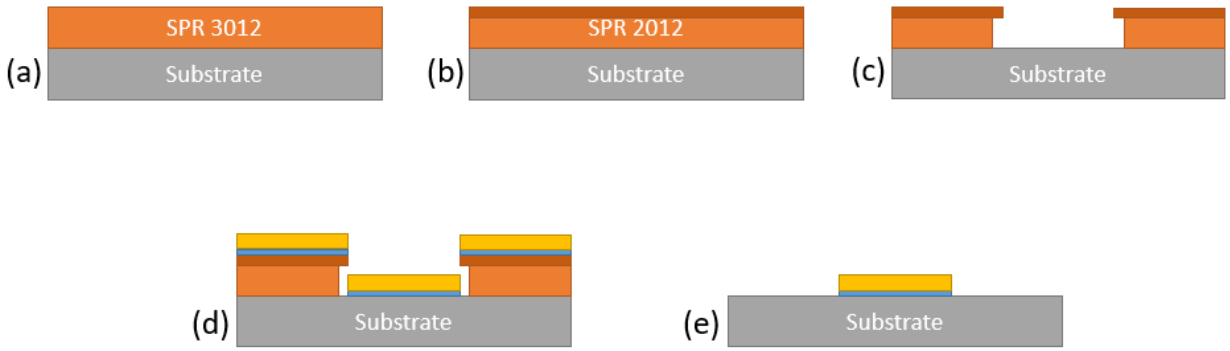

Fig. 6.3: The photolithography fabrication process: (a) spin coat sample with SPR 3012, (b) soak in toluene, (c) photolithography and develop, (d) evaporate Ti and Au, (e) liftoff.

An electron beam lithography (EBL) process is subsequently used to form the nanomagnet arrays. The samples are coated with a double layer resist. First, PMMA 495 A2 is spin coated for 5 s at 500 RPM, followed by 55 s at 2500 RPM, to give a thickness of ~50 nm. Then, PMMA 950 A2 is spin coated using the same program, to give a thickness of ~75 nm. Each layer is baked on a hot plate for 2 min at 115 C. The pattern is exposed with EBL at 30 kV, with a beam current of 60 µA, and a line dose of 1.1 nC/cm. The nanomagnet array pattern was delineated 31 times on Sample A and 75 times on Sample B. The samples were developed in a cold solution of 1:3 MIBK

to IPA for 10 s, then rinsed with IPA. Next, e-beam evaporation is used to deposit a thin layer of Ti for adhesion with a growth rate of 0.7 Å/s. This deposition was immediately followed by a layer of Co with a growth rate of 1.0 Å/s. The final thicknesses of the Ti and Co layers were ~5 nm and 20 nm, respectively. The final step was to soak the samples in Remover PG at 60 °C for 1 hr, followed by 20 s of sonication, or until all the metal around the pattern lifted off. This process is shown in Fig. 6.4.

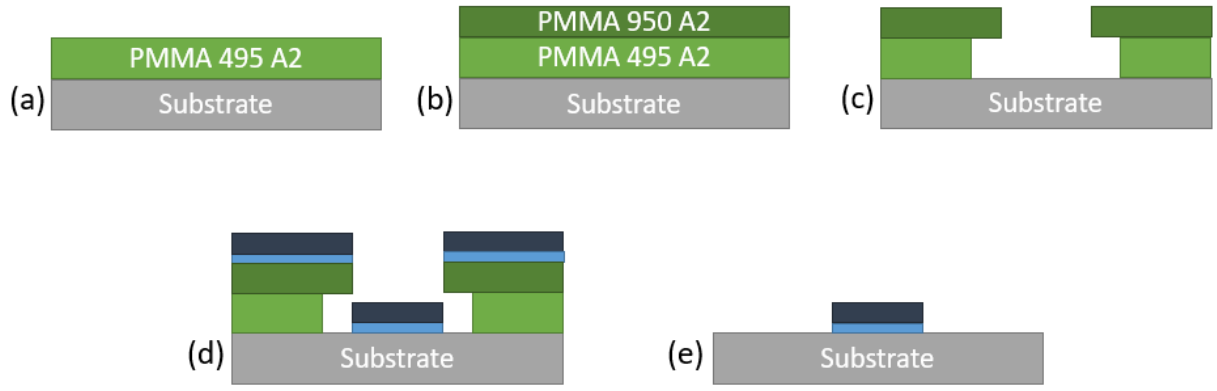

Fig. 6.4: The EBL fabrication process: (a) spin coat sample with PMMA 495, (b) spin coat with PMMA 950, (c) EBL and develop, (d) evaporate Ti and Co, (e) liftoff.

The samples were imaged using SEM to determine the success of the fabrication process. Some of the arrays on both samples A and B were over developed and the liftoff process failed to completely remove the excess material; this is seen in Fig. 6.5. The brighter arrays on the right side of each sample show failed liftoff. Each array was 80 x 90 nanomagnets. In total, there were 10/31 successful arrays on Sample A, about 72,000 nanomagnets, and 33/75 on Sample B, about 237,600 nanomagnets. Magnified images of successful arrays are shown in Fig. 6.6-6.8.

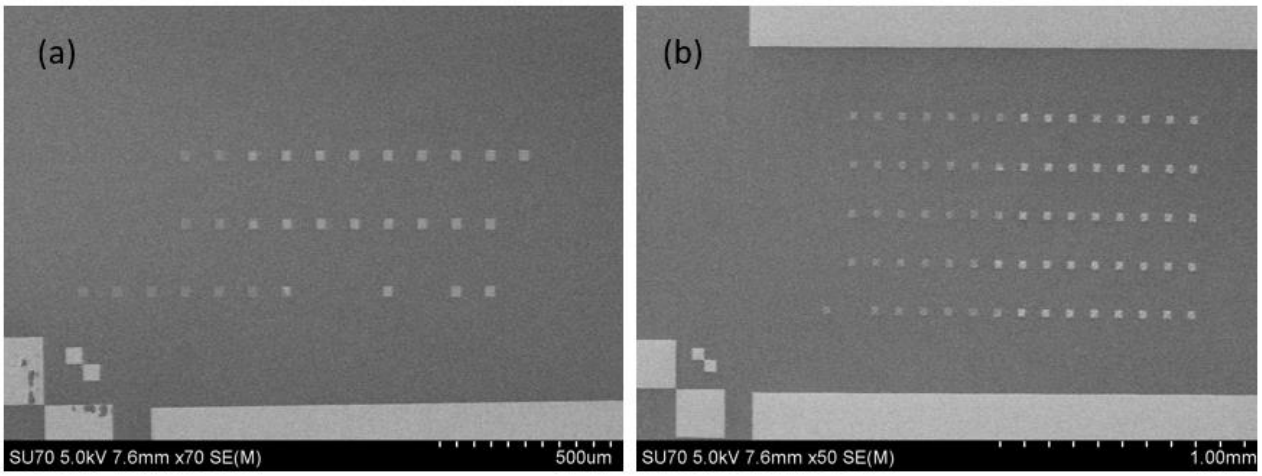

Fig. 6.5: Low magnification images of nanomagnet arrays of (a) Sample A and (b) Sample B

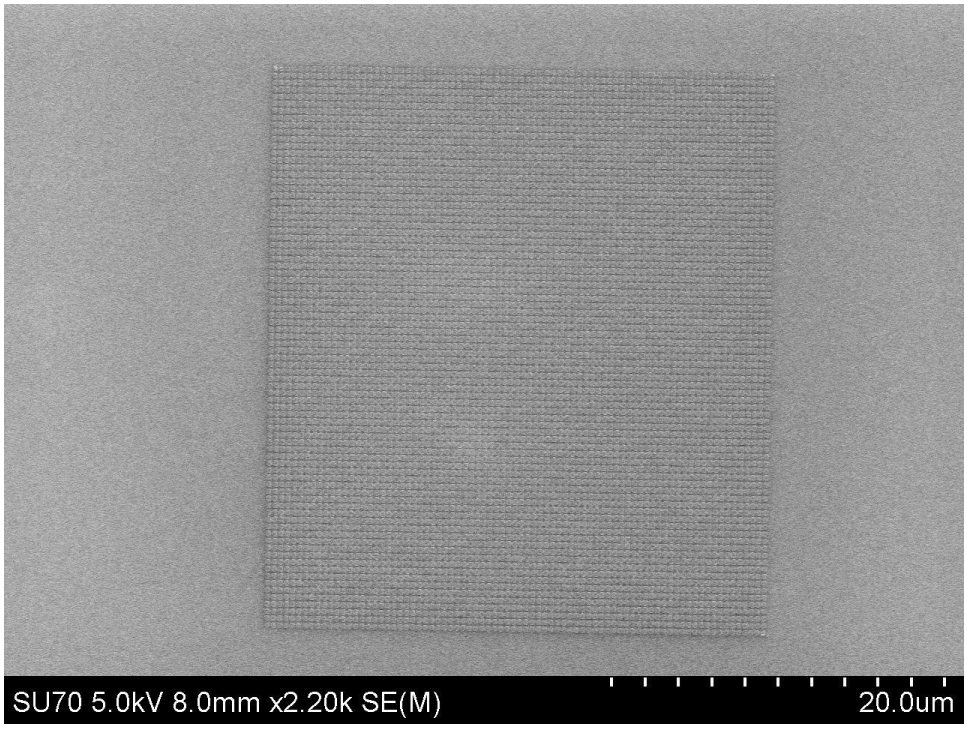

Fig. 6.6: An SEM image of Sample A, showing single nanomagnet array 80 nanomagnets across and 90 nanomagnets down

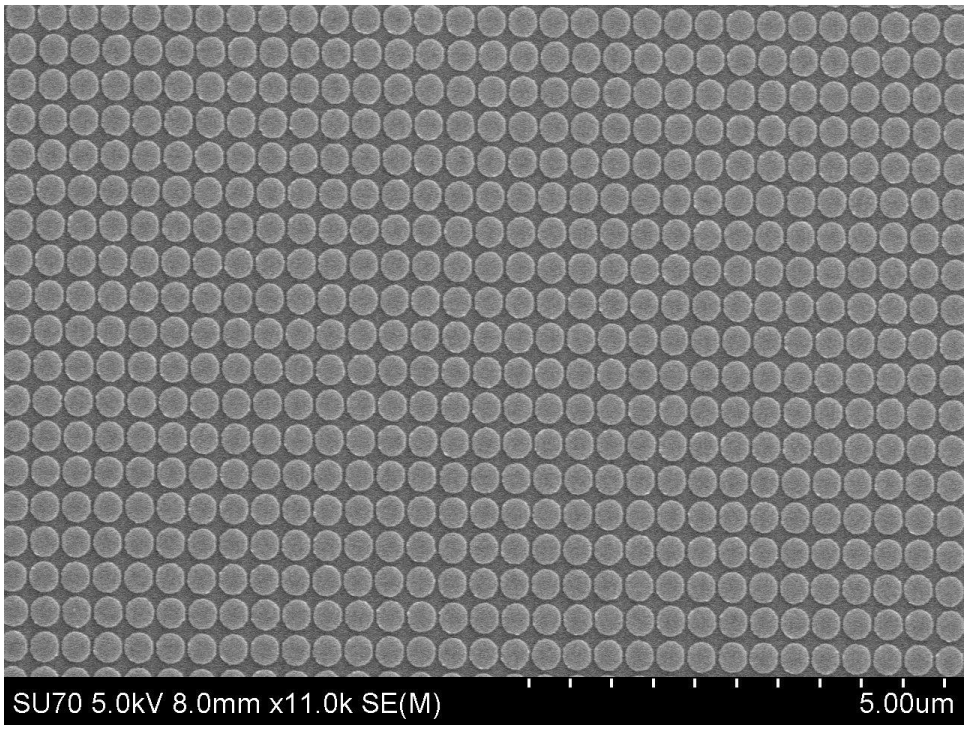

Fig. 6.7: An SEM image showing nanomagnets on Sample A

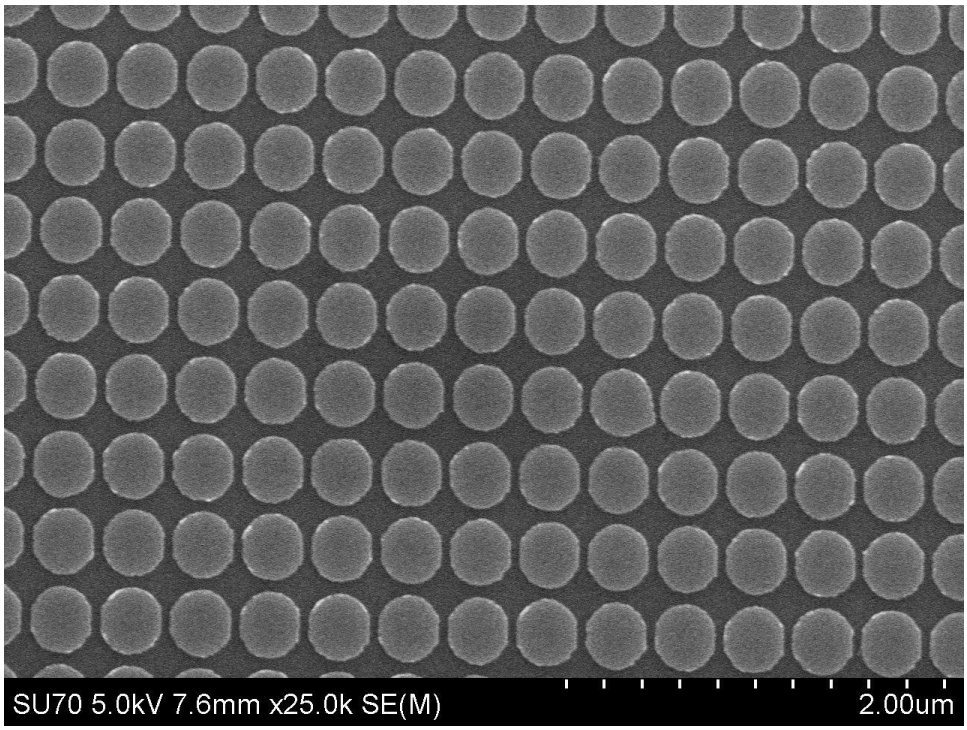

Fig. 6.8: An SEM image showing nanomagnets on Sample B

The nanomagnets were designed to be 330 nm along the major axis and 300 nm along the minor axis, with spacing of 75 nm along the major axis and 60 nm along the minor axis. The fabricated nanomagnets were about 10% larger than expected, with decreased array spacing: about 365 nm along the major axis and 330 nm along the minor axis, with spacing of about 65 nm along the major axis and 40 nm along the minor axis. These measurements are shown in Fig. 6.9.

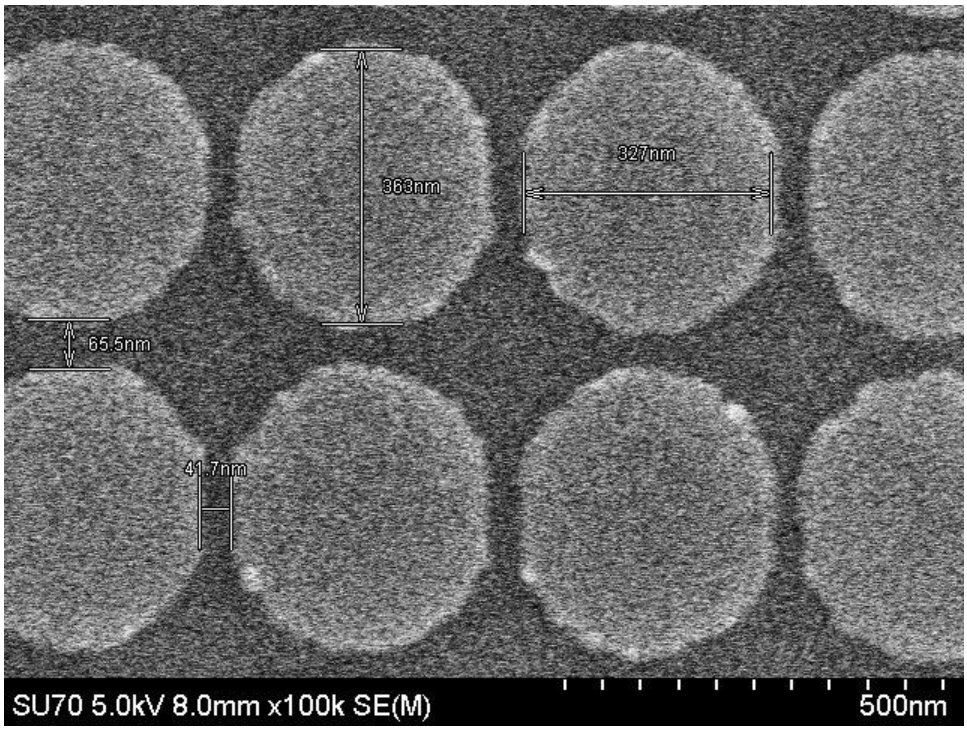

Fig. 6.9: An SEM image (Sample A) showing the measured magnet dimensions

6.3 Results and Discussion

After mounting an adapter for a coaxial cable across the contact pads using silver paste and epoxy, the antenna was connected to a signal generator. Using 5 dBm of power, measurements were taken at 900 MHz and 144 MHz. A spectrum analyzer was placed in the far field (approximately 4 m away from the sample) and connected to a patch antenna for the 900 MHz measurements and a dipole antenna for the 144 MHz measurements. The set-up is depicted in Fig. 10. The results for 900 MHz are shown in Fig. 6.11. There was no significant difference between

the peak signal for Control 1 and Sample A, -72.65 dBm and -71.55 dBm, respectively. This is likely due to the inability of the magnetization to oscillate at this high of a frequency.

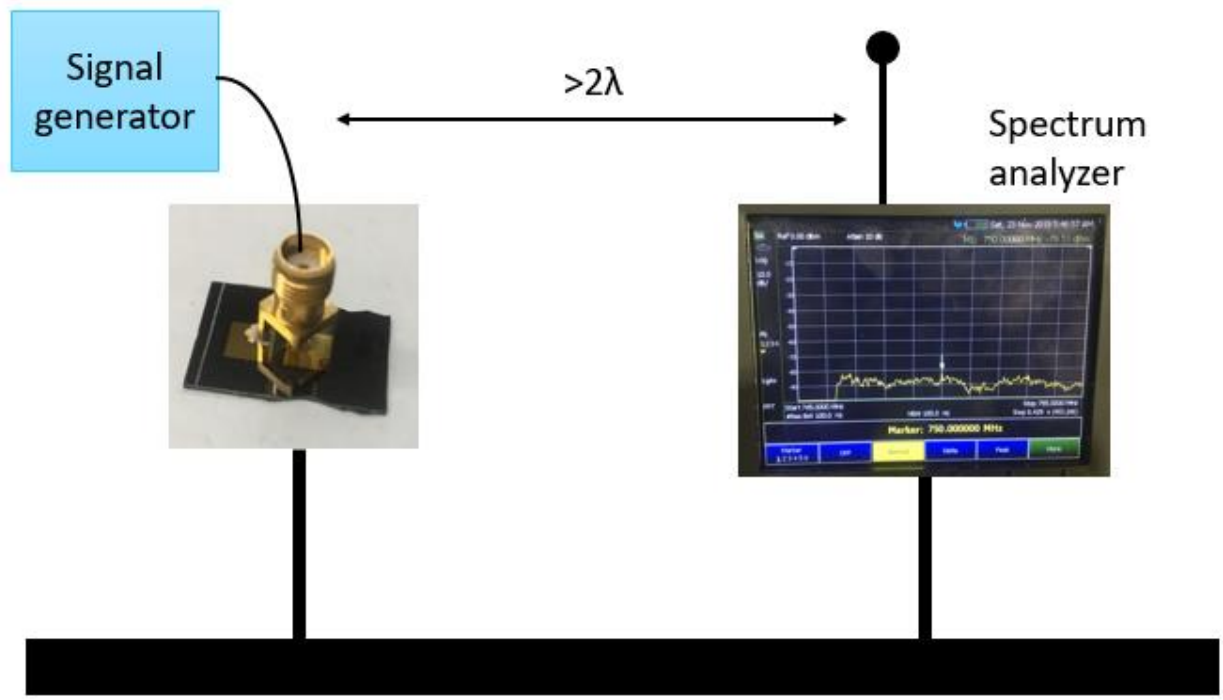

Fig. 6.10: Experimental set-up of antenna measurement showing the antenna connected to a signal generator by a coaxial adapter and cable and the spectrum analyzer connected to a dipole antenna in the far-field.

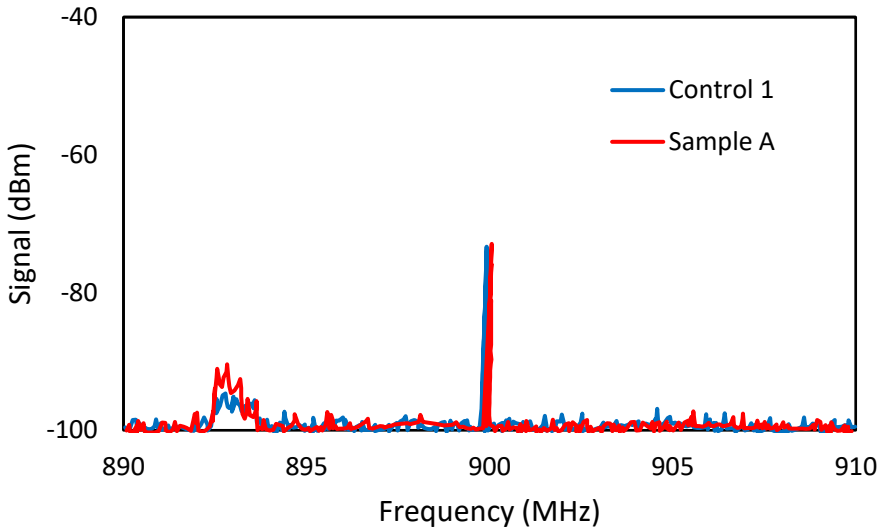

Fig. 6.11: Spectrum analyzer measurement at 900 MHz for samples Control 1 and Sample A

The results for 144 MHz are shown in Fig. 6.12. Here we could detect a difference between the real samples (with nanomagnets) and the control samples (without nanomagnets) because this frequency is low enough that the magnetizations can oscillate. The peak signals for Sample A and Sample B were -77.68 dBm and -73.38 dBm, respectively. Both signals were stronger than Control 1 and Control 2, which were -81.51 dBm and -82.69 dBm, respectively. The results are summarized in Table 6.1. The S11 parameter was also measured for Sample A and the controls, as shown in Fig. 6.13. Although the majority of the signal was measured as reflecting back, there is a small additional resonance around 1.3 GHz from Sample A that is not measured from the control samples.

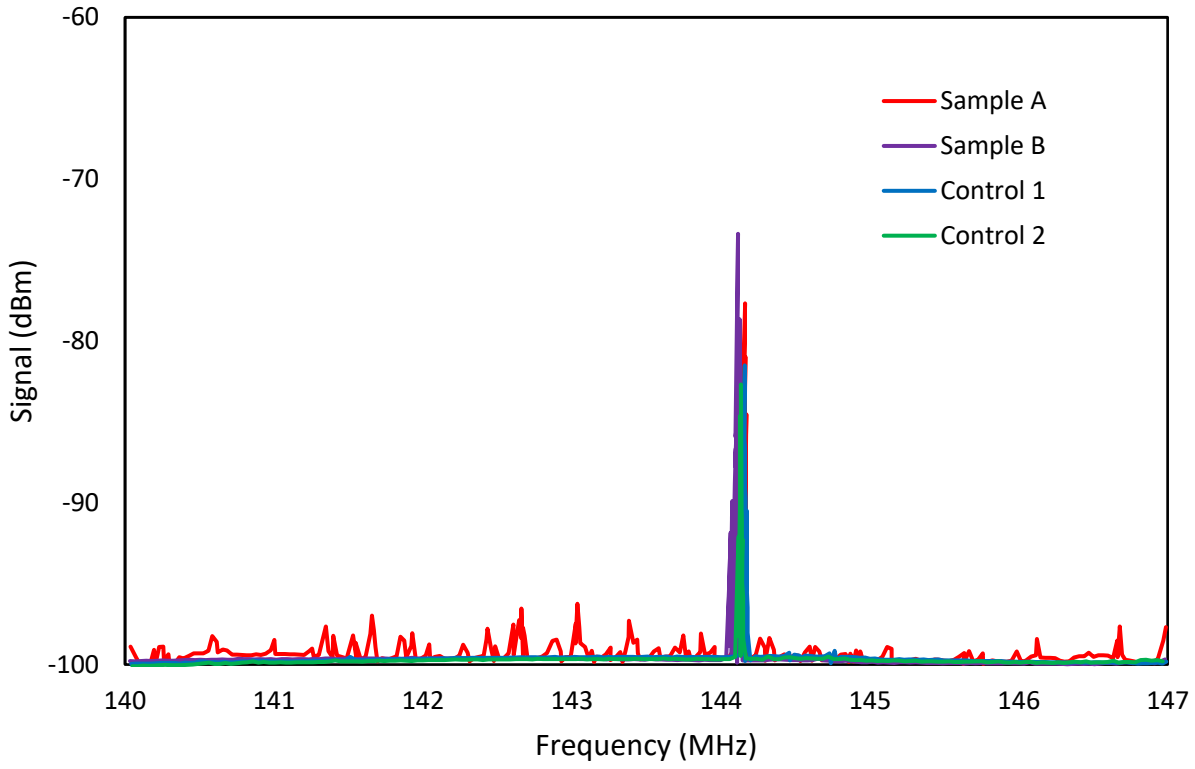

Fig. 6.12: Spectrum analyzer measurement at 144 MHz for samples Control 1, Control 2, Sample A, and Sample B

Table 6.1 – Peak signal strength (dBm) for sample and control measurements at 144 MHz and 900 MHz

	Peak signal at 144 MHz (dBm)	Peak signal at 900 MHz (dBm)
Sample A	-77.68	-71.55
Sample B	-73.38	
Control 1	-81.51	-72.65
Control 2	-82.69	

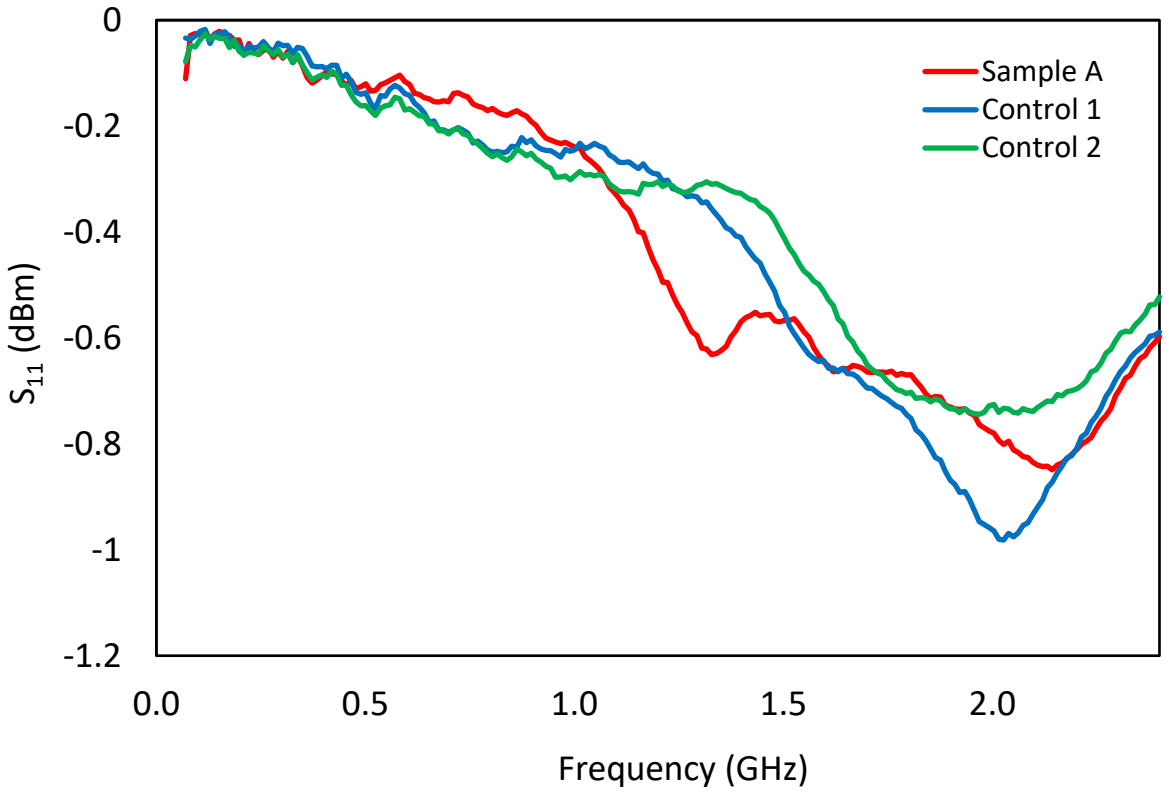

Fig. 6.13: The measured S11 parameter for Sample A and the control samples, from 70 MHz to 2.4 GHz.

Any dipole-type sub-wavelength antenna driven at electromagnetic resonance will have a radiation efficiency, η, of:

$$\eta = \frac{A}{\lambda^2} \qquad (6.1)$$

where A is the antenna area and λ is the electromagnetic wavelength. At 144 MHz, the electromagnetic wavelength is 2.1 m. The nanomagnet array area of Sample B is about 1 mm^2, and we can reasonably assume that only 10% of them will actually flip, giving a radiation efficiency of $5x10^{-8}$ had the antenna been driven at electromagnetic resonance. The reason the signal was detectable is due to driving the antenna not at the electromagnetic resonance, but at the acoustic resonance. Consequently, the effective ratio in Equation (6.1) exceeds unity. The antenna is extreme sub-wavelength when the wavelength is the electromagnetic wavelength, but super-wavelength when the wavelength is the acoustic wavelength.

Such miniaturized antennas have many applications, such as in personal communicators, miniaturized RFID, and medically implanted devices that need to communicate signals outside the body.

6.4 Calculations

The input power P_i to the antenna was 5 dBm, which yields $10\log_{10}(P_i) = 5$; $P_i = 3.16$ mW. At 144 MHz, the power P_n detected from the control sample (which is primarily due to surface currents in the contact pads) is found from $10\log_{10}(P_n)$ = -81.5 dBm, or $P_n = 4x10^{-9}$ mW = 4 pW. The power P_d detected from the real sample is found from $10\log10(P_d)$ = -73.4 dBm, or $P_d = 5x10^{-8}$ mW = 50 pW. Therefore, the power detected from the nanomagnet array is 50 – 4 = 46 pW. The "radiated" power is much larger than this since the radiation occurs over 4π solid angles and our dipole antenna detected only a small fraction of that.

The antenna dimension is about 1 mm x 1 mm with approximately 10% of the area occupied by nanomagnets, while the wavelength of electromagnetic radiation at 144 MHz is about 2.1 m. If this were a standard electromagnetic antenna driven at the electromagnetic resonance, then the radiation efficiency according to Equation (6.1) would have been $2.3x10^{-8}$. Based on past

experience, we can reasonably assume that no more than 10% of the nanomagnets were flipping and hence the renormalized maximum efficiency would be 2.3×10^{-9}. With input power of 3.16 mW, the radiated power would have been then limited to $3.16 \times 2.3 \times 10^{-9}$ mW = 7.2 pW. This is the maximum "radiated" power and the "detected" power in the far field (4 m away from the antenna) would be a small fraction of this, perhaps 1%, which would be 0.07 pW. Realistically, this value would be even smaller because the majority of the power is reflected back to the antenna based on the measured S_{11} parameter. We detected 46 pW, which beats this limit more than 600x.

6.5 Conclusion

In conclusion, we have demonstrated an extreme sub-wavelength electromagnetic antenna. The signal measured from the approximately 250,000-nanomagnet antenna sample is 10 dB above the noise floor and about 46 pW. Larger nanomagnet arrays would have produced more detected power. We point out that had the nanomagnets been driven at electromagnetic resonance, the detected power would have been much smaller than what we detected. We were able to beat the electromagnetic resonance limit by exciting the antenna at acoustic resonance. Hence, the demonstrated antenna performs superior to the corresponding electromagnetic antenna.

One last question to address is whether it would have been advisable to replace the nanomagnets with a much larger thin film of ferromagnet to obtain a larger magnetic moment and hence more radiated power. Unfortunately, this strategy can be self-defeating since the film would break up into many domains with different orientations of the magnetization, so that the spatial average of the magnetization would be small. In contrast, the nanomagnets will have one or few domains which can be made to align parallel to each other because the easy axes of the nanomagnets are mutually parallel. This could actually lead to a much larger magnetic moment. Thus, the use of nanomagnets instead of a thin film is advantageous.

Chapter 6 References

[1] Yao, Z; Wang, Y. E.; Keller, S.; Carman, G. P. Bulk acoustic wave mediated multiferroic antennas: architecture and performance bound. IEEE Trans. Antennas Propag. 2015, 63, 3335– 44.

[2] Domann, J. P.; Carman, G. P. Strain powered antennas. J. Appl. Phys. 2017, 121, 044905.

[3] Nan, T. et al. Acoustically actuated ultra-compact NEMS magnetoelectric antennas. Nat. Commun. 2017, 8, 296.

[4] Lin, H. et al. NEMS magnetoelectric antennas for biomedical applications. IMBioc 2018–2018 IEEE/MTT-S Int. Microwave Biomedical Conf., 2018, 13–15

[5] Lin, H.; Page, M. R.; McConney, M.; Jones, J.; Howe, B.; Sun, N. X. Integrated magneto-electric devices: filters, pico-Tesla magnetometers, and ultra-compact acoustic antennas. MRS Bull., 2018, 43, 841–847.

Chapter 7: Conclusion

In this thesis, I examined many aspects of nanomagnetic devices, involving information storage, processing, and communication.

A precessionally switched p-MTJ based memory cell where data is written with VCMA *without any on-chip magnetic field* was proposed and analyzed. The role of the in-plane magnetic field is played by applying strain via a piezoelectric substrate which generates an in-plane stress. This approach introduces some additional energy dissipation needed to generate the stress compared to devices which use a magnetic field, but that energy overhead is almost negligible. It is a small price to pay for eliminating the on-chip magnetic field.

Probabilistic (p-) bits implemented with low energy barrier nanomagnets (LBMs) were also analyzed through simulations, and plots show that the probability curves are not affected much by reasonable variations in either thickness or lateral dimensions. In the case of thickness variation, we see a significant difference only for the 15 nm thickness. Variation in the lateral dimension (minor axis length) is even more forgiving. A variation of more than 9 nm, which is 9% of the minor axis dimension, does not make a significant difference in the probability curves. The little variation that there is can be further suppressed by increasing the degree of spin polarization in the current. These results are reassuring since it implies that the "control" over p-bits exercised with spin polarized current is not impaired by reasonable device-to-device variations and therefore a fairly large number of p-bits can be harnessed for "p-circuits" in many applications, i.e. p-bits are generally "scalable," and the practicality of implementing p-bits with LBMs is unassailable.

An approach to obtaining deposition rate calibrations for the dual-chamber, ultrahigh vacuum 12-gun sputtering system in the Magnetic Engineering Research Facility at NIST was described. The development of this procedure laid the groundwork for future deposition rate calibrations. These deposition growth rates were integrated into a “recipe builder” user-interface for sample creation and documentation. Precisely calibrated deposition rates have many implications on magnetic device quality, and this process illustrates the foundation that must be laid before production of high-quality devices without growth variations and other defects can occur.

The feasibility of using a dusting layer of CoFe at the interface between CoFeB and MgO to achieve moderate perpendicular magnetic anisotropy, low damping, and relatively high saturation magnetization was demonstrated. For several annealed samples, we observed a net perpendicular magnetic anisotropy with a saturation magnetization exceeding 1500 kA/m and a Gilbert damping coefficient below 0.015. By inserting a CoFe layer between the CoFeB and MgO, we demonstrated an approach for introducing a thickness gradient in B content, which can modify the final properties of the annealed bilayer by changing the microstructure of the as-deposited film. This chapter explored some of the experimental aspects of p-MTJ devices which were simulated in Chapter 2.

Finally, an extreme sub-wavelength electromagnetic antenna was fabricated and tested. The antenna was driven at acoustic resonance instead of electromagnetic resonance and that allowed its radiation efficiency to exceed the limit for an electromagnetic antenna driven at the electromagnetic resonance. Hence, the demonstrated antenna performs superior to the corresponding electromagnetic antenna.

Overall, this dissertation covered a comprehensive study of nanomagnetic devices and their uses in technology for information processing – from simulating and analyzing the mechanisms behind the devices, to experimental investigations encompassing magnetic film growth to nanomagnetic device fabrication.

Vita and List of Publications

Justine Lynn Drobitch was born on September 22, 1990 in Windsor, Ontario, Canada. She received a B.S. in Physics and Astronomy from the University of Pittsburgh, Pittsburgh, Pennsylvania in April 2012. This thesis is the final requirement for a Ph.D. in Engineering with a concentration in electrical and computer engineering from Virginia Commonwealth University, Richmond, Virginia.

Journals – Published:

M. A. Abeed, J. L. Drobitch and S. Bandyopadhyay, "A Microwave Oscillator based on a Single Straintronic Magnetotunneling Junction," Phys. Rev. Applied **11**, 054069 (2019).

S. Nasrin, J. L. Drobitch, S. Bandyopadhyay, and A. R. Trivedi, "Low Power Restricted Boltzmann Machine Using Mixed-Mode Magneto-Tunneling Junctions," IEEE Elec. Dev. Let., vol. 40, no. 2, p. 345, Feb. 2019.

J. L. Drobitch, M. A. Abeed and S. Bandyopadhyay, "Precessional switching of a perpendicular anisotropy magneto-tunneling junction without a magnetic field," Jpn. J. Appl. Phys., vol. 56, no. 10, p. 100309, Sep. 2017.

Journals – In press:

J. L. Drobitch, Y.-C. Hsiao, H. Wu, K. L. Wang, C. S. Lynch, K. Bussmann, S. Bandyopadhyay, and D. B. Gopman, "Effect of CoFe Dusting Layer and Annealing on the Magnetic Properties of Sputtered Ta/W/CoFeB/CoFe/MgO Layer Structures," J. Phys. D: Appl. Phys. 2019 (in press)

J. L. Drobitch and S. Bandyopadhyay, "Robustness and scalability of p-bits implemented with low energy barrier nanomagnets," IEEE Mag. Let. 2019 (in press)

Conference proceedings

C. Campbell, A. Casey, D. Fomra, J. Drobitch, and G. Triplett, "The influence of the fabrication developing time on plasmonic bowtie nanoantenna metastructures," Proc. SPIE 11082, Plasmonics: Design, Materials, Fabrication, Characterization, and Applications XVII, 110822I (9 September 2019.

C. Campbell, A. Casey, M. Hren, J. Drobitch, G. Triplett, "A comparison of simulated and fabricated gold bowtie nanoantennas for molecular fingerprinting," Proc. SPIE 10891, Nanoscale Imaging, Sensing, and Actuation for Biomedical Applications XVI, 108910K (5 March 2019).

Conference presentations:

J. L. Drobitch, Y.-C. Hsiao, H. Wu, K. L. Wang, C. S. Lynch, K. Bussmann, S. Bandyopadhyay, and D. B. Gopman, “Effect of CoFe Dusting Layer and Annealing on the Magnetic Properties of Sputtered Ta/W/CoFeB/CoFe/MgO Layer Structures,” Bulletin of the American Physical Society, March Meeting 2019.